Master's thesis

NTNU
Norwegian University of Science and Technology
Faculty of Natural Sciences
Department of Materials Science and Engineering

Lasse August Dørum Backer

Carbon-Coated Industrial-Grade Silicon as Potential Anode Material in Lithium-Ion Batteries

Master's thesis in Chemistry
Supervisor: Ann Mari Svensson
Co-supervisor: Jan Petter Mæhlen, Alexey Koposov
June 2021

NTNU
Norwegian University of
Science and Technology

Lasse August Dørum Backer

Carbon-Coated Industrial-Grade Silicon as Potential Anode Material in Lithium-Ion Batteries

Master's thesis in Chemistry
Supervisor: Ann Mari Svensson
Co-supervisor: Jan Petter Mæhlen, Alexey Koposov
June 2021

Norwegian University of Science and Technology
Faculty of Natural Sciences
Department of Materials Science and Engineering

NTNU
Norwegian University of
Science and Technology

Summary

Silicon (Si) has been intensively researched over the past decade as a potential anode material for new-generation lithium-ion batteries (LIB). The main motivation being that Si has the ability to reversibly alloy with lithium to form highly lithium-concentrated Li_x-Si-phases, leading to an extremely high gravimetric capacity (3590 mAh g^{-1}).[1] This is about ten times that of today's commercial anode, graphite. However, the large volumetric and structural changes that occur as lithium is alloyed and de-alloyed with Si causes mechanical fractures of Si particles and unwanted side reactions with the electrolyte.[2] This leads to short battery cycle lives. Two promising mitigation strategies are a) size reduction of Si to the nano-range[3] and/or b) carbon (C)-coating the Si particles[4].

In order to achieve cheap batteries with low carbon footprints, the use of raw materials that can be produced on a large scale is essential. Therefore, making industrial-grade Si anodes with high capacity and cycling stability is highly desirable. The work presented here involves the electrochemical testing and material characterization of a micron- and a nano-sized industrial-grade Si powder. The reduced size of the nano-sized Si powder (n-Si) was achieved in a top-down approach and demonstrated a low initial delithiation capacity of 2105±271 mAh g^{-1}, compared to the 3235±119 mAh g^{-1} achieved for the micron-sized Si (m-Si), at a current density of 0.16 A g^{-1}. No gain in cycling stability was seen for the n-Si compared to m-Si.

The formation of C-coated m-Si particles with varying C thicknesses, made in a facile one-pot polymerization reaction with a resorcinol-formaldehyde (RF)-resin, are herein reported. The irregular-shaped m-Si obtained complete coatings with homogeneous thicknesses after being carbonized in a furnace. The thickness could be controlled under a critical RF-resin amount. A reaction with 60 wt% m-Si and 40 wt% RF-resin yielded m-Si/C with C layer thicknesses in the range of 50-70 nm. Increasing the RF-resin with a factor of 2.2 yielded m-Si/C with C layer thicknesses in the range of 100-150 nm. By increasing the RF-resin with a factor of 6, lead to the formation of pure polymer spheres with only minor C-coated. The m-Si/C composites did not demonstrate improved electrochemical performance compared to the pristine m-Si and the sample with the least C-coated outperformed the samples with thick C layers, suggesting that the C layer limits the lithiation of the Si-core.

The m- and n-Si powders were attempted C-coated with varying amounts of glucose. The Si/C composites obtained after carbonization had increasing amounts of C for both powders, however, the carbon layers were believed to be inhomogeneous and incomplete based on energy-dispersive X-ray spectroscopy (EDS)-analysis mapping. The m-Si/C composites made with glucose did not demonstrate improved electrochemical performance compared to the pristine m-Si and no relation between C amount and performance was seen. However, the sample with the highest C content had higher capacity retention in the 100. cycle (28±2%), compared to the other composites. The n-Si/C composites demonstrated increased cycling stability after around 100 cycles compared to the pristine n-Si, however, large deviations between cells with the same sample were seen. The n-Si/C composite with the least C (3.2 wt%) performed the best of all samples with n-Si. In the 100. cycle, it demonstrated an average delithiation capacity of 535±22 mAh g^{-1}, compared to 412±167 mAh g^{-1} for the pristine n-Si, at a current density of 1.6 A g^{-1}.

Preface

The research presented in this thesis was conducted in The Department of Battery Technology at the Institute for Energy Technology (IFE) and part of my Master of Science in Chemistry, at the Norwegian University of Science and Technology (NTNU). The work has been carried out in the fall of 2020 and spring of 2021 and is part of the ongoing research project "Silicon-based anodes towards market penetration" (SiBANODE, project number 296272). The project is lead by Elkem with IFE and SINTEF as partners, funded by the Research Council of Norway and Elkem. All experiments and analysis presented in this thesis were performed by the author, with the exception of the flash elemental analysis, Brunauer-Emmett-Teller (BET) surface area analysis, and transmission electron microscopy (TEM) analysis. This work was carried out by Ingar Johansen (IFE), Saima Sultana Kazi (IFE), and Per Erik Vullum (SINTEF), respectively, and is greatly appreciated.

I want to thank IFE for the opportunity to carry out my work at their facilities at Kjeller and under their guidance. The learning curve has been steep as I stepped into the world of batteries, and I am grateful for the time and resources spent to help me on my way. I would like to thank my supervisor Ann Mari Svensson for the thorough and valuable feedback on my thesis and for always being available if help was needed. My co-supervisors Jan Petter Mæhlen and Alexey Koposov are sincerely thanked for the many discussions regarding my work and for valuable feedback on my thesis. My most sincere appreciation goes to Andreas Wolf and Samson Yuxiu Lai. This work would not be possible without their support, training, guidance, discussions, and encouragement. Furthermore, Muhammad Abdelhamid, Carl Erik Lie Foss, Julia Wind, and Marius Uv Nagell are all thanked for always taking the time to support, when needed. I would also like to express my gratitude to the rest of the people in The Department of Battery Technology at IFE, for welcoming me into the group and always showing interest in my work. Moreover, I would like to thank my partner Mathilde Tillman Hegdal and my friends and roommates Vetle Birkeland Huglen and Elias Loona Myklebust for enduring the daily talks on battery technology over the past eight months. Without their encouragement and support, through both stressful and exciting times, this work would not be possible. Lastly, I want to express my huge gratitude to my family for the continuous encouragement during my studies.

Lasse August Dørum Backer, 04.06.21, Oslo

Table of Contents

Summary **i**

Preface **iii**

1 Introduction **1**

1.1 Aim of this work 2

2 Theory **3**

2.1 Introduction to batteries 3

2.1.1 Working principle 3

2.1.2 Terms and definitions 4

2.1.3 Cycling current and cut-off voltage 6

2.2 Lithium-ion battery 7

2.2.1 Working principle 7

2.2.2 Electrolyte 8

2.2.3 Solid electrolyte interphase (SEI) layer 9

2.2.4 Cathode materials 10

2.2.5 Anode materials 11

2.3 Si-based anode 13

2.3.1 Motivation 13

2.3.2 (De)lithiation mechanisms 14

2.3.3 Degradation mechanisms 15

2.3.4 Mitigation strategies 18

2.4 Si/C composite 21

2.4.1 Core-shell Si/C composites 22

2.4.2 The resorcinol-formaldehyde route 24

2.4.3 Glucose route 29

2.5 Characterization techniques 31

2.5.1 Material characterization 31

2.5.2 Electrochemical characterization 33

3 Experimental **35**

3.1 Coating methods 35

3.1.1 Chemicals and materials 35

3.1.2 Coating with resorcinol-formaldehyde resin 35

3.1.3 Coating with glucose 37

3.1.4 Carbonization 38
3.1.5 Ball-milling 39
3.2 Electrode fabrication 39
3.3 Cell-assembly 40
3.4 Electrochemical testing 40
3.4.1 Galvanostatic cycling 41
3.4.2 Rate-testing 41
3.4.3 Full-cell testing 41
3.5 Material characterization 42
3.5.1 X-ray diffraction (XRD) 42
3.5.2 Field emission scanning electron microscopy (FE-SEM) 42
3.5.3 Energy-dispersive X-ray spectroscopy (EDS) 42
3.5.4 Zeta potential measurements 42
3.5.5 Flash elemental analysis 43
3.5.6 Brunauer–Emmett–Teller (BET) 43
3.5.7 Transmission electron microscopy (TEM) 43

4 Results **45**
4.1 Industrial grade Si 45
4.1.1 Material characterization 45
4.1.2 Galvanostatic cycling 48
4.1.3 Heat-treatment of powders 51
4.2 Si/C composites with RF-resin 55
4.2.1 Synthesis and reference 55
4.2.2 Material characterization 57
4.2.3 Electrochemical testing 66
4.3 Si/C composites with glucose 75
4.3.1 Reference 75
4.3.2 m-Si/C composites 75
4.3.3 Galvanostatic cycling 79
4.3.4 n-Si/C composites 81

5 Discussion **87**
5.1 Industrial grade Si 87
5.1.1 Material characterization 87
5.1.2 Electrochemical testing 87
5.1.3 Heat-treatment of the Si-powders 89

5.2 Si/C composites with RF-resin 90
5.2.1 Synthesis and reference 90
5.2.2 Material characterization 92
5.2.3 Galvanostatic cycling 94
5.3 Si/C composites with glucose 98
5.3.1 m-Si/C composites 98
5.3.2 n-Si/C composites 100
5.4 General remarks 102

6 Conclusion **105**

7 Further work **107**

Bibliography **109**

Appendix **123**

1. Introduction

The 5-year period (2016-2020) went down as the warmest ever recorded and CO_2-levels in the atmosphere hit record heights in 2020.[5,6] With the current progression, there is no chance of achieving the goal of the Paris Agreement which states that the average global temperature must be limited to 1.5°C above pre-industrial levels.[6] Electrification of society is crucial in reducing greenhouse gas emissions and turning the trend around. It means replacing a fossil-based power supply with renewable energy and is part of UN's Sustainable Development Goals towards 2030; goal seven states: "Ensure access to affordable, reliable, sustainable and modern energy for all".[7] To enable the electrification of our society, batteries are crucial. As stationary storage, they allow for the storage of excess energy from renewable energy sources, such as solar and wind. Batteries are also vital in enabling a wide deployment of electric vehicles, which could heavily reduce the carbon footprint of the transportation sector.

Today, the dominant secondary battery technology is lithium-ion batteries (LIBs). It was first commercialized by Sony in 1991 and has affected our lives immensely. In 2019, John B. Goodenough, M. Stanley Whittingham, and Akira Yoshino received the Nobel prize in Chemistry for the development of the LIB.[8] The battery has a high energy density, which makes it especially attractive for electrical vehicles and portable electronics. After two decades of improvements in the battery's chemistry, cell design, and the production process, the prices of LIBs have decreased by a staggering 97% since 1991 and are predicted to fall under 100 USD/kWh within the next five years.[9,10,11] This is predicted to make LIBs competitive with the energy cost of gasoline.[12] The increased efforts in LIB recycling, and the principles of circular economy during LIB production, allow assuming that LIBs will maintain the dominant position for the upcoming decade.[13]

Regardless of the improvements to the LIB since 1991, the acceleration has been most significant in the production and up-scaling, rather than the chemistry. Therefore, it consists of almost the same materials as the batteries commercialized in 1991. In order to keep up with the acceleration in the production of renewable electrical energy and electrical vehicles, there are great efforts from scientists around the world to reinvent parts of the battery.[14] The batteries of the future are green and with higher energy densities. The electrode materials used in a battery, the cathode and anode, mainly determine the energy density of the battery. A promising anode material is silicon (Si), because of its extremely high theoretical lithium (Li) storage capacity (3590 mAh g^{-1}). That is about ten times higher than today's commercialized anode material, graphite. Si is also the second most abundant element in the earth's crust (27.7%) and the production is well established which makes it cheap.[15,16] However, major issues associated with large volume changes during (dis)charging result in short battery life and hinders widespread commercialization.

Great efforts have been made in tackling the challenges of Si-based anodes and include strategies such as structural designs (Si-sponges[17], Si-nanorods[18], Si-nanotubes[19]), Si-based ceramic powders (SiC[20] and SiN[21]), and Si/carbon (Si/C)-composites.[22,3,23] Although these approaches represent keys to improve the performance of Si as an anode material, the methods and materials are often expensive and energy-demanding for large-scale production. Achieving a high-performance Si-based anode with a cheap and green industrial-grade Si is therefore highly desirable.

1.1 Aim of this work

The aim of this work is to make Si/C composites, by C-coating industrial-grade Si, with improved performance in a LIB. Industrial-grade Si will be coated with two carbon precursors, namely resorcinol-formaldehyde-resin and glucose. The aim is to achieve carbon coatings with varying thickness in order to find an optimum amount. Reducing the particle size of Si is a common strategy in order to increase the performance of Si as an anode.[24,25] The electrochemical differences between micron-sized and nano-sized industrial Si will therefore also be studied, with and without C-coating. A simplified schematic of the work is shown in Figure 1.1.

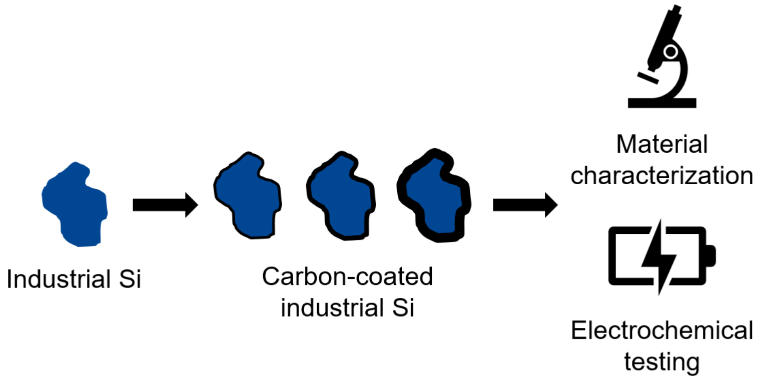

Figure 1.1: Simplified schematic of the work.

2. Theory

2.1 Introduction to batteries

According to the Oxford dictionary, a battery is defined as "*A container consisting of one or more cells, in which chemical energy is converted into electricity and used as a source of power*".[26] In this report, a *battery* refers to a single electrochemical cell.

2.1.1 Working principle

A battery can convert chemical energy to electric energy via oxidation and reduction (redox) reactions at the electrodes, caused by the difference in electrochemical potentials of the two electrodes.[27] During discharge, the reduction occurs at the cathode (positive electrode) and the oxidation occurs at the anode (negative electrode). A battery also contains an electrolyte that transports ions, while electrons are conducted in an outer circuit to do work. A separator acts as a physical barrier between the electrodes to prevent electrical shorting, but is porous, and thus permeable to the ionic component.[28] Batteries can be divided into two groups: primary and secondary batteries. A primary battery is assembled in a charged state and when its initial reservoir of reactants is depleted, the battery's life is over. Secondary batteries, are intended to be recharged multiple times and thereby restore their ability to store electric energy. Charging is done by applying electric current in the opposite direction of the electron flow at discharge and thereby changing the direction of the redox reactions.[28] The further theory will concern secondary batteries. A schematic of the secondary LIB can be seen in Figure 2.1.

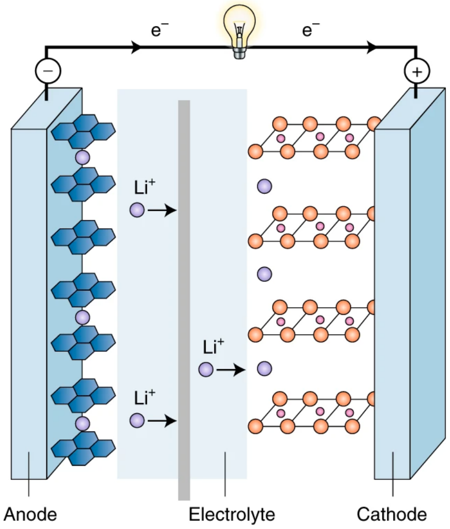

Figure 2.1: Illustration of a lithium-ion battery at discharge. Reprinted from ref.[29].

2.1.2 Terms and definitions

At standard conditions, the oxidation and reduction reactions have standard electrode potentials ($E°$) and the difference between the potentials give rise to the standard cell voltage (E°_{cell})[27]. The net Gibbs free energy (ΔG), at standard state, can be described as

$$\Delta G° = -nFE^{\circ}_{\text{cell}} \tag{2.1}$$

where n is the number of electrons transferred per mole of reactants and F is the Faraday's constant[30]. At non-standard conditions, the open-circuit voltage (V_{oc}) is the difference between the electrochemical potentials of the anode (μ_{A}) and cathode (μ_{C}) when no net current is flowing, as follows

$$V_{\text{oc}} = \frac{(\mu_{\text{A}} - \mu_{\text{C}})}{e} \tag{2.2}$$

where e is the elementary charge.[31,27] During charge and discharge, the battery experiences polarization losses which leads to a decrease in the discharge voltage (V_{dis}) and a increase in the charge voltage (V_{ch}), compared to the V_{oc}. In other words, less energy is delivered at discharge than theoretically possible, and more energy is needed to drive the reactions in reverse. The polarization losses (or overvoltage), η, includes ohmic losses, transportation losses and kinetic losses and are dependent on the current (I) and the state of charge (q). The voltages at discharge and charge can be expressed as[29, 30]

$$V_{\mathrm{dis}} = V_{\mathrm{oc}} - \eta(q, I_{\mathrm{dis}}) \tag{2.3}$$

$$V_{\mathrm{ch}} = V_{\mathrm{oc}} + \eta(q, I_{\mathrm{ch}}) \tag{2.4}$$

The operating voltage is an important factor in the overall energy achieved by a battery. However, the capacity at which it can be delivered is also key. Electrode materials have a specific capacity, C_{E}, based on the number of electrons involved in the reaction and its molar weight. The overall theoretical specific capacity of a battery, Q, is defined as the total charge per unit weight (mAh g^{-1}) or volume (mAh cm^{-3}), and can be expressed as[31]

$$Q = \int_0^{\Delta \mathrm{t}} I \,\mathrm{d}t = \int_0^{Q} \mathrm{d}q \tag{2.5}$$

where Δt is the time of running a current, I, and q is the state of charge. The specific capacity current-dependent. For instance, cycling at high currents leads to a diffusion-limited charge transfer and increased concentration polarization.[31] The discharge energy, E_{dis}, is a function of the voltage, V, and capacity, and dependent on the discharge current, I_{dis}. By measuring the time of discharge, $\Delta t(I_{\mathrm{dis}})$, for a constant I_{dis} = dq/dt, E_{dis} can be obtained as follows[31]

$$E_{\mathrm{dis}} = \int_0^{\Delta \mathrm{t}} IV(t) \,\mathrm{d}t = \int_0^{Q} V(q)\mathrm{d}q \tag{2.6}$$

where the energy of a battery is often given as the energy per unit weight (Wh kg^{-1}) or volume (Wh L^{-1}). As mentioned, the current will influence the performance of a battery and some other important factors are temperature, cut-off voltage, and electrode loadings of active material. Coulombic efficiency (CE) is commonly used as a measure of the capacity loss for an individual cycle and is defined as[31]

$$\mathrm{CE} = \frac{Q_{\mathrm{dis}}}{Q_{\mathrm{ch}}} \times 100 \tag{2.7}$$

with CE commonly being less than 100% due to losses. Irreversible capacity loss (ICL), for a specific cycle i, can be quantified as

$$\mathrm{ICL} = Q^{\mathrm{i}}_{\mathrm{ch}} - Q^{\mathrm{i}}_{\mathrm{dis}} \tag{2.8}$$

The cumulative irreversible capacity loss (CICL) is the sum of the ICL of n cycles

$$\mathrm{CICL} = \sum_{\mathrm{i}=1}^{\mathrm{n}} (Q_{\mathrm{ch}}^{\mathrm{i}} - Q_{\mathrm{dis}}^{\mathrm{i}}) \tag{2.9}$$

The number of cycles it takes for a battery to fade to 80% of its initial reversible capacity, is known as its cycle life.

The terms anode and cathode are relative and are often defined by the reaction that occurs (oxidation or reduction) at the individual electrode or by the electrode potential relative to the other. Common for batteries, the terms "anode" and "cathode" are defined by the oxidation and reduction reaction, respectively, that occur at discharge and will not change at charging. The terms lithiation and delithiation will also be used for charging and discharging, respectively, when discussing LIBs. The term intercalation is described by Whittingam *et al.* as "the reversible insertion of guest species into a lamellar host structure with maintenance of the structural features of the host"[32], and used to describe the insertion of Li^+ in graphite. Today, the term is widely used for non-layered structures as well, including the insertion into crystal lattices in various cathode materials. The term intercalation (or insertion/host) material/compound is used for both cathode and anode. The term "cycling" will be used to describe the continuous (dis-)charging/(de)lithiation in a battery.

2.1.3 Cycling current and cut-off voltage

The C-rate of a battery is a measure of the current applied during charge and/or discharge and is related to the battery's capacity. 1C equals the current for a battery with an X capacity to be fully discharged in one hour. For a battery with a capacity of 100 mAh, charge or discharge at 1C equals a current of 100 mA and C/2 equals a current of 50 mA for two hours. Cut-off voltages, during charging and discharging, are adopted in order to prevent side reactions that reduce the battery's safety and cycle life. Overcharging or over-discharging can lead to exothermic decomposition reactions that cause thermal runaway. At high currents, cut-off voltages are reached earlier due to the increased polarization. This is known as a reversible capacity loss that can be recovered by reducing the (dis-)charge rates.[33] The loading ($\mathrm{mg\ cm^{-2}}$) of active material and electrode thickness will also influence the performance of the battery. In thick electrodes, the diffusion distance from the current collector to active material is longer, which can cause a lithiation gradient in the electrode at higher currents.

2.2 Lithium-ion battery

LIBs are the leading battery technology in consumer electronics and in electric vehicles, due to the importance of a high energy density. As shown in section 2.1.2, the gravimetric energy density (Wh kg^{-1}) is a function of the operating voltage, capacity, and weight. Crucial for the success of the technology is the intrinsic properties of Li, such as low potential (-3.04 vs. standard hydrogen electrode) and low atomic weight.[34] This results in batteries with typical operating voltages of 3.6-3.7 V and therefore high gravimetric energy densities (> 200 Wh kg^{-1}), compared to other battery technologies.

2.2.1 Working principle

The lithium-ion battery is secondary and converts chemical energy to electric energy through redox reactions at its electrodes. It operates reversibly by shifting Li^+ and electrons back and forth between two electrodes, during cycling. The electrolyte allows for Li-ion diffusion within the battery. Commonly, the electrodes are comprised of intercalation materials, such as a lithium metal oxide cathode ($LiMO_2$) and a graphite (C) anode, that acts as hosts. Intercalation materials allow for reversible insertion and extraction of Li^+.[35] These electrochemical intercalation reactions (redox) are described as follows[31]

$$\textbf{Cathode} : \mathrm{LiMO_2 \leftrightarrow Li_{1-x}MO_2 + xLi^+ + xe^-} \tag{2.10}$$

$$\textbf{Anode} : \mathrm{C + xLi^+ + xe^- \leftrightarrow Li_xC} \tag{2.11}$$

$$\textbf{Overall} : \mathrm{LiMO_2 + C \leftrightarrow Li_{1-x}MO_2 + Li_xC} \tag{2.12}$$

where M represents a transition metal. The forward and backward reactions, in (2.12), represents discharge and charge, respectively. Reactions 2.10-2.11 represents common commercial battery chemistries.

2.2.2 Electrolyte

The electrolyte of a battery is the medium of charge transport of Li^+ between the two electrodes. The open-circuit voltage (V_{oc}) of a battery is determined by the difference in electrochemical potentials (or Fermi levels) of the electrodes, as seen in Equation 2.2. The species of the electrolyte can also be involved in redox reactions if the potential is sufficiently high or low. Therefore, the (V_{oc}) is limited by the electrolyte's molecular orbital energies. In order to avoid redox reactions with the electrolyte, the potential must be within its energy window,E_{g}.[33] The E_{g} is determined by the difference between the lowest unoccupied molecular orbital (LUMO) and the highest occupied molecular orbital (HUMO) of the electrolyte. To avoid electrolyte oxidation at the cathode (oxidant), the cathode's Fermi level must be higher than the electrolyte's HOMO. To avoid electrolyte reduction at the anode (reductant) the anode's Fermi level must be lower than the electrolyte's LUMO. This is known as thermodynamic stability and is illustrated in Figure 2.2. In order to make a battery with higher V_{oc} than the electrolyte's E_{g} allows for, a passivating layer must be created at the electrode-electrolyte interphases. This will be further addressed in section 2.2.3.

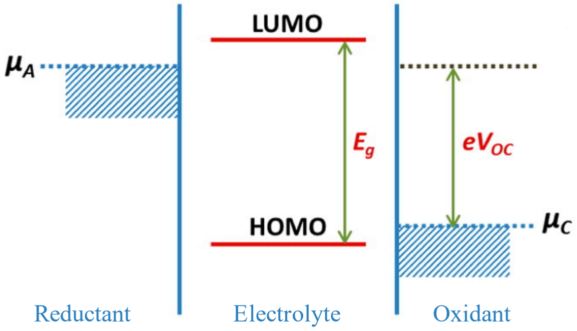

Figure 2.2: Illustration of the molecular orbital energy levels of the reductant (anode), electrolyte and oxidant. Reprinted from Ref[31].

J. B. Goodenough *et al.* have formulated the requirements of a LIB electrolyte, as follows:[33]

1. Large energy window, E_{g}
2. Retention of the electrode-electrolyte interphase as particles volume change
3. A Li^+-ion conductivity $\sigma_{\mathrm{Li}} > 10^{-4}$ S/cm in temperature range of operation
4. An electronic conductivity $\sigma_{\mathrm{c}} < 10^{-10}$
5. A transference number $\sigma_{\mathrm{Li}}/\sigma_{\mathrm{tot}} \approx 1$

6. Chemical stability temperature range of operation
7. Chemical stability in regards to the electrodes and rapid formation of a stable SEI
8. Preferably safe materials (nonflammable, nonexplosive)
9. Low toxicity and low cost

A common electrolyte for commercial LIBs is the salt lithium hexafluorophosphate ($LiPF_6$) solved in organic carbonates such as ethylene carbonate (EC) with dimethyl carbonate (DMC), propylene carbonate (PC), diethyl carbonate (DEC), and/or ethyl methyl carbonate (EMC).[36]

2.2.3 Solid electrolyte interphase (SEI) layer

Graphite and Si have higher Fermi levels than the LUMO of common electrolytes and thus making thermodynamically unstable batteries that cause the reduction of electrolyte. Electrolyte species decompose on the surface of the anode and form a passivating SEI layer that hinders further decomposition of the electrolyte while remaining Li-ion conductive. This allows for high voltage batteries with electrode potentials outside the energy window of the electrolyte. The SEI formation occurs mostly in the first cycle and consists of a variety of reduction products from the electrolyte reduction. Li^+ are consumed irreversibly and contribute to an overall loss in the battery's capacity. As a result, the coulombic efficiency is therefore especially low for the first cycle. Figure 2.3shows a model of the SEI layer on a graphite anode and common species making up the layer. Prelithiation is a method of accounting for the loss by having an excess of lithium ions in the electrodes, however, this will not be addressed further. Reducing the overall surface area of the electrodes will reduce the SEI-layer formation and thus reduce the loss of Li^+. Commonly, this gives an increase in the CE. However, high surface area electrodes have improved power performance. Therefore, the battery's intended use plays a key role in designing the electrode properties.[37] The desired functional properties of an SEI layer according to Peled *et al.* are as follows:

1. High electrical resistance
2. High lithium ion selectivity and permeability
3. High strength (mechanically stable and flexible)
4. Thickness close to a few nanometers
5. Tolerance to expansion and contraction stresses
6. Insolubility in the electrolyte
7. Stability over a wide range of operating temperatures and potentials

Meeting the properties above is especially challenging for a Si anode, as it experiences huge volume changes during cycling. In recent years, fluoroethylene carbonate (FEC) and vinylene carbonate (VC) has been extensively used as electrolyte additives for Si-based LIBs, due to the improved cycling stability.[38] This will be addressed in Section 2.3.4.

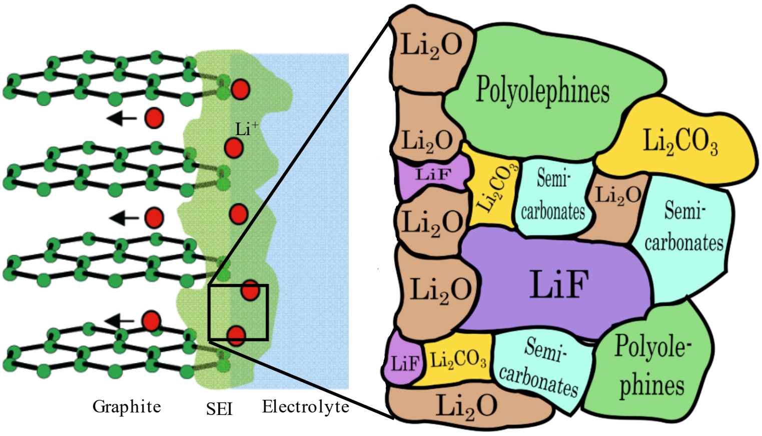
Li^+
Graphite
SEI
Electrolyte
Li_2O
Polyolephines
Li_2O
Li_2CO_3
LiF
Li_2CO_3
Semi-carbonates
Li_2O
Semi-carbonates
Li_2O
LiF
Li_2O
LiF
Li_2CO_3
Semi-carbonates
Polyole-phines
Li_2O

Figure 2.3: Illustration of SEI on a graphite surface and the composition of the SEI. Adapted from ref.[39, 33]

2.2.4 Cathode materials

Ever since LIB's commercialization, lithium transition metal oxides have been the prevalent cathode material.[40] Later, polyanions materials, such as $LiFePO_4$, have also been developed and commercialized. These materials allow for Li^+ to readily be extracted or inserted into the lattice structure. Crucial for this extraction and insertion is the transition metals' ability to change oxidation states. The structures of cathodes can mainly be classified as either layered types, such as $LiCoO_2$, spinel type, such as $LiMn_2O_4$ and olivine type, such as $LiFePO_4$. Cathode potentials are typically in the range of 3.3-4.2 V (vs. Li/Li^+)[31, 41] The specific capacity of cathodes is limited to the reversible solid-solution range of Li in the material, and are therefore lower than the theoretical values.[31] The capacity is in the range of 100-180 mAh g^{-1} in commercial cells.[42] Other important factors of cathodes are safety, weight, cost, power performance, degradation, and cycle life.

2.2.5 Anode materials

This section will give an overview of some common anode materials. Section 2.3 will focus on the Si anode. The main criteria for anode materials are:[43]

1. Low voltage vs. Li/Li^+
2. High ionic conductivity
3. High electric conductivity
4. High reversible capacity
5. High lithium diffusion rate
6. Long cycle and calendar life
7. High safety
8. Low cost
9. Low toxicity and high eco-compatibility.

In principal, Li metal would be an ideal anode material due to the extremely high theoretical specific energy density (3860 mAh g^{-1}) and the lowest negative electrochemical potential (-3.040 V vs. standard hydrogen electrode).[44] However, a low CE as a result of an unstable SEI-layer and potential electroplating of Li to form dendrites that can cause an internal short-circuiting of the battery, are major issues.[42] Therefore, to avoid severe safety concerns, a host material is used to store the Li. These materials are referred to as anodes and can be divided into three different groups based on their operating principles: intercalation, alloy, and conversion.[42] Each group represents an electrochemical lithiation/delithiation mechanism. Further, the introduction to the Li-storing mechanisms of intercalation and alloy materials will be given.

Intercalation materials

The intercalation materials include the most common commercial anode material, graphite. The electrochemical intercalation of lithium into the graphite structure is enabled by its lamellar structure of stacked graphene sheets. The lithium can be stored in between the layers. Graphite has high Li-ion conductivity, high electric conductivity, and high 2D mechanical stability.[41] The theoretical specific capacity of graphite is 372 mAh g^{-1}, determined by graphite's ability to store 1 Li atom per 6 C-atoms. The reaction is shown in Equation 2.11. Graphite has a low working potential vs. Li/Li^+, high thermal conductivity, and relatively low volume change during cycling which are all favorable properties as an anode material.[41,42] Another commercially available intercalation anode is lithium titanium oxide (LTO), $Li_4Ti_5O_{12}$. Key advantages of LTO include superior thermal stability, high cycling rates, low volume change at cycling, and long cycle life. LTO has a lower theoretical specific capacity (175 mAh g^{-1}) and higher working potential ($\sim$1.55 vs. Li/Li^+), compared to graphite. Operating at a higher potential window mainly avoids the formation and growth of SEI at the anode. However, the lack of a passivation layer allows for reactions with the organic electrolyte leading to gassing. LTO has also low electric conductivity.[41]

Alloying materials

Alloying anode materials electrochemically alloy with Li and can be represented as a reversible reaction as follows

$$\mathrm{xLi^+ + xe^- + A \leftrightarrow Li_xA} \tag{2.13}$$

where A is the anode material. The number of Li atoms, x, will be dependent on the materials alloying phases and determine its capacity. Widely studied alloy materials include Si, Ge, and Sn.[45] They have extremely high theoretical specific capacities (up to 4200 mAh g^{-1}). By replacing graphite with Si, the gravimetric energy density of a battery could increase by 40%.[46] However, the major drawback of huge volume change, up to $\sim$410% during cycling, hinders commercialization.[47] The lithiation mechanism includes the breaking of covalent or metallic A-A bonds and the formation of Li-A bonds, which are fundamentally different from the intercalation materials.[46] However, the high capacity of these materials results in great volumetric changes during (de)lithiation as will be discussed in section 2.3.3. Table 2.1 lists characteristics of the most common anode materials.

Table 2.1: A comparison of key parameters for common anode material. Values from ref.[46]

Materials	**Li**	**C**	**$Li_4Ti_5O_{12}$**	**Si**
Density [g/cm^3]	0.53	2.25	3.5	2.3
Lithiated phase	Li	LiC_6	$Li_7Ti_5O_{12}$	$Li_{4.4}Si$
Q_g (delithiated) [mAh g^{-1}]	∞	372	175	4200
Q_g (lithiated) [mAh g^{-1}]	3860	339	168	2010
Q_v (delithiated) [mAh cm^{-3}]	∞	837	613	9660
Q_v (lithiated) [mAh cm^{-3}]	2050	747	614	2370
Delithiation potential vs. Li/Li$^+$	>0	>0.05	1.6	~0.4
Volume change [%]	∞	<10	1	410

Q_g, Q_v are the theoretical gravimetric and volumetric capacities.
Volume change = (volume (lithiated)/volume (delithiated) - 1) × 100

2.3 Si-based anode

2.3.1 Motivation

Si has been intensively researched over the past decade as a potential anode material for new-generation LIBs. The main motivation being the high gravimetric capacity, about ten times that of graphite, see table 2.1. Other key factors are:[16]

1. Low discharge voltage (~0.4)
2. High abundance
3. Low cost
4. Non-toxic
5. Established production

The discharge voltage allows for a good balance between high OCVs and avoiding Li plating. As the second most abundant element in the earth's crust and established production, the cost of Si is low. However, huge volume expansion with subsequent contraction during (de)lithiation causes mechanical damage to the materials, resulting in rapid degradation of electrochemical performance.[48] In a Si-based battery, as of today, the cathode will be the limiting electrode in terms of capacity. The overall battery capacity increases asymptotically as the anode capacity is increased. Therefore, making an electrode with a stable capacity of 1200 mAh g^{-1} is often considered sufficiently high and would give an overall battery capacity increase of $\sim$25%.

2.3.2 (De)lithiation mechanisms

Crystalline (c) and amorphous (a) Si can both be used as alloy type anodes that form various lithium-silicide alloys (Li_xSi), electrochemically. The equilibrium alloy phase with the highest Li concentration is $Li_{22}Si_5$, giving a specific capacity of 4200 mAh g^{-1}.[2] The mechanisms and respective Li_xSi phases that occur during (de)lithiation have been extensively studied using various characterization techniques such as ex- and in-situ TEM, ex- and in-situ NMR spectroscopy, ex- and in-situ XRD diffraction, density-functional theory (DFT) calculations etc.[2,49,50,51,52,53]

The first electrochemical lithiation of c-Si is shown to occur via a two-phase mechanism in which a metastable amorphous phase (a-Li_xSi) is formed. The crystalline equilibrium phases are kinetically hindered.[51,52,53,49] The mechanism involves breaking of Si-Si bonds at a rate-limiting reaction front. This induces lithiation gradients and is associated with huge mechanical stress in the Si particles.[2] The lithiated amorphous phase formed is $Li_{3.5\pm0.2}Si$. Obrovac *et al.* found that for potentials <50 mV vs. Li/Li$^+$ (at room temperature (RT)), the amorphous lithium-silicide phase did not reach $Li_{22}Si_5$; however, crystallized to a metastable $Li_{15}Si_4$ phase. The crystalline phase is commonly reported as the terminal phase at RT, with a specific capacity of 3579 mAh g^{-1}.[1,54] The transition from amorphous to crystalline is associated with increased irreversible losses that limit the cycling performance. A cut-off voltage of 50 mV is therefore often employed in galvanostatic cycling.[1] Ogata *et al.* investigated the phases forming during galvanostatic cycling of c-Si and the respective potentials at which they form.[50] The results are summarized in Table 2.2.

Table 2.2: Summary of the lithiation and delithiation reactions of c-Si nanorods at galvanostatic cycling. x is calculated to be ∼3.5 for the first step in L1. δ has a value of 0.2-0.3.[50]

	Reaction	Potential [V]
1^{st} Lith		
L1	c-Si → a-Li_xSi → c-$Li_{3.75}Si$ → c-$Li_{3.75+\delta}Si$	0.10
≥ 2^{th} Lith		
L2	a-Si → a-$Li_{2.0}Si$	0.25-0.30
L3	a-$Li_{2.0}Si$ → a-$Li_{3.5}Si$	0.10
L4	a-$Li_{3.75}Si$ → c-$Li_{3.75}Si$	0.05-0.06
L5	c-$Li_{3.75}Si$ → c-$Li_{3.75+\delta}Si$	0.03
1^{st} Delith		
D1	c-$Li_{3.75+\delta}Si$ → c-$Li_{3.75}Si$ + c-$Li_{3.75+\delta}Si$	0.05-0.15
≥ 2^{th} Delith		
D2	a-$Li_{3.5}Si$ → a-$Li_{2.0}Si$	0.27-0.30
D3	c-$Li_{3.75}Si$ → a-$Li_{1.1}Si$	0.43
D4	a-$Li_{2.0}Si$ → a-Si	0.50

For c-Si, the first lithiation (L1) and delithiation (D1) differ from the subsequent cycles due to the formation of the amorphous phase. The second and third step of the reactions of L1 is dependent on the cut-off potential.[50]

2.3.3 Degradation mechanisms

The major drawback of a Si-anode is the huge volume changes experienced during cycling, leading to poor cyclability. Obrovac *et al.* reported that the $Li_{15}Si_4$ phase had a volume expansion of 280%, which causes particle stresses that lead to fractures.[1] An in-situ TEM study from McDowell *et al.* revealed that the first lithiation of amorphous and crystalline Si both occur via a two-phase lithiation reaction.[49] After the first lithiation, the reaction occurs via a single-phase lithiation for the subsequent cycles. Models have shown that the nature of the induced particle stresses is different for the two lithiation reactions.[25] In a single-phase lithiation, the stress is diffusion-induced and arises from inhomogeneous volume expansion as a result of Li concentration gradients. The diffusion rate of Li is determined by Fick's law.

In a two-phase lithiation reaction there is a sharp change in the concentration of Li between the unreacted c-Si and the a-Li_xSi. The stresses occur as the volume expansion takes place in a local region near the reaction front. The newly created Li_xSi at the core/shell interphase pushes out the already-formed Li_xSi leading to tensile hoop stresses at the surface.[49] The deformation is controlled by the migration of the reaction front.[2] Figure 2.4 illustrates the concentration difference in a spherical Si particle in a one-phase (de)-/lithiation reaction and two-phase lithiation reaction. The experienced tensile and compressive hoop stresses, close to the center and at the surface of the particles, are marked. Another in-situ TEM study of the lithiation kinetics from McDowell *et al.*, suggested that the reaction front in a two-phase lithiation of c-Si is retarded due to compressive stresses.[55] Later, McDowell *et al.* found that the kinetics of an initial lithiation of a-Si behaved linearly.[49]

In-situ TEM by Liu *et al.* have also shown that the volume expansion during lithiation is anisotropic, for a two-phase reaction in c-Si. The proposed reason being that different crystallographic planes have different interfacial mobility of Li. In-situ TEM showed a faceted Si core during lithiation as a result of the different mobility[25] Thus, acoustic fracture measurements have shown that there is a higher frequency of fractures in the first lithiation of c-Si compared to the following cycles.[56]

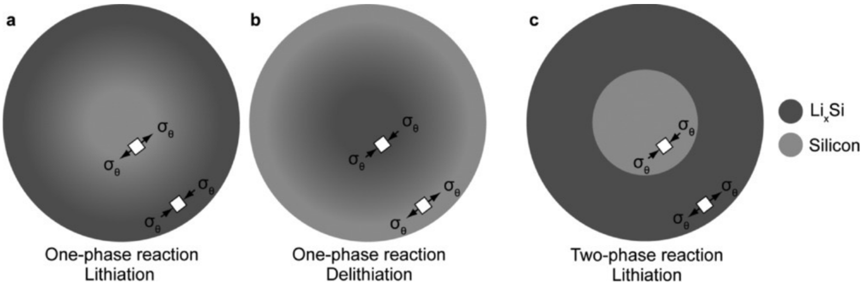
a
b
c
σθ
σθ
σθ
σθ
Li_xSi
● Li_xSi
● Silicon
One-phase reaction Lithiation
One-phase reaction Delithiation
Two-phase reaction Lithiation

Figure 2.4: Illustration of the a) one-phase reaction lithiation, b) one-phase reaction delithiation and c) two-phase reaction lithiation. The grey colour are used to show the Li concentration. Compressive and tensile hoop stresses, σ_ϑ, arising as a result of volume expansion gradients are indicated in the particles. For a) and c), the stresses are reversed. Reprinted from Ref.[2]

The tensile hoop stresses on the surface of the Si particles causes cracks to propagate and particles to fracture. Continuous cycling of Si will therefore often end in pulverization of the particles.[57] Electrical isolation of particles is also a result of volume changes. Reduced integrity of the electrode layer that is cast onto a current collector foil is seen. This can lead to delamination from the current collector or electrode material. Isolation can also occur as particles are covered in a thick and complete SEI layer. Both degradation mechanisms lead to an increase of irreversible losses and capacity fade.

Section 2.2.3 highlighted the importance of a stable passivating SEI-layer on the surface of the anode. However, the volume changes cause the SEI layer to continuously break and therefore exposing fresh Si surface to the electrolyte. As a result, the electrolyte and Li^+ are consumed in the formation of a new SEI layer. The electrolyte is eventually depleted in Li^+ and the battery is no longer functional. This continuous consumption of Li^+ leads to a fast capacity fade. A thick SEI layer also reduces the rate performance of the battery, as the energy barrier of diffusion in the SEI is higher compared to the electrolyte, thus, increasing the internal resistance and overpotential.[58] This is highly non-advantageous as Si already suffers from poor electric and ionic conductivity due to its semiconducting properties. Figure 2.5 illustrates three common degradation mechanisms, discussed above.

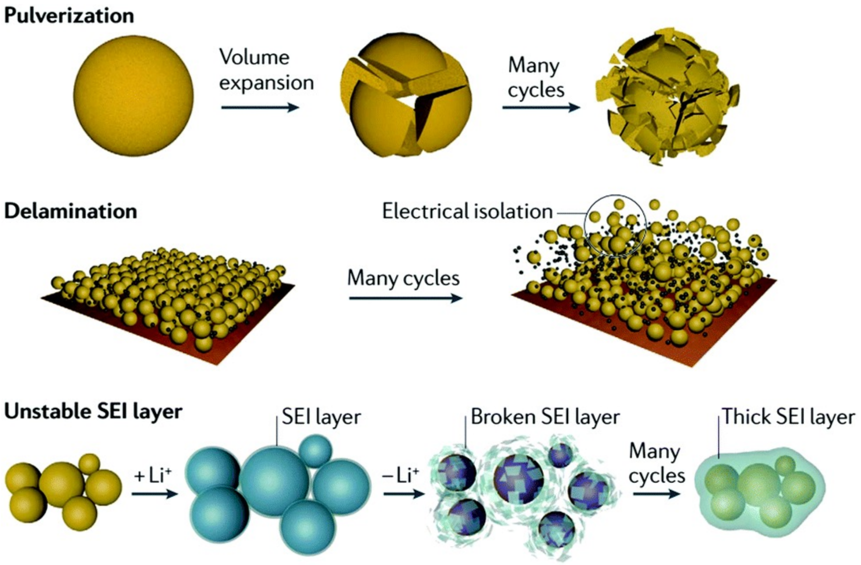
Pulverization
Volume expansion
Many cycles
Delamination
Electrical isolation
Many cycles
Unstable SEI layer
SEI layer
Broken SEI layer
Thick SEI layer
+Li⁺
−Li⁺
Many cycles

Figure 2.5: Illustration of three common degradation mechanisms for Si anodes: pulverization, delamination and unstable SEI layer. Reprinted from Ref.[48]

2.3.4 Mitigation strategies

Intensive research over the last decades have lead to significant insights into the behavior of Si as an anode material. In this section, some important improvement efforts and concepts will be addressed. C-coatings will be addressed in greater detail under Section 2.4.

Size reduction and amorphization

An in-situ TEM study by Liu *et al.* revealed that fractures during lithiation of spherical c-Si particles are strongly size-dependent.[25] They showed that particles below a critical particle diameter of ∼150 nm, did not crack or fracture in the first lithiation, thus, reducing pulverization and related irreversible losses. This was attributed to the insufficient amount of strain energy release to drive crack propagation in small-sized nanoparticles.[25] In-situ TEM studies from McDowell *et al.* also showed that the cracking and fracture of Si NPs might be dependent on their crystallinity.[49] Their spherical a-Si NPs with diameters up to 870 nm did not fracture upon lithiation, potentially making it a better candidate as anodes compared to c-Si. The difference in critical diameter was proposed to be due to: 1) increased stress in specific locations due to anisotropic lithiation in c-Si, 2) lower Li^+ concentration in the Li_xSi phase for a-Si and therefore lower volume expansion at the Si-Li_xSi interface, reducing the stresses 3) faster Si-Si-bond breaking at the reaction front for a-Si.

Making spherical Si NPs in a bottom-up process is expensive. As an alternative, Gauthier *et al.* presented the results of milling micron-sized c-Si to form NPs in a top-down process.[24] The milled Si NPs showed improved cycling stability with less irreversible losses and high CE, compared to the micron-sized Si. The milling was done under an argon atmosphere to reduce the oxidization of the particles. The improvement was attributed to the improved crack and fracture resistance of Si NPs and the reduced diffusion distances.

A large number of studies have investigated the effects of size reduction down to nano-scale dimensions, with great improvements in cyclability. These include the mentioned 0D nanoparticles, 1D nanowires[59], nanorods[18], nanotubes[19] and 2D thin films[60]. Highly engineered 3D structures, such as particles with high porosity/voids[17] or a Si composite material containing a highly electric and/or Li-ion conductive material, are commonly used in order to improve the performance of the Si.[61,3,22] Si/C composite materials will be addressed in Section 2.4. Proposed reasons for increased performance vary and include: 1) increased fracture resistance, 2) strong adhesion to the current collector, 3) voids accommodating for volume expansion, 4) increase in electric and ionic conductivity and 5) higher stability of SEI layer.

Binders

Elastic polymeric binders play a crucial role in the fabrication of electrodes, as they give structural integrity, binding of the active material, and adhesion to the current collector.[57] Binders are therefore an important key in tackling the challenges that Si present during cycling. Increased attention to greener, water-soluble binders such as sodium carboxymethyl cellulose (CMC) and polyacrylic acid (PAA) with high compatibility to Si, have been seen. Mazouzi *et al.* demonstrated the importance of the pH in the slurry, in order to achieve covalent bonding between CMC and the Si surface.[62] At neutral pH, the silanol groups (Si-OH) at the Si surface are deprotonated and negatively charged. The isoelectric point of Si is ~3.5 in water. The carboxylate groups (R-COO^{-1}) of CMC are also negatively charged (deprotonated) at neutral pH with a pK_a value of ~3.5.[62] These negatively charged groups repel each other. However, by addition of a buffer solution (pH = 3) to the slurry, the groups can be protonated (Si-OH and R-COOH) and react in an esterification reaction to form a covalent bond (Si-OCO-R). This is referred to as surface-grafting. Compared to slurries at neutral pH, the acidic conditions have shown to give Si anodes with increased capacity retention.[62, 63] Bridel *et al.* also studied the CMC binder with a Si-anode and emphasized the importance of hydrogen bonding between the silanol groups (Si-OH) and the carboxyl groups (-COOH).[64] They proposed a self-healing mechanism, in which hydrogen bonds would break and reform as the Si expanded and contracted, which would be beneficial in the long-term cycling stability. The slurries were prepared at a neutral pH.

PAA also contains a carboxyl group that can take part in an esterification reaction with Si at acidic conditions. Foss *et al.* demonstrated improved cycling stability of micron-sized Si with the addition of an acidic buffer solution to the slurry, compared to neutral pH.[65] The proposed reason for increased stability was the esterification reaction and grafting on the Si surface, as seen in Figure 2.6. Numerous studies have shown improved capacity retention over 100 cycles for PAA-derived polymers compared to traditional binders such as CMC, alginate, and PVDF due to their superior mechanical strength.[66] However, the binder's interplay with the nature of the Si, electrolyte, additives, and SEI is highly complex and must be further studied.

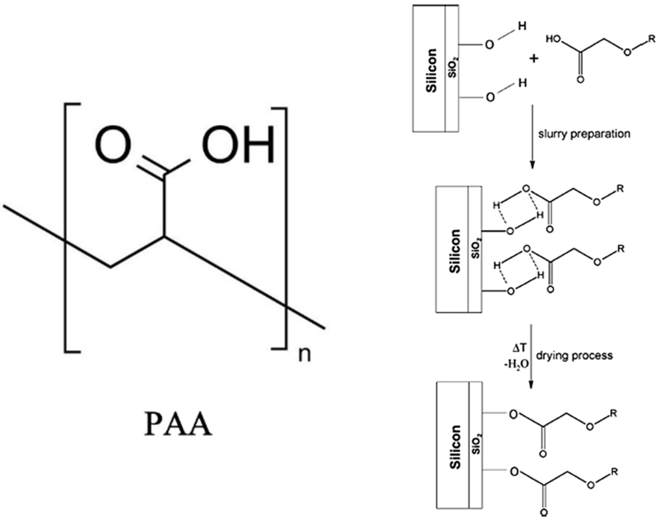

Figure 2.6: Structure of PAA and a illustration of the esterification reaction with PAA and silanol, leading to a surface grafting. Reprinted from Ref.[67].

Electrolyte additives

The addition of VC and FEC have shown to be an effective and easy strategy in improving the cycling performance of Si anodes and is therefore widely used in the testing of Si anode materials.[68] However, the reduction mechanisms and reasons for improvement are not agreed upon nor fully understood.[68,69] VC and FEC have shown to reduce before EC, and DFT calculations have shown lower LUMO energy levels for FEC and VC, compared to EC, which would favor their reduction at the anode.[23] Jaumann *et al.* reported the reduction of FEC and VC to occur at 1.47 V and 1.25 V (vs. Li/Li^+), respectively.[68] VC is already commercialized in LIBs due to the increase in CE and thermal stability seen for graphite anodes. Widely agreed upon is the fact that VC and FEC form stable and flexible layers on the Si surface, which help accommodate the volume changes during lithiation. Jaumann *et al.* report a dense and highly flexible polycarbonate (PC) layer as the result of VC-decomposition.[68] The PC-layer suppresses the formation of SEI, but reduces Li-ion conductivity and thereby the rate performance. VC is also thought to have a positive effect on the thermal stability of the cathode.

Etacheri *et al.* reported major improvement in cycling performance with the addition of FEC to the electrolyte, for SiNW. Post-mortem analysis with XPS and FTIR revealed a thin flexible film of polycarbonates on the Si surface, proposed to be a result of VC polymerization as FEC decomposes to VC and HF.[70] In addition, the defluorination to form HF increases the formation of LiF. The results reported by Jaumann *et al.* support this and propose that the formation of LiF nanocrystals enhances the Li-ion conductivity inside the SEI by creating defects in the dense and flexible PC layer.[71,68] However, the LiF-containing polymeric layer is stiffer and not as stable in terms of SEI formation compared to the one made from VC. In addition, LiF is an electronic insulator. The important effect of FEC on cycling stability has also been demonstrated for micron-sized Si by *Foss et al.*.[65] After numerous cycles with high stability, a drop in the capacity and increased polarization is common cycling behavior for Si with FEC-additive.[65,70,69] Jung *et al.* have shown that the number of cycles with relatively stable capacity is highly dependent on the amount of FEC added to the electrolyte. 19F-NMR analysis from Jung *et al.* also suggests that the FEC is consumed at the point where a rapid capacity drop is seen after the stable cycling.[69]

2.4 Si/C composite

Si/C composite materials have been heavily studied as a way of tackling the challenges that Si experience during cycling. By taking advantage of the intrinsically different material properties of Si and C, a superior anode material can be made. The properties of C differ heavily with the type of allotrope, however, in a Si/C the main types of C structures are amorphous (hard carbon), graphite, graphene, nanowires, and nanotubes. These are used due to their superior electric and ionic conductivity compared to Si, and therefore efficiently complements the high capacity of Si.[72] Higher conductivity and decreased internal resistance give better rate performance and less overpotential. These C materials have also favorable mechanical properties and are thought to buffer the volume changes during (de)lithiation. This leads to less SEI-cracking and higher CE, and ultimately retention of irreversible losses and longer cycle lives.[72,73] A chemically stable C shell around the Si surface can hinder the core's contact with the electrolyte. Thus, reducing side-reactions and stabilize the SEI layer. There is a long list of different Si/C anode designs, however, the focus going forward will be on core-shell structures in which a Si-core is coated with a C shell/layer.

2.4.1 Core-shell Si/C composites

Core-shell Si/C composites consist of a C shell with a Si core. The fabrication of core-shell Si/C composites is commonly achieved in a wet-chemistry synthesis (in-situ polymerization, sol-gel etc.) or a gaseous atmosphere (CVD) with a carbon precursor (CP) (sugars, resins, ethylene, etc.) Table 2.3 list different work done on core-shell Si/C. Most methods include a carbonization step in which the Si/CP is heated to several hundred degrees Celsius under an inert atmosphere (e.g. Ar), thus, driving out elements such as hydrogen and oxygen to leave a carbonaceous structure on the surface of the Si.[4] The type of CP, method, and carbonization temperature will influence the chemical composition, physical properties, and ordering of the final C layer.[74, 4]

The work of Liu *et al.* brought much attention as they made a Si/C with a yolk-shell design. Spherical Si NPs were encapsulated in a thin and conformal C shell with a void space in between to allow for volume expansion. This hinders the deformation of the shell or the SEI on the outside of the shell.[3] The yolk-shell structure was achieved by coating a sacrificial SiO_2 layer on the outside of the Si and then coating this surface with a polydopamine layer. After carbonization, the SiO_2 was etched away with hydrofluoric acid (HF) and the yolk-shell structure was obtained. The C layer was amorphous and $\sim$5-10 nm thick. This resulted in a high capacity anode with high CE and cycle life. The same group later developed a Si/C with a pomegranate-inspired design, based on their yolk-shell design.[22] After the SiO_2 layer was made, the particles were assembled into bigger clusters and coated with a resorcinol-formaldehyde (RF) resin. After carbonization, the same etching took place and left Si/C microbeads with a pomegranate-like structure. The surface for SEI formation was reduced compared to the yolk-shell design and showed exceptionally cycling stability at a high capacity (1160 mAh g^{-1} after 1000 cycles at 2100 mA g^{-1}), for low electrode loadings ($\sim$0.2 mg cm^{-2}). The work of Son *et al.* demonstrated Si/C composites with a graphene-coated Si core.[23] The coating was done by CVD, with methane as CP, and left a few layers of graphene on the Si surface. The best results were achieved with a Si/C containing 5 wt% C. High cycling stability was partly attributed to a proposed graphene interlayer sliding mechanism upon volume expansion of Si. A full-cell reached volumetric energy densities of 972 and 700 Wh/L at first and 200th cycle, respectively, about 1.5 times higher than commercial LIBs. Illustrations of the three designs are shown in Figure 4.16. Although promising results are frequently shown in the labs, the main commercialization challenge is cost. As Liu *et al.* express in their work on the pomegranate-like Si/C: *"However, we note that future work is needed to reduce the cost* *of starting materials such as the Si nanoparticles to meet commercial needs.".*[22] Figure 4.16 illustrates the three different Si/C structures mentioned above.

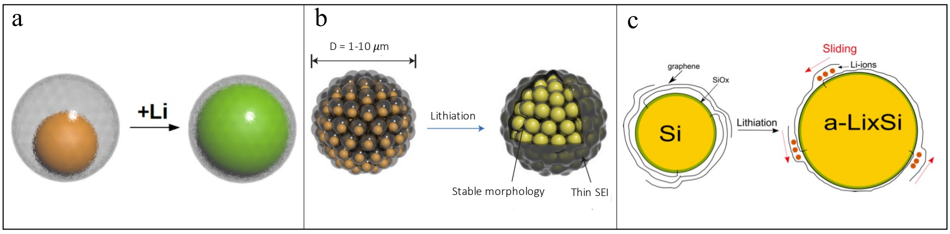

Figure 2.7: Illustration of the a) yolk-shell structure, b) pomegranate structure and c) graphene-coated structure. The illustrations show the volume expansion of Si at lithiation, going from left to right in the reactions. Adapted from Ref.[3, 22, 23, 39].

Table 2.3: Summary of core-shell Si/C composite materials with their respective synthesis method, CP, final wt% Si in composite, cycling current density and the capacity after n cycles. All studies used Si NPs.

Synthesis method	**Carbon precursor**	**Si (wt%)**	**Current density (mA g^{-1})**	**Capacity (mAh g^{-1}) after (n) cycles**	**Ref.**
Spray-pyrolysis	Citric acid	44	100	1489 (20)	75
Hydrothermal	Glucose	75	150	1100 (60)	76
In-situ polymerization	PZS polymer	78	500	1201 (40)	77
Pyrolysis	Polyvinylidene fluoride	95.7	50	1290 (30)	78
CVD	Toluene	37	100	767 (100)	79
CVD	Acetylene	30	250	1080 (200)	80
Alkaline etching	Dopamine	75	1000	804 (50)	81
Water-in-oil emulsions	Phenolic resins	77	2100	1160 (1000)	22
Sol-gel	Phenolic resins	81.7	500	1006 (500)	4

2.4.2 The resorcinol-formaldehyde route

Development and mechanism

The synthesis of core-shell Si/C composites, with a great increase in cycling performance, has been demonstrated in a facile, one-pot reaction solution with resorcinol-formaldehyde (RF) resin, at room temperature.[4, 82, 83] The synthesis involves a base-catalyzed polymerization reaction between resorcinol molecules and the cross-linking formaldehyde molecule, which forms a polymeric layer on the Si surface. The solvent solution is a mixture of water and ethanol with ammonium hydroxide (NH_4OH) as a base. A surfactant, cetyltrimethylammonium bromide (CTAB), is used to modify the electrostatic properties of the Si surface. The polymer-coated particles are carbonized to form a core-shell Si/C anode. A simplified overview of the synthesis is shown in Figure 2.8. An in-depth mechanism will now be given.

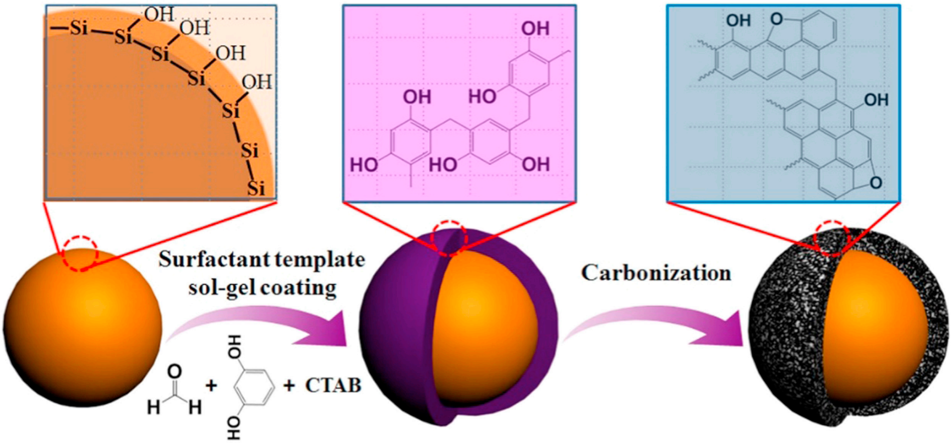

Figure 2.8: Illustration of the simplified steps in which core-shell Si/C is made by coating with RF resin and further carbonized. Reprinted from Ref.[4].

Pekala *et al.* first discovered the RF resin and used it to make organic aerogels under alkaline conditions, through polycondensation reactions similar to the sol-gel processing of silica (Stöber method).[84] Later, Liu *et al.* demonstrated a method of making spherical RF resin particles in the submicron range in a facile one-pot synthesis at room temperature.[85] The particles showed a narrow size distribution and simple size-tunability, with potential applications in bio-medicine, catalysis, super-capacitors, and LIBs, etc. Liu *et al.* describe the synthesis steps as follows: 1) emulsion droplets are first formed through the hydrogen bonding between water, ethanol, resorcinol, and formaldehyde, and 2) polymerization of RF takes place from the inside of the droplets, resulting in uniform colloidal spheres. A simplified 2-step mechanism is seen in Figure 2.9, in which a polymeric network is created. Firstly, formaldehyde is added to the resorcinol structure initiated by the base. Secondly, condensation reactions form a cross-linked structure connected by either methylene ether or methylene bridges as seen in Figure 2.9.[86]

The role of NH_4OH is crucial in two ways. Firstly, it initiates the polymerization by increasing the pH and the deprotonation of the resorcinol molecule. The deprotonation of the two alcohol groups in resorcinol has been determined to occur in the pH ranges of 8.4–9.6 and 10.4–11.6.[87] As a result, it initiates the addition reaction with formaldehyde, as seen in Figure 4.16. Secondly, the NH_4^+ adheres to the outer surface of the polymer spheres and therefore, kinetically, hinders agglomeration.[85] Liu *et al.* revealed high tunability in particle size as decreasing the ratio of alcohol/water, decreasing the amounts of NH_4OH or RF precursor leads to reduced particle sizes.[85]

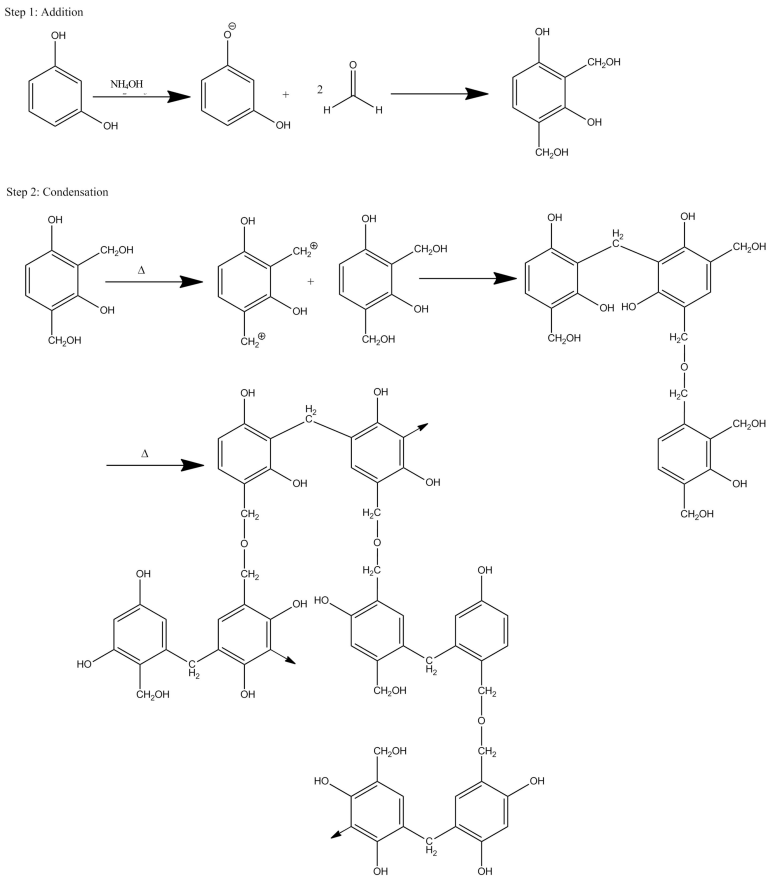

Figure 2.9: A simplified polymerization reaction with monomer resorcinol and cross-linker formaldehyde, in basic conditions. Reprinted from Ref.[86]

RF-coating

A method of C-coating inorganic structures with RF-resin was developed by Li *et al.* and Fang *et al.*.[88, 89] Both works demonstrated the importance of adding a surfactant molecule (CTAB) to the reaction solution in order to direct the growth of a polymeric RF-layer on the surface of the particles. Li *et al.* used spherical silica particles as the coating template and measured a negative zeta potential for the particles in the reaction solution (pH = $\sim$10.3), expected as the isoelectric point of colloidal silica is around 1.7-3.5.[90] Silica and Si contains surface silanol groups (Si-OH) that deprotonate in water. At this pH, the resorcinol is also negatively charged and the electrostatic repulsion force hinders adsorption to the surface.[88] The silica surface can be modified by the addition of the surfactant CTAB. The positively charged head group will adsorb to form a layer at the surface. A second layer of CTAB is energetically favored as the organic tail-groups associate with each other, forming a bi-layer as seen in Figure 2.10 a.[91] Li *et al.* demonstrated the change in zeta potential the concentration of CTAB was increased, according to Figure 2.10 b. The CTAB bi-layer allows for electrostatic attraction between the particle surface and the negatively charged resorcinol, which promotes polymerization at the surface and coating, confirmed by TEM imaging.[88] The measured zeta potential of an RF-coated silica particle was negative.[88] Liu *et al.* demonstrated that the coating thickness increased as resorcinol and formaldehyde were increased at a fixed ratio. Increased reaction time also increased the thickness. Fang *et al.* demonstrated RF-coating on non-spherical particles as well.[89] The concept of directed growth of polymer transfers to Si as well, as it is oxidized in air to form a thin layer of amorphous SiO_x at the surface.[92]

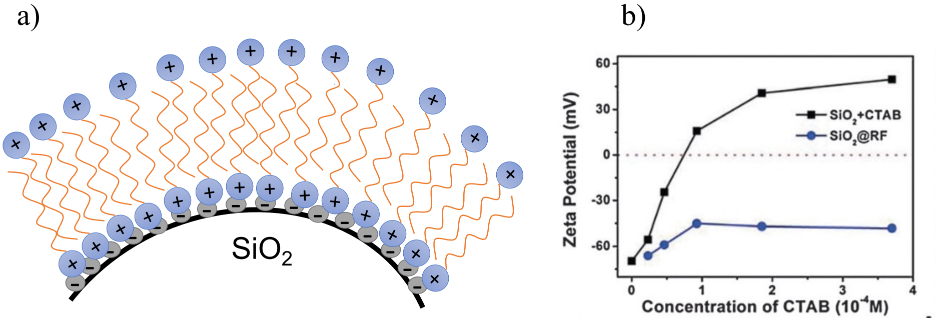

Figure 2.10: a) Illustration of the proposed CTAB bi-layer formation at the surface of silica in water. Bromine counter-ions are not included for simplicity. b) Zeta potential measurements in respect to the CTAB concentrations for silica and RF-coated silica. Reprinted from Ref.[88]

Si-RF anodes

Core-shell Si by RF-coating has been presented by Luo *et al.* and Fang *et al.*.[4,82] The work represents a far easier and cheaper alternative to highly engineered anode structures, such as the yolk-shell and pomegranate designs, while achieving high cycling stability. Luo *et al.* C-coated spherical nanosized c-Si (d = ~80 nm) with varying amounts of RF resin. The coating synthesis is in accordance with the method described previously for silica. After carbonization at 700°C, core-shell particles with C-coateds thicknesses in the range of 2-25 nm, was obtained. TEM-imagining revealed homogeneous and complete layers. The Si/C with a coating thickness of 10 nm (Si@10C), demonstrated superior electrochemical performance compared to pristine Si and other Si@xC, emphasizing the importance of an optimum C-coating thickness. The galvanostatic cycling data is shown in Figure 2.11. BET measurements revealed a microporous C structure. The capacity of Si@10C, after 500 cycles (0.5 A g^{-1}), was 1006 mAh g^{-1} compared to 205 mAh g^{-1} for the pristine c-Si NPs. The high stability was attributed to: 1) protection of the Si core and reduction of side reactions, 2) alleviation of internal stress during cycling avoiding fractures, 3) faster electron transfer, and 4) rapid Li-ion diffusion through the shell to the core due to microporosity. The surface area and total pore volume were found to be ∼129.9 m^2 g^{-1} and 0.11 cm^2 g^{-1}, respectively, with C content of 18.3 wt%. Luo *et al.* proposed that less than 10 nm C thickness was unable to sustain the strain relaxation upon cycling, causing pulverization of the particles. The thicker C-coating of 15 nm demonstrated high cycling stability but at a cost of a lower initial delithiation capacity (1473 mAh g^{-1}), due to the high C-content (48.8 wt%). The C-coating was determined to be amorphous by Raman spectroscopy and ^{13}C NMR spectroscopy revealed -OH-groups after carbonization under N_2 at 600°C. Carbonization at 900°C, lead to the disappearance of the same shift, and the cycling stability was significantly reduced. Luo *et al.* used both CMC and Na-alginate as binders and showed superior capacity retention for CMC compared to Na-alginate. The results emphasize the importance of the anode's surface properties as it interacts with the SEI and binder. The slurry composition contained 60 wt% Si or Si/C, but the electrode loadings were not reported.

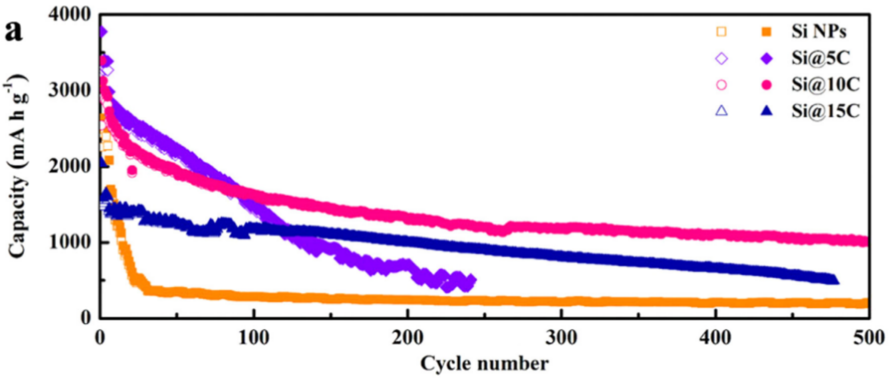

Figure 2.11: Capacity mAh g^{-1} as a function of the cycle number for half-cells with pristine Si NPs and Si NPs with C-coating thicknesses 5, 10, and 15 nm. Cycled at a current density of 0.5 A g^{-1}.

Lu *et al.* also demonstrated significant improvement in cycling stability for c-Si NPs (d = ∼100 nm) with C-coating from an RF-resin.[82] The group used a Na-alginate binder, a carbonization temperature of 800°C, and the slurry contained 70 wt% Si or Si/C. Galvanostatic cycling of half-cells with active material loadings of $\sim$1.7 mg cm^{-2} was done at a current rate of C/3 (1 formation cycle of C/20). A Si/C with 13.7 wt% C achieved a high specific capacity of 1107.5 mAh g^{-1} over 50 cycles, and nearly 1000 mAh g^{-1} over 200 cycles with CE of more than 99.6%. In contrast, the pristine c-Si NPs achieved <200 mAh g^{-1} after 20 cycles.[82] Both works above involve the coating of expensive spherical NPs, however, the recent work of Tzeng *et al.* demonstrated improved performance of C-coating with RF-resin on Si flakes, recycled from wastes of Si wafer manufacturing processes.[83]

2.4.3 Glucose route

C-coating Si with sugar represents a greener alternative to RF-resin, with promising improvement in the cycling performance.[93, 94] Hu *et al.* C-coated c-Si NPs (d = 20-50 nm) with glucose in a hydrothermal carbonization synthesis.[93] The method involved mixing glucose and Si in water into an autoclave and heating to 200°C for 12 h. In the process, glucose polymerize in a condensation reaction.[94] The obtained particles were then carbonized at 750°C (N_2) to form core-shell composites. Raman spectroscopy demonstrated an amorphous C layer (hard carbon) and TEM imaging revealed a complete layer (10 nm), consisting of amorphous SiO_x and C. The C layer lacked homogeneous thickness and on some particles, it consisted of only one to three graphene layers. The total C content was determined to be 25 wt%. The result was a Si@SiO_x/C nanocomposite, which outperformed the pristine Si NPs in cycling performance. Si@SiO_x/C half-cells achieved a reversible capacity of 1100 mAh g^{-1} at a current density of 150 mA g^{-1} with no further decay for about 60 cycles. The pristine Si suffered large capacity losses with a reversible capacity of around 200 mAh g^{-1}, after 60 cycles. The slurry contained 70 wt% active material (Si or Si@SiO_x/C), PVDF was used as the binder, but the electrode loadings were not reported.

Shao *et al.* synthesized core-shell Si obtained in a similar manner as mentioned above.[94] However, a non-ionic copolymer surfactant molecule (Pluronic F127) was also added. After carbonization at 800°C the surfactant molecule yielding a porous C shell. An overview of the synthesis is given in Figure 2.12. TEM imaging determined the C shell to have a thickness in the range of 15-20 nm with pore-diameters of 3-5 nm. The final composite had a C content of 34.5 wt% and surface area of 197.9 m^2 g^{-1}, compared to 31.0 m^2 g^{-1} for the pristine Si. Galvanostatic cycling of half-cells at a current density of 0.4 A g^{-1}, showed superior cycling stability for the composite, compared to pristine. A reversible capacity of 1607 mAh g^{-1} after 100 cycles with a CE of 99.1 % was achieved.

The pristine Si achieved 490 mAh g^{-1} after 20 cycles. The slurry contained 70 wt% Si or Si/C and active material loadings for Si and Si/C was 0.7 mg cm^{-2} and 0.5 mg cm^{-2}, respectively. CMC was used as the binder.

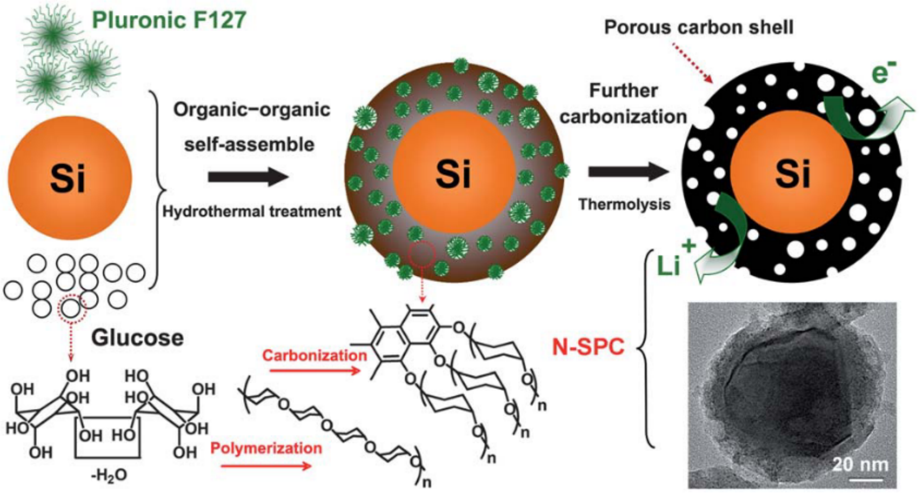
Pluronic F127
Si
Glucose
Organic−organic
self-assemble
Hydrothermal treatment
Si
Porous carbon shell
Further
carbonization
Thermolysis
Si
e⁻
Li⁺
N-SPC
Carbonization
Polymerization
-H₂O
20 nm

Figure 2.12: Shematic overview of the synthesis of core-shell Si/C with glucose as CP. Reprinted from Ref.[94]

A simple method of C-coating silica particles with sugars have been reported by Blanco *et al.* and involves the following steps: 1) dissolution of sugar (eg. glucose/sucrose) in distilled water, 2) addition of silica particles, 3) 30 min ultrasonication, 4) 2 h of continuous stirring on a hot plate at 60°C, 5) manual grinding with an agate mortar, and 6) carbonization at 850°C or 1200°C.[95, 96] An adaptation of this procedure was used in this thesis. Blanco *et al.* demonstrated high SSAs and microporosity when glucose/silica was annealed at 850°C. At 1200°C, the total micropore area was significantly reduced and higher ordering of the C layer was obtained. By varying the amounts of sugar precursor, an optimum amount of about 15 wt% C in the final composite was determined to have the best electrochemical performance.[96]

C-coatings with glucose and RF-resin have amorphous structures (hard carbon). Dahn *et al.* describe the structure of hard carbon as *"small single layers of C arranged more or less like a house of cards."*.[97] They demonstrated capacities in the range of ∼200-600 mAh g^{-1} for hard carbons made from epoxy-novolac resins heated between 900°C-1100°C. Single layers in the hard carbon are proposed to allow for Li-adsorption on both sides.

Therefore, showing higher capacity compared to graphite. Dahn *et al.* plotted the capacity as a function of single-layer fraction and demonstrated higher capacity as the fraction increased.[97]

2.5 Characterization techniques

2.5.1 Material characterization

X-ray diffraction (XRD)

XRD analysis is an analytical technique that can be used to determine material properties such as crystallographic structure, phases and crystallite sizes. XRD peaks are produced by constructive interference of a monochromatic beam of X-rays scattered at specific angles from each set of lattice planes in a sample. Consequently, the XRD pattern is the fingerprint of periodic atomic arrangements in a given material.[98] An X-ray powder diffraction pattern is a plot of the intensity of X-rays scattered at different angles by a sample. The intensity, usually recorded as "counts", is plotted as a function of the angle. The width of the peaks can be used to estimate the crystallite size of the powder, using the Scherrer equation:

$$\tau = \frac{K\lambda}{\beta \cos\vartheta} \tag{2.14}$$

where τ is the average crystallite size, K is a constant, λ is the X-ray wavelength, B is the peaks full-width at half-maximum (FWHM) and ϑ is the scattering angle in radians.[99]

Brunauer-Emmett-Teller (BET)

The physical adsorption (physisorption) of a gas to a solid surface is a result of weak interactive van der Waals forces and can be utilized to determine the specific surface area (SSA) and surface porosity of a specimen. The number of gas molecules (adsorbate) adsorbed on the surface can be described by an adsorption isotherm. The adoption isotherms is the amount adsorbed at equilibrium at a constant temperature as a function of the pressure of the gas.[100] The gas used is often nitrogen, adsorbed at its boiling point of -196°C. There are many models or isotherms that describe the amount adsorbed, however, the BET equation is commonly used and follows,

$$\frac{p}{V(p_0 - p)} = \frac{1}{V_\mathrm{m}C} + \frac{C-1}{V_\mathrm{m}C}\frac{p}{p_0} \tag{2.15}$$

where p is the pressure, p_0 is the saturated vapor pressure of the gas, V is the volume of gas adsorbed, V_m is the volume of adsorbate equivalent to a monolayer coverage and C is a constant.[100] Equation 2.15 can be linearized to determine the V_m and the SSA can then be calculated from the cross-sectional area of the gas molecule, assuming close-packing at the surface. The shape of the isotherms obtained from physisorption measurements can be used to describe the surface structure of the specimen. The six types of isotherms (IUPAC classification) are characteristic of materials that are microporous (type I), nonporous or macroporous (types II, III, and VI), or mesoporous (types IV and V), as shown in Figure 2.13.[101]

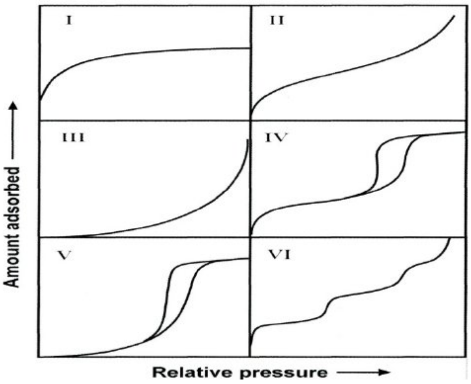

Figure 2.13: Classification of isotherms. Reprinted from ref[101].

Energy-dispersive X-ray spectroscopy (EDS)

EDS is an analytical technique used for the elemental analysis of a specimen. The technique is often coupled with an SEM and, commonly, involves focusing an electron beam on the specimen. The electron beam excites electrons which leaves "positive holes" that are filled by the relaxation of an electron from a higher energy orbital. This relaxation releases an X-ray characteristic of an element. The X-rays hit a detector and signals are interpreted by a software. Elemental maps can be constructed by scanning the electron beam over a specimen.[102] EDS is a semi-quantitative elemental analysis technique with limitations in terms of specimen matrix and morphology. The penetration of the electron beam is dependent on the acceleration voltage but is in the micron range. A particle specimen with a sub-micron coating will therefore have elemental counts from its core and underlying specimen holder.[103]

2.5.2 Electrochemical characterization

Galvanostatic charge-discharge

Galvanostatic charge-discharge (or cycling) of batteries is a method of running a set current rate through a battery as a function of time. The desired charge and discharge current might be expressed as a C-rate which is based on the expected capacity of a cell. In a half-cell, a working electrode is cycled with Li-metal as counter-electrode, and they are therefore not balanced in terms of capacity. The Li-metal electrode has "unlimited" lithium ions and the C-rate is therefore based on the expected capacity of the working electrode. By assuming a set capacity for all electrodes, the charge/discharge rate can be given as a current density (A g^{-1}). The direction of current is programmed to change within a set of values (time and/or voltage) The voltages are known as cut-off voltages. The measured capacities at the cut-off voltages can be plotted as a function of the cycle index. The plots are used to describe the cycling behavior and performance of a cell and working electrode.

Internal resistance

During a galvanostatic cycling program, the internal resistance (IR) of the battery cell is often measured, e.g., after every cycle. By plotting IR as a function of the cycle index, it can be used as a supporting tool in determining the behavior of a cell. An increase in the IR is often correlated with a decrease in the capacity or extensive SEI growth.[65, 104] The measurement is done by applying a pulsed discharge and charge current ($\mathrm{I_{IR}}$), and the voltage (V) responses at $\mathrm{I_0 + I_{IR}}$ and $\mathrm{I_0\text{-}I_{IR}}$ are measured. Over a set number of pulses n, e.g. 10, the IR is calculated as follows:

$$\mathrm{IR} = \frac{1}{\mathrm{n}} \sum_{\mathrm{i=1}}^{\mathrm{n}} \left[\frac{\mathrm{V^i_{I_0+I_{IR}}} - \mathrm{V^i_{I_0-I_{IR}}}}{2\mathrm{I_{IR}}} \right] \tag{2.16}$$

where the IR is given in Ohm. However, Equation 2.16 is only valid for ideal resistors, and not a battery cell. Instead, electrochemical impedance spectroscopy must be used in order to describe a cell's electrochemical mechanisms, reaction kinetics, and internal resistance.[105]

3. Experimental

3.1 Coating methods

This section includes two different methods to achieve core-shell Si/C composites: 1) coating with resorcinol-formaldehyde and 2) coating with glucose. The first method was only done with a micron-sized industrial-grade Si (m-Si). The second method included the m-Si and a nano-sized industrial-grade Si (n-Si).

3.1.1 Chemicals and materials

The chemicals and materials used in experiments are: m-Si (Elkem), n-Si (Elkem), resorcinol ($\geqslant$ 99%, Sigma Aldrich), D-(+)-glucose monohydrate (Merck), formaldehyde (37 wt% in H_2O + 10-15wt% methanol, Sigma Aldrich), polyacrylic acid (PAA) (Mw 250,000, 35 wt% in H_2O, Sigma Aldrich), hexadecyltrimethylammonium bromide ($\geqslant$ 98%, Sigma Aldrich), graphite (C-NERGY KS 6L, Timcal), carbon black (C-NERGY Super C65, Timcal), lithium foil (99.99 %, LinYi Gelon LIB Co, 15 mm in diameter and 250 µm), Argon-gas ($\geqslant$ 99%, AGA), dendritic copper-foil (16µm thick, dendritic, Schlenk), electrolyte "S1" (1.2M $LiPF_6$ in 3:7 EC/EMC, 2 wt% VC and 10 wt% FEC, Solvionics), polyproylene separator (25µm thick, Celgard 2400), pH-paper (Tritest, pH 1-11, Macherey-Nagel), Lithium Nickel Manganese Cobalt Oxide electrode (NMC 111, aluminium current collector, Customcells®). Caps, spacers, and springs were all stainless steel from Hohsen Co. All chemicals were used without further purification.

3.1.2 Coating with resorcinol-formaldehyde resin

Coating of the m-Si with an RF-resin was based on the work of Luo *et al.*.[4] A simplified overview is given in Figure 3.1. The procedure can be divided into five steps: 1) 1 g of Si and 1 g of CTAB were added to 90 mL of DI water and the suspension was vigorously stirred and ultrasonicated with a probe (pulse mode 4/40% output, Sonoplus Bandelin) for 30 min. 2) 30 mL of ethanol and a calculated amount of resorcinol were added (Table 3.1). The solution's pH was measured with pH paper, before adding 0.3 mL of ammonium hydroxide. The pH was again measured to verify alkaline conditions and the suspension was set to stir for 30 min. 3) The beaker was then placed in an oil bath that was pre-heated to 35°C. Then, a calculated amount (Table 3.1) of formaldehyde was added dropwise using a pipette. Both the oil bath and suspension were kept under continuous stirring (300 rpm) for 6 h. The beaker was covered with parafilm to limit evaporation losses. 4) The beaker was then taken out of the oil bath and the suspension was left to age for 16 h, at ambient conditions and no stirring. 5) The suspension was then centrifuged for 5 min at 4400 rpm in a centrifuge (Eppendorf). After, the supernate was decanted off. The particles were washed with DI-water and redispersed by shaking, before 5 min centrifugation. This process was repeated twice, however, ethanol was used the last time. The particles were left to dry in a fume hood for at least 16 h before further drying and carbonization in a tube furnace. This step will be described in section 3.1.4. The amounts of formaldehyde (F) and resorcinol (R) were varied but at a fixed molar ratio of F/R = 1.4. However for the sample labeled "m-Si@RF_40", this ratio was 2.1, due to an error in the calculation. Table 3.1 lists the targeted amounts.

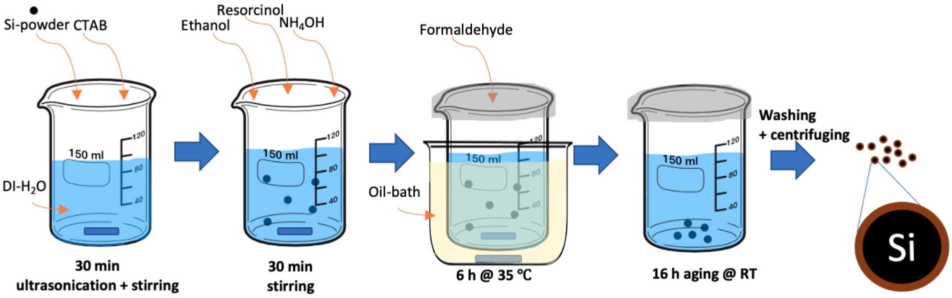

Figure 3.1: A simplified overview of the reaction steps of making a Si/RF-resin composites.

Table 3.1: The targeted amounts of all substances involved in the synthesis involving RF-resin. The labeling refers to the wt% of resorcinol in relation to only Si, e.g. "m-Si@RF_40" contains 60 wt% m-Si and 40 wt% resorcinol. For Si@RF_0, no resorcinol or formaldehyde was added and "RF-resin" does not contain Si.

Label	Si (g)	R (g)	F-solution (mL)	CTAB (g)	H_2O (mL)	Ethanol (mL)	NH_4OH-solution (mL)
m-Si@RF_0	1.00	-	-	1.00	90	30	0.30
m-Si@RF_40	1.00	0.67	0.95	1.00	90	30	0.30
m-Si@RF_60	1.00	1.50	1.43	1.00	90	30	0.30
m-Si@RF_80	1.00	4.00	3.81	1.00	90	30	0.30
RF-resin	-	6.00	5.72	1.00	90	30	0.30

3.1.3 Coating with glucose

Coating of the m-Si and n-Si with glucose was based on the work of Blanco *et al.*[96] A simplified overview is given in Figure 3.2. The procedure follows three main steps: 1) Glucose monohydrate (G) was dissolved in 5 mL DI-water and added to a suspension of 1.5 g Si in 10 mL ethanol. The suspension was stirred and ultrasonicated for 30 min. 2) A hotplate was pre-heated to 70°C and the ethanol-H_2O-Si-G-suspension was transferred to an Al-foil insulated glass beaker and put on the hotplate. After 1-2 hours of solvent evaporation, under continuous stirring (300 rpm), a "honey-like" substance was obtained. 3) The mixture was transferred to an agate mortar and hand-ground until it dried to a powder (~30 min). The amount of glucose monohydrate was varied while other species were kept constant for all samples. However, n-Si was received as a slurry containing 59.9 wt% isopropanol (IPA) and 40.1 wt% n-Si. Therefore 3.74 g of slurry (1.50 g n-Si) was measured out in step 1. Table 3.2 lists the targeted amounts. Pure glucose monohydrate was also carbonized as a reference.

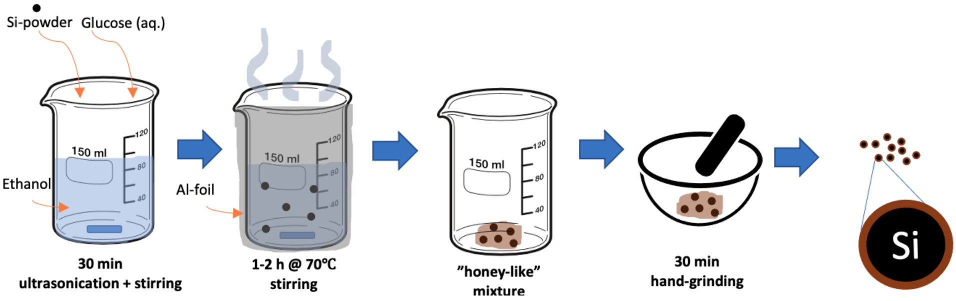
Si-powder
Glucose (aq.)
Ethanol
150 ml
120
80
40
30 min
ultrasonication + stirring
Al-foil
1-2 h @ 70°C
stirring
"honey-like"
mixture
30 min
hand-grinding
Si

Figure 3.2: A simplified overview of the reaction steps of making a Si/glucose composites.

Table 3.2: The targeted amounts of all substances involved in making a Si/G composite. The labeling refers to the wt% of G in relation to only Si, e.g. "m-Si@G_40" contains 60 wt% Si and 40 wt% G. For m and n-Si@RF_0, no G was added.

Label	Si (g)	Glucose (g)	DI-H_2O (mL)	Ethanol (mL)
m-Si@G_0	1.50	-	5.00	10.00
m-Si@G_20	1.50	0.38	5.00	10.00
m-Si@G_40	1.50	1.00	5.00	10.00
m-Si@G_60	1.50	2.25	5.00	10.00
n-Si@G_0	1.50*	-	5.00	10.00
n-Si@G_20	1.50*	0.38	5.00	10.00
n-Si@G_40	1.50*	1.00	5.00	10.00
n-Si@G_60	1.50*	2.25	5.00	10.00

*Target was 3.74 g of an IPA/n-Si-slurry (59.9 wt%/40.1 wt%).

3.1.4 Carbonization

All powders in Table 3.1 and 3.2were further dried and carbonized in a tube furnace (Nabertherm). Alumina crucibles were used to hold the powders. The furnace tube was evacuated to <10^{-1} bar and refilled with argon gas and the procedure was repeated twice. A slow and steady flow of argon through the tube ensured an inert atmosphere and exhaustion of gaseous species. The samples were heated to 120°C at a rate of 5°C/min and held for 6 h to dry the powders. Further, the samples were heated to 820°C at 5°C/min and held for 2 hours in order to carbonize the samples. Samples were cooled to RT at a rate of 10°C/min. Figure 3.1.4 shows the carbonization profile used for all samples.

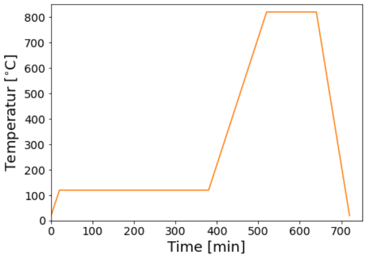

Figure 3.3: Temperature profile of the carbonization in a tube furnace.

Component	Mass [wt%]
Si or Si/C	60
PAA-binder	15
Carbon black	15
Graphite	10

Table 3.3: The targeted anode composition.

3.1.5 Ball-milling

After carbonization, the Si/C composites obtained from glucose were ball-milled in a planetary ball mill (Fritsch Pulverisette 7 Micro Mill). The milling vial volume was 80 mL and zirconia balls (10 mm) were used in a ball-to-powder mass ratio of 20:1. The milling was done in an ambient atmosphere for 2x30 min at 250 rpm. In between the two runs, the powder was scraped from the walls and mixed around. Thereafter, the powders were then sieved in a "tea-sieve" to avoid big hard carbon particles.

3.2 Electrode fabrication

A water-based slurry with the species that make up the anode was mixed in two steps and then cast onto a copper (Cu) current collector. 1) Polyacrylic acid (PAA) binder, DI-water, and a buffer solution of citric acid (aq.) and potassium hydroxide (aq.) (pH $\sim$3) was measured and mixed in a planetary Thinky mixer (ARE-250CE, Thinky Co.) for 2 min at 2000 rpm. 2) Carbon black (CB), graphite (Gr), and Si or Si/C were added to the binder solution. A zirconia ball was added to increase the homogeneity of the slurry, as it was further mixed for 7 minutes, at 2000 rpm. A dendritic Cu-foil (18 µm thick, Schlenk) was used as substrate and a Hohsen MC-20 Mini Coater with a 10 cm wide doctor-blade was used to cast the anode layer. Castings were done with a doctor-blade height in the range of 12.7-25.4 µm (0.5-1 milli-inch) at a speed of $\sim$4.5 mm/s. The casts were left to dry overnight in a fume hood and then dried *in vacuo* at 120°C for 3 hours. Table 3.3 lists the targeted anode layer composition after drying, neglecting the contribution from solids in the buffer solution.

3.3 Cell-assembly

Anode electrode disks (⌀=15 mm) were punched out and weighed with a targeted active material (AM) loading of ∼0.8 mg cm^{-2}. "Active material" includes the Si or Si/C and the graphite. The Si/C composite anode electrodes were also increased in loadings, in relation to their C content, to have similar Si-loadings (∼0.7 mg cm^{-2}). The electrodes were left *in vacuo* overnight before taken directly inside an Ar-filled glovebox (MBRAUN), without exposure to ambient conditions. Coin-cells (CR2023) were assembled in the following configuration: positive cap, electrode (⌀=15 mm), 18 µL electrolyte, polypropylene separator (⌀=18 mm), gasket, 18 µL electrolyte, counter electrode (⌀=15 mm), spacer, wave spring and negative cap. Thereafter, the cells were sealed with a cell crimper (Hohsen Co.). In a half-cell, Li-foil was used as a counter electrode (vs. Si or Si/C). The Li-foil surface was scraped with a scalpel before assembly. In a full-cell, NMC-111 (1 mAh cm^{-2}) was the first electrode (vs. Si or Si/C). The electrolyte, "S1", was a custom mixture of 1.2M $LiPF_6$ in 3:7 EC/EMC with 2 wt% VC and 10 wt% FEC (Solvionics). The caps, spacer, and spring were all stainless steel from Hohsen Co.. Three coin-cells were made for most Si- or Si/C electrodes tested.

3.4 Electrochemical testing

The electrochemical testing was done on Arbin BT200 battery testers coupled with Mits Pro computer software. All channels were placed in temperature-controlled cabinets and with a constant temperature of 25°C. The python script "Cellpy" (made by Jan Petter Mæhlen, IFE) was used to extract and handle the data from Arbin. Note: Due to a malfunction of one of the Arbin battery testers, reliable results for coulombic efficiencies could not be obtained for all cells. All cycling schedules started with a 6 h rest step to ensure wetting of electrodes.

3.4.1 Galvanostatic cycling

Half-cells were long-term galvanostatic cycled with 9 formation cycles with a current density of 0.16 A g^{-1} (C/20) between 0.05 and 1.0 V vs. Li^+/Li. Followed by 300 cycles at 1.6 A g^{-1} (C/2) between 0.05 and 1.0 V vs Li^+/Li. In addition, IR measurements with 10 pulses according to Equation 2.16 were done after the initial rest step and after every delith step. A rest step of 15 min was also used after every (de)lithiation. Note that some half-cells cycled with three formation cycles and are not compared to cells with nine.

3.4.2 Rate-testing

The rate-testing of half-cells was done by galvanostatic cycling at different current densities. The cells were cycled according to the following schedule: 13 cycles at 0.16 A g^{-1} (C/20), followed by 5 cycles at 0.31 A g^{-1} (C/10), 0.62 A g^{-1} (C/5), 1.6 A g^{-1} (C/2), 3.1 A g^{-1} (1C), 6.2 A g^{-1} (2C), respectively. Lastly, continuous cycling at 0.62 A g^{-1} (C/5) followed. All cycles were between 0.05 and 1.0 V vs. Li^+/Li. IR measurements and 15 min rest steps were used after every (de)lithiation step. Two cells of each electrode were made for the rate-testing.

3.4.3 Full-cell testing

Commercial NMC 111-cathodes and Si or Si/C anodes were punched out (⌀=15 mm). The target was a capacity ratio of $Q_{\mathrm{tot,anode}}/Q_{\mathrm{tot,cathode}} = 1.2$, to avoid Li-plating. The assumed capacity of Si was 3579 mAh g^{-1}. In order to determine the capacity of Si/C composite anodes, the capacity was based on their Si and graphite content, neglecting the contribution from the hard carbon. Therefore a higher anode loading was used for the composite anode. The galvanostatic cycling started with a lithiation at 7.25 mA g^{-1} followed by a lithiation-taper step at 2.9 mA g^{-1}, both to a cut-off voltage of 4.3 V. After delithiation at 7.25 mA g^{-1} to a lower cut-off voltage of 3 V, the schedule followed: 2 cycles at 14.5 mA g^{-1}, 2 cycles at 29 mA g^{-1} and continuous cycling at 72.5 mA g^{-1}. IR measurements and 15 min rest steps were used after every (de)lithiation step.

3.5 Material characterization

3.5.1 X-ray diffraction (XRD)

XRD analysis was used to study the crystallinity of the two pristine Si-powders. Measurements were done between 10° to 80° in a D2 Phaser XE-T edition (Bruker) with a CuK_α X-ray source. Si-powder was mixed with isopropanol and deposited on a Si single-crystal and dried before analysis. The powders were also analyzed after going through the carbonization step described in section 3.1.4.

3.5.2 Field emission scanning electron microscopy (FE-SEM)

An FE-SEM (JEOL JSM-7900F) was used in order to study the size and morphology of the different powders. The FE-SEM samples were prepared by adding ∼5-10 mg of powder to ∼2 mL ethanol and ultrasonicated for ∼30 s (pulse mode 2/10% output). Then, 2-5 drops were added onto a lacey carbon Cu-grid (400 Mesh, agar scientific) and left to dry in ambient conditions. The acceleration voltage was set to 10 kV at a working distance of ∼9 mm.

3.5.3 Energy-dispersive X-ray spectroscopy (EDS)

An EDS detector (Oxford instruments), coupled with the FE-SEM, was used to perform elemental analysis of the powder samples. Element mapping was used to study the positions of Si, C, and O in relation to each other, to verify the presence of the surface coating. The maps were constructed using the AZtec EDS software. The acceleration voltage was set to 10 kV at a working distance of ∼9 mm.

3.5.4 Zeta potential measurements

Zeta potential measurements for m-Si were performed with and without CTAB in water. Si (0.5 g) and CTAB (0.5 g) were added to 45 mL of DI water and vigorously stirred for 30 min. The suspension was diluted 1:10 in DI water and added to a zeta potential cuvette

(DTS1070). Three measurements were done at 150 V, in a Zetasizer nano (Malvern). The same procedure was done for the suspension without CTAB.

3.5.5 Flash elemental analysis

Carbon content was determined by burning the samples at 1700°C in a Flash EA elemental analyzer (Thermo Fisher Scientific). CO_2 and N_2 are flushed into a DELTA V™ isotope ratio mass spectrometer (Thermo Fisher Scientific), in which their amounts are determined. The water is trapped on $Mg(ClO_4)_2$. All results are plotted on a calibration line calculated from the analysis of international reference material analyzed in each sequence. For analytical control, a third reference material is run as unknown in all sequences. The value of this third reference material is reported with standard deviation to give accuracy and precision of the analysis. The analyses were performed by Ingar Johansen (researcher, IFE).

3.5.6 Brunauer–Emmett–Teller (BET)

BET surface area analyses were done in order to measure the specific surface area (SSA) of the Si or Si/C powders. The measurements were done using a 3Flex analyzer (Micromeritics) and the powders were degassed at 300°C under vacuum overnight. The surface properties were determined by N_2 physisorption at a temperature of -196°C (77K). The analyses were performed by Saima Sultana Kazi (engineer, IFE).

3.5.7 Transmission electron microscopy (TEM)

The powders were dispersed in isopropanol and ultrasonicated for 10 – 15 min to avoid agglomeration. A droplet was transferred to a holey, amorphous carbon coated Cu TEM grid. TEM was performed with a double Cs aberration corrected cold FEG JEOL 200FC, operated at 200 kV. This instrument is equipped with a large solid angle (covering 0.98 sr solid angle) Centurio detector for energy dispersive X-ray spectroscopy (EDS) and a GIF Quantum ER for electron energy loss spectroscopy (EELS). EDS and EELS mapping were performed simultaneously in scanning transmission electron microscopy (STEM) mode. The analyses were performed by Per Erik Vullum (Senior researcher, SINTEF).

4. Results

The results are presented in three main parts: Firstly, the material characterization and electrochemical testing of the pristine industrial Si powders will be presented. Secondly, the material characterization and electrochemical testing of Si/C composite materials, made from an RF-resin and the micron-sized, m-Si, will be presented. Lastly, the electrochemical testing of Si/C composites made with glucose as a carbon precursor for both industrial powders will be presented.

4.1 Industrial grade Si

4.1.1 Material characterization

SEM

The size and morphology of the "as-received" pristine m-Si and n-Si, were determined by SEM. The SEM images revealed irregular particle morphologies for both powders, as seen in Figure 4.1 a) and b). Rough particle edges were also observed for both. The particle size distributions (PSD) obtained from SEM images are presented in Figure 4.2 a) and b). The m-Si powder had a wide PSD and included a high number of sub-micron particles. These particles were often seen on the surfaces of the micron-sized particles (∼1-8 µm). The n-Si have a narrower PSD, with a size range of ∼100-500 nm.

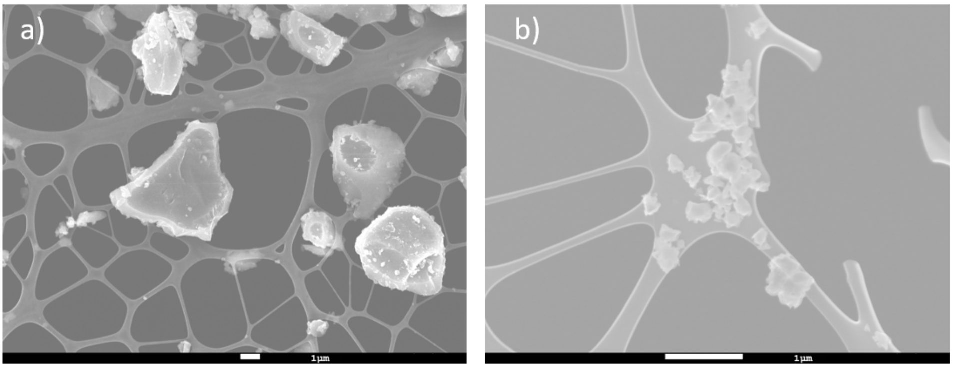

Figure 4.1: SEM-image of a) m-Si and b) n-Si. Both scale bars are 1 µm.

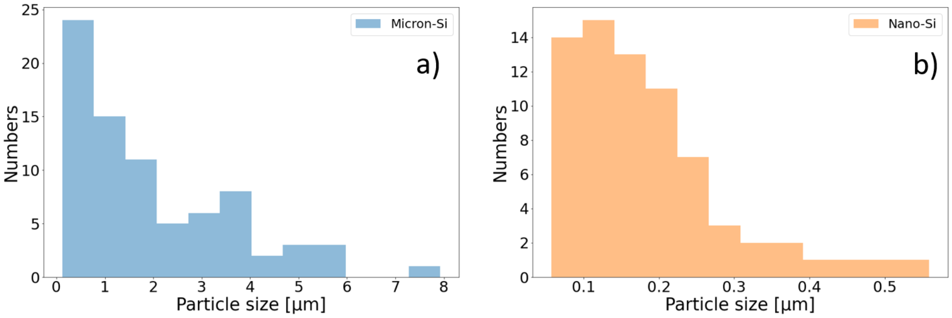

Figure 4.2: Particle size distribution of a) micron-Si and b) nano-Si determined from SEM-images.

XRD

The XRD diffractograms for m-Si and n-Si are shown in Figure 4.3. Both Si powders are crystalline with peaks at around $2\vartheta = 28°$, 47°, 56°, 69° and 76°. The peaks correspond to the crystal planes of (111), (220), (311), (400), and (331), respectively.[106] Three small peaks at around 26°, 42°, and 51° were also observed. EDS-analysis have shown traces of Al, S, and K impurities for both powders. A small amount of Cr was also detected in the m-Si. The peaks of n-Si are slightly shifted to higher degrees and are broader compared to the m-Si. Table 4.1 lists the full-width at half-maximum (FWHM) of the (111)-peak for both Si powders. The BET specific surface areas (SAA) of the powders were determined to be 13.7 and 41.7 $m^2\ g^{-1}$ for m-Si and n-Si, respectively, as seen in Figure 4.4. The adsorption/desorption isotherms were characteristic of a non- or macro-porous material, as seen in Figure A.1, in Appendix.

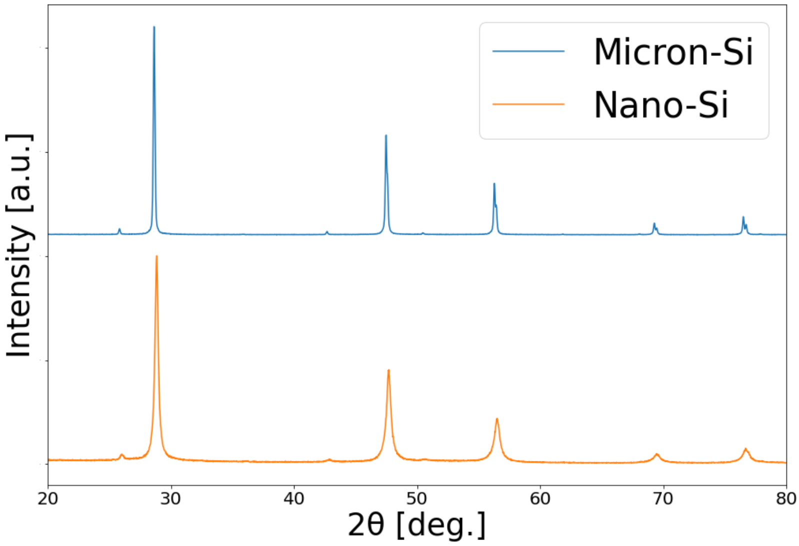

Figure 4.3: a) XRD-diffractograms of m-Si and n-Si.

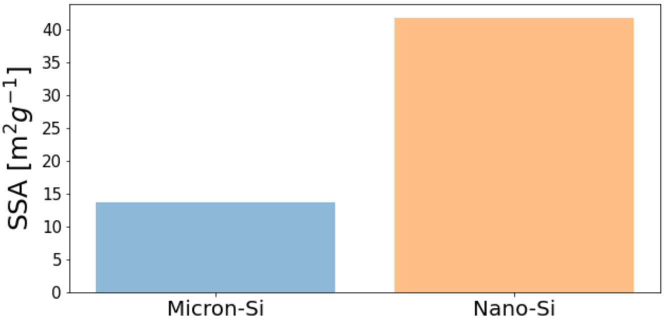

Figure 4.4: BET specific surface area (SSA) for m-Si and n-Si.

4.1.2 Galvanostatic cycling

Electrodes were made with the pristine Si powders and galvanostatically cycled in half-cells. The specific delithiation capacities per gram active material (Si + graphite) were plotted as a function of cycle index and are shown in Figure 4.5. The average initial capacities were 3235±119 and 2105±271 mAh g^{-1} for the m-Si and n-Si, respectively. A slight increase in capacity was seen for both powders in the second cycle, followed by a large capacity drop as the cycling current was increased after the third formation cycle. After around 20 cycles the capacities stabilized at around 50% of their respective initial capacities. Rapid capacity losses were seen after around 40 and 50 cycles for n-Si and m-Si, respectively. However, large variations between the cells were seen, demonstrated by the large standard deviations after ∼50 cycles for both powders, as seen in Figure 4.5. The initial CEs were 89.8±0.4 and 81.5±1.3% for the m-Si and n-Si, respectively. A decrease in the CE was also seen as the current was increased before it stabilized at ∼99.5% for both powders in cycle 10.

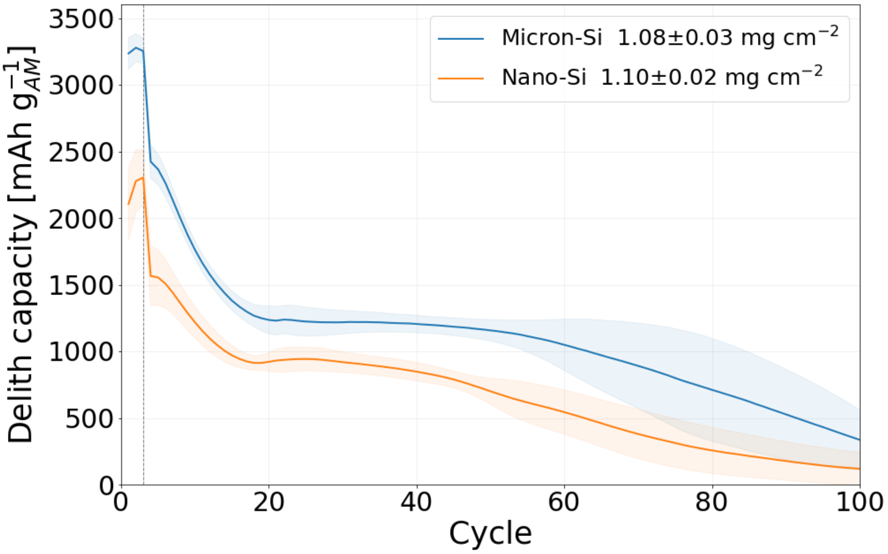

Figure 4.5: The galvanostatic cycling of m-Si and n-Si half-cells. The values are an average of five cells each, and plotted with the standard deviation. The cycling included three formation cycles 0.16 A g^{-1} (C/20) followed by 1.6 A g^{-1} (C/2), marked by a bold grey vertical line.

Figure 4.6 a) shows the voltage curves for the first three cycles of m-Si. As the current was applied, a quick voltage drop to $\sim$0.1 V, was observed. The lithiation proceeded at this single voltage step as the Si was lithiated to the cut-off voltage of 50 mV. A significant difference was seen in the voltage curves between the first and subsequent cycles. After the first cycle, the lithiation mainly occurred at two voltage steps. This distinct difference was not as apparent for the n-Si, as some lithiation also occurred at a higher voltage, as seen in Figure 4.6 b. In order to illustrate this difference, the differential capacities, for the first three cycles, were plotted as a function of the voltage, as shown in Figure 4.7 a) and b). For m-Si, the lithiation occurred at $\leq$0.1 V, followed by a narrow delithiation peak at $\sim$0.45 V. From the second cycle, the lithiation was represented by two peaks: a broad doublet at $\sim$0.25–0.3 V and at $\sim$0.1. The delithiation was represented by two relating broad peaks at $\sim$0.27 V and $\sim$0.45. This occurs as most of the Si becomes amorphous in the first cycle.[51] For n-Si, a small lithiation peak at $\sim$0.25 V and the related delithiation peak at $\sim$0.27 was seen in the first cycle, marked in Figure 4.7 b). The delithiation peak at $\sim$0.45 V was also different from the m-Si, as it had a broad character. From the second cycle, similar differential capacity peaks were seen for both Si powders. As the anodes contained 10 wt% graphite, a small peak was observed at $\sim$0.15 V, associated with the delithiation of graphite.[107] The lithiation peaks of graphite were not distinguishable as they were "overshadowed" by the larger Si-lithiation peaks.

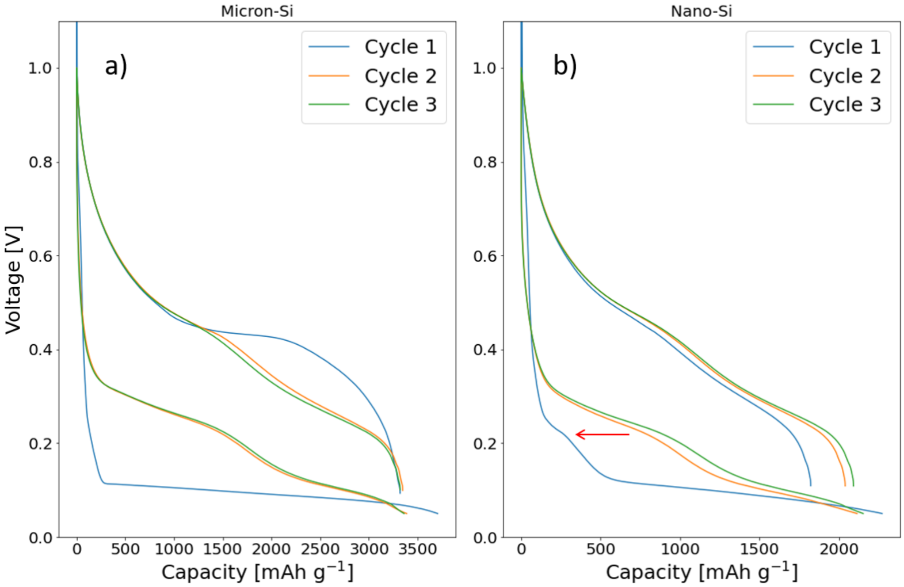

Figure 4.6: The first three voltage curves of a) m-Si and b) n-Si. The curves are derived from one representative cell.

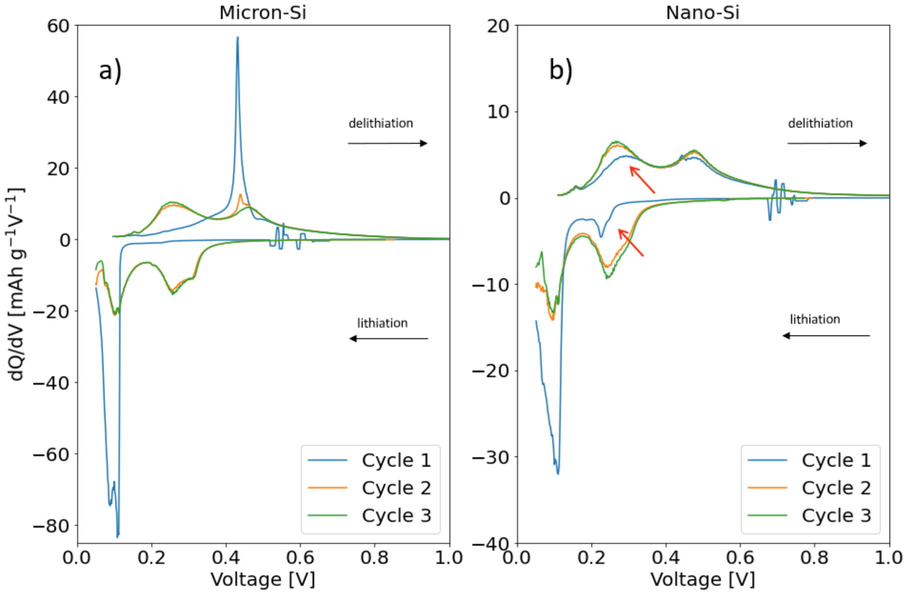

Figure 4.7: Differential capacities of a) m-Si and b) n-Si. The curves are derived from one representative cell.

4.1.3 Heat-treatment of powders

The pristine powders were heat-treated in a furnace (820°C, Ar, 2 h) to study the effects of the carbonization step, needed to make Si/C composites. The XRD diffractograms for the pristine and heat-treated powders are shown in Figure 4.8 and 4.9. The heat-treated Si had narrower peaks compared to the pristine Si. The (111)-peak position and FWHM were used to calculate the average crystallite size (τ), using the Scherrer-equation. Both the m- and n-Si had an increase in the calculated τ, after heat treatment. However, the change was more significant for n-Si as τ increased by 52%. The (111)-peak position, FWHM and τ are listed in Table 4.1.

XRD

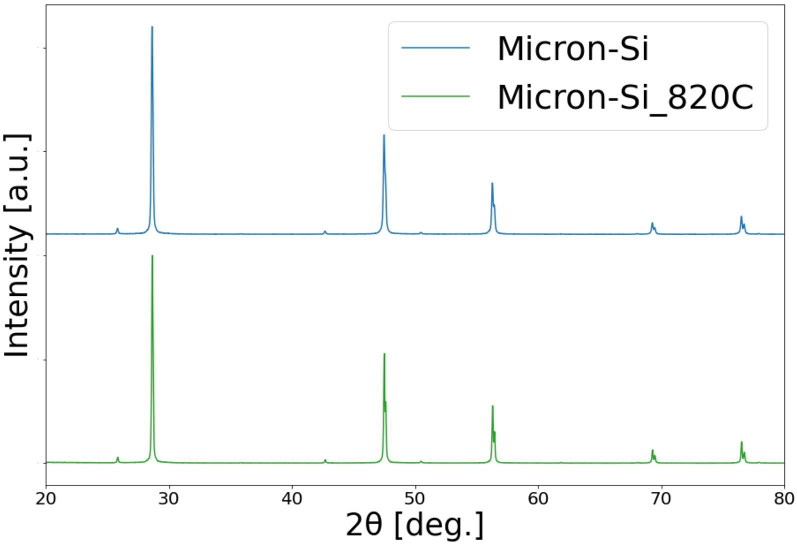

Figure 4.8: XRD-diffractograms of the pristine m-Si and heat-treated m-Si (820° under Ar-atmosphere).

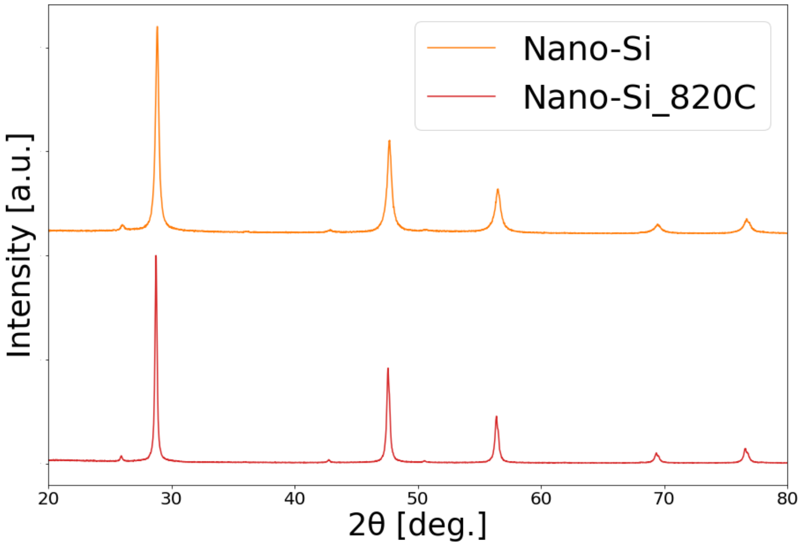

Figure 4.9: XRD-diffractograms of the as-received n-Si and n-Si heated to 820° under Ar-atmosphere

Table 4.1: The (111)-peak position, FWHM(111) and calculated τ for pristine and heat-treated Si.

	Micron-Si	**Micron-Si_820C**	**Nano-Si**	**Nano-Si_820C**
Peak$_{(111)}$ [°]	28.65	28.67	28.86	28.75
FWHM [°]	0.16	0.14	0.32	0.21
τ [nm]	53.5	61.2	26.8	40.8

Galvanostatic cycling

The pristine and heat-treated m-Si showed no significant change in differential capacity in the first cycles, as shown in Figure 4.10 a) and b). However, after heat-treatment of n-Si, the small lithiation peak at ~0.25 V, was reduced. A narrower delithiation peak at ~0.45 appeared after heat-treatment, as marked in Figure 4.11 b). The initial delithiation capacities for pristine and heat-treated Si showed no significant differences as seen in Figure 4.12.

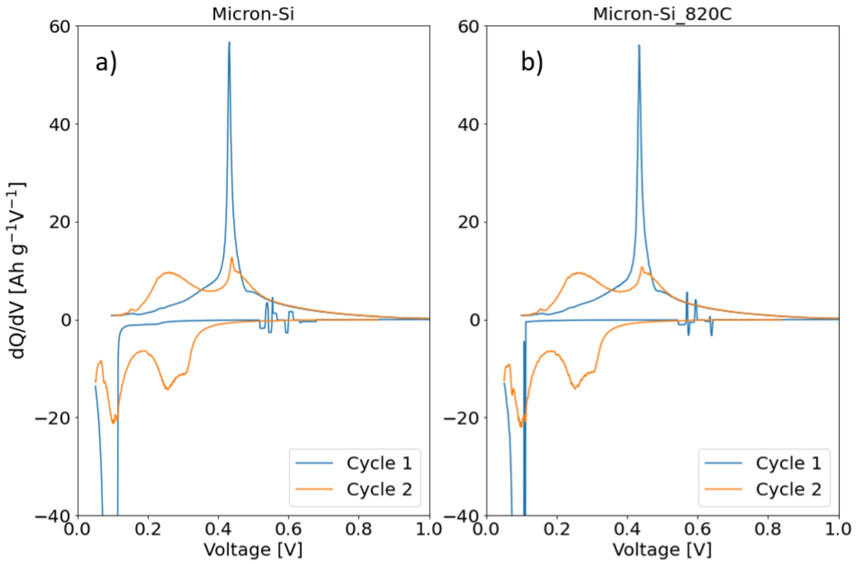

Figure 4.10: The differential capacities for the first two cycles of a) pristine m-Si and b) heat-treated m-Si. The curves are derived from one representative cell.

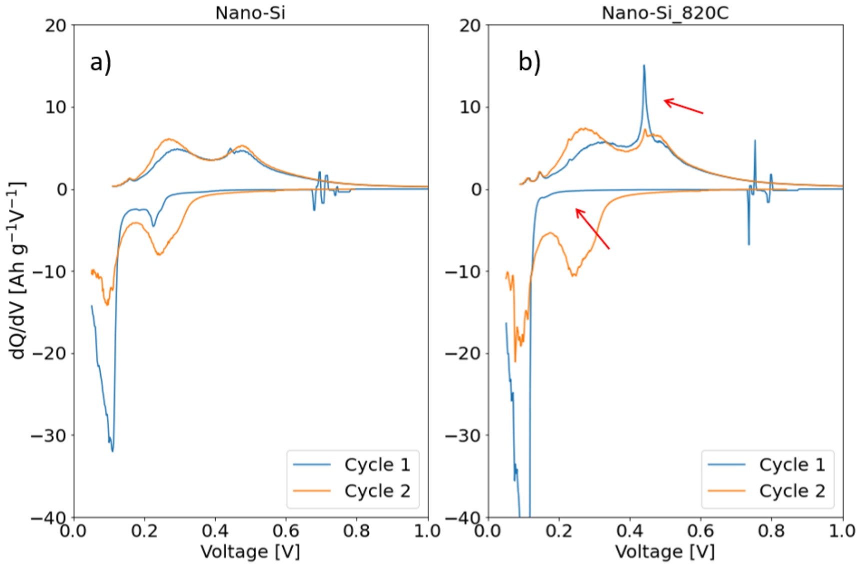

Figure 4.11: The differential capacities for the first two cycles of a) pristine n-Si and b) heat-treated n-Si. The curves are derived from one representative cell.

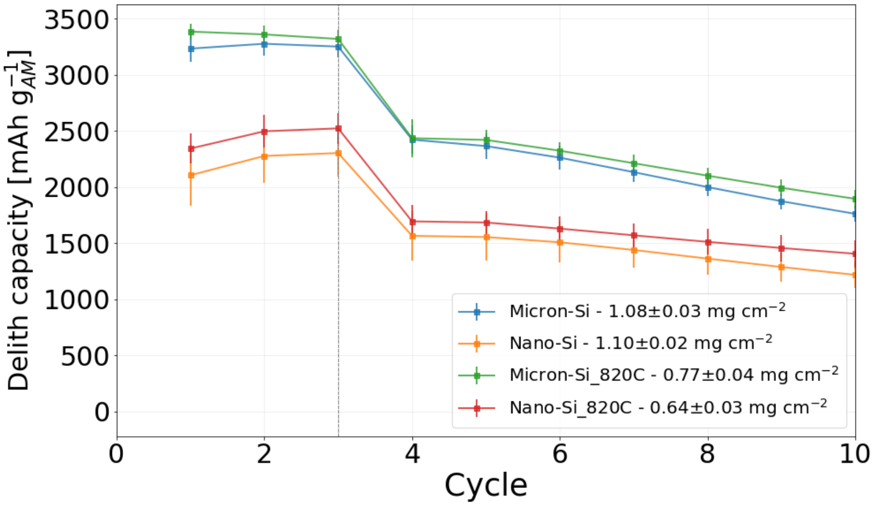

Figure 4.12: Delithiation capacities of pristine and heat-treated Si powders. The capacities for the pristine are an average of five cells each, and the heat-treated are an average of three cells each.

4.2 Si/C composites with RF-resin

4.2.1 Synthesis and reference

In an attempt to create a polymeric RF-layer on the surface of the m-Si particles, the zeta-potentials of the particles were modified by the surfactant molecule, CTAB, in water. The addition of CTAB in a 1:1 weight ratio to m-Si, changed the zeta-potential from negative to positive as seen in Figure 4.13.

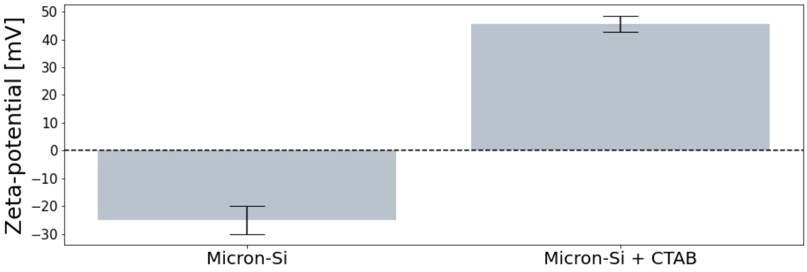

Figure 4.13: Zeta-potential measurements of m-Si/water suspensions with and without the addition of CTAB. CTAB was added in a 1:1 wt-ratio to Si.

To ensure that the polymerization reaction of RF-resin would take place under the reaction conditions used and to determine the capacity of the har pure RF-polymer particles were made with a high concentration of R and F. The synthesis yielded a pink powder after drying. SEM images revealed spherical particles with a narrow size distribution (diameter (d) = ∼1-2 µm), as seen in Figure 4.14 a). Based on the previous work on C-coating Si with RF-resin, it was expected to make Si/C composites with high hard carbon contents as the RF-resin amounts were increased.[4] Therefore, the capacity contribution of the hard carbon formed after carbonization would be non-negligible.

The polymer particles were carbonized to form hard carbon and a reference electrode with 60 wt% of the obtained hard carbon, 25 wt% CB, and 15 wt% binder, was cycled in half-cells, to determine its specific capacity. After three formation cycles at (0.16 A g^{-1}), the half-cells cycled at around 200 mAh g^{-1} for 500 cycles without significant capacity loss, as seen in Figure 4.14 b). The CE for the first cycle was ∼48.5%, however, the CE stabilized at >99.5% after five cycles. The differential capacity showed broad peaks between 1 and 0.75 V, and a large narrow peak at ∼2 V, for the first cycle. These peaks were not present in the subsequent cycles. The initial CEs and the differential capacity plot can be seen in Figure 4.14 c) and d).

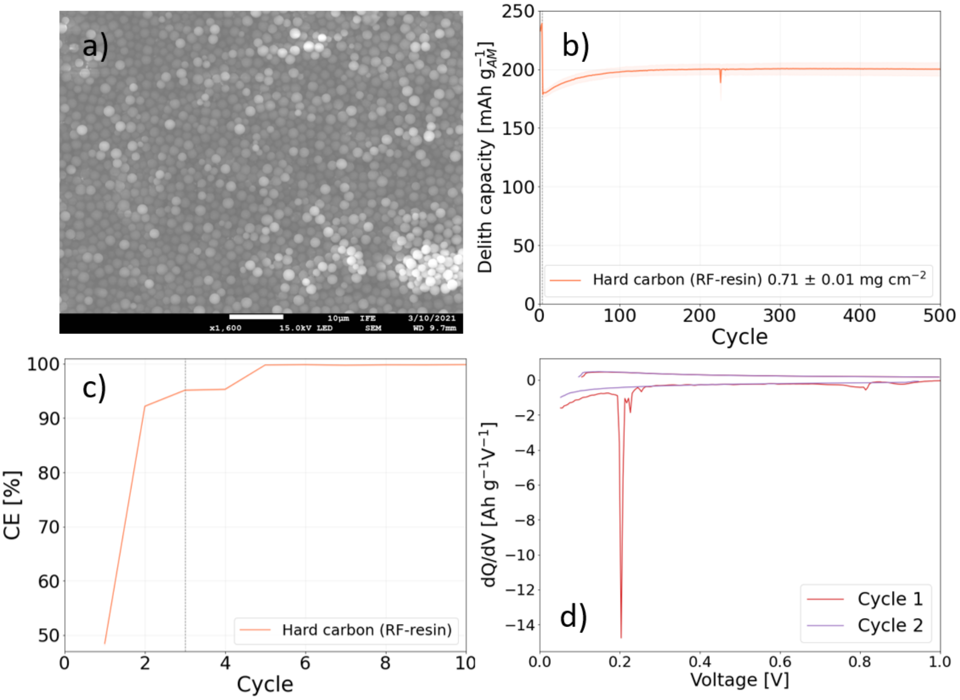

Figure 4.14: a) SEM-image of the polymer particles in sample RF-resin before carbonization, b) galvanostatic cycling of hard carbon (RF-resin) with three cycles at 0.16 A g^{-1} followed by 1.6 A g^{-1} (the average of three cells), c) coloumbic efficiencies for the first ten cycles, and d) differential capacities for the first two cycles.

Coatings of m-Si with an increasing amount of R and F were done according to Table 3.1. The pH of the reaction mixture was measured before and after the addition of ammonia and was ∼6 and ∼8, respectively, for all samples. All mixtures were left to age overnight with no stirring. The reaction mixtures for the RF-resin, m-Si@RF_60, and m-Si@RF_80 after the aging are shown in Figure 4.15. The reaction mixtures of m-Si@RF_0 and m-Si@RF_40 were visually similar to m-Si@RF_60. The RF-resin made a pink, milky suspension with a pink sediment. This was also seen in the supernate over the sediment for sample m-Si@RF_80, as shown in Figure 4.15 c). In samples m-Si@RF_0, m-Si@RF_40, and m-Si@RF_60, the supernate over the sediment was still brown. After centrifugation and washing, the sediments of the RF-resin, m-Si@RF_60, and m-Si@RF_80 were collected and shown in Figure 4.16. The m-Si@RF_0 and m-Si@RF_40 yielded brown sediments. For the m-Si@RF_60, a slight gradient in the color from dark brown to light brown was observed and marked with an arrow in Figure 4.16 b). In m-Si@RF_80, a layer of pink sediment settled on top of the brown sediment, as shown in Figure 4.16 c). No further effort in separating the two layers was made.

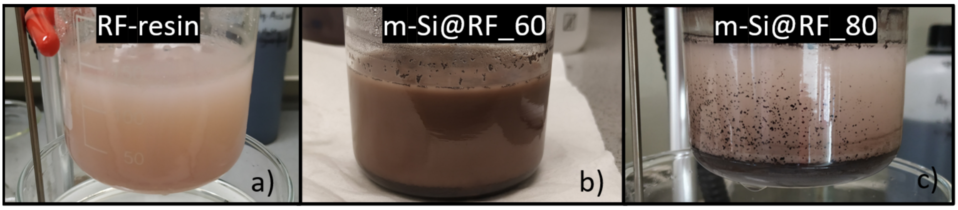

Figure 4.15: Samples a) RF-resin, b) m-Si@RF_60, and c) m-Si@RF_80 after aging overnight.

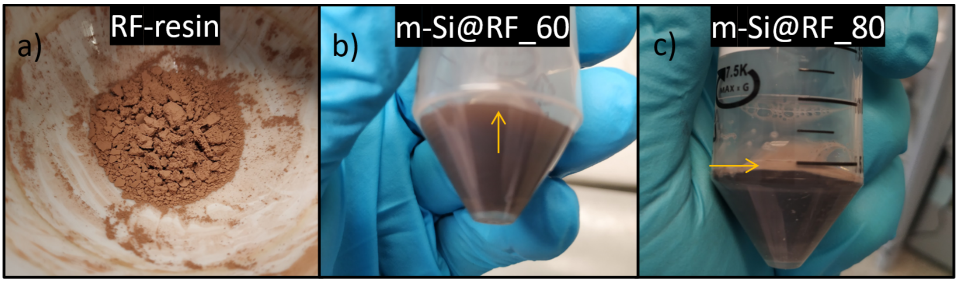

Figure 4.16: The sediments obtained after washing for a) RF-resin, b) m-Si@RF_60, and c) m-Si@RF_80.

4.2.2 Material characterization

C content

After carbonization and ∼5 min gentle hand-grinding, the C content was determined in the samples that had RF-resin added to the synthesis. The C contents are shown in Figure 4.17. The wt% of carbon almost doubled from sample m-Si@RF_40 to m-Si@RF_60, which was expected as the R and F amount was increased with a factor of ∼2.2, in the synthesis. However, the carbon content of m-Si@RF_80 only increased 4.1 wt.% as the amounts of R and F were increased by a factor of ∼2.7. The C content of the carbonized RF-resin sample was measured to 96.6 wt%. The powders were not degassed or dried before analysis.

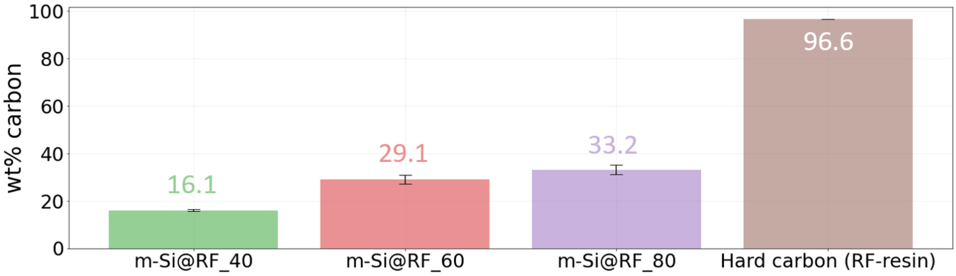

Figure 4.17: C content for samples: m-Si@RF_40, m-Si@RF_60, m-Si@RF_80 and RF-resin.

Specific surface area (SSA)

Figure 4.18 shows the SSAs determined from BET analyses. The adsorption/desorption isotherms are shown in Figure A.1. The Micron-Si, m-Si@RF_0, m-Si@RF_40 and m-Si@RF_60 had isotherms characteristic of a non- or macro-porous material. A decrease in the SSAs of m-Si@RF_0, m-Si@RF_40, and m-Si@RF_60 were seen compared to the Micron-Si. The m-Si@RF_80 had an extreme increase in SSA with an isotherm characteristic of a microporous material.

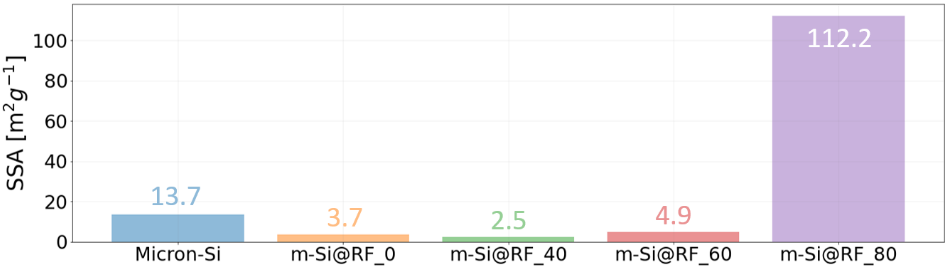

Figure 4.18: Specific surface areas of Micron-Si, m-Si@RF_0, m-Si@RF_40, m-Si@RF_60, and m-Si@RF_80, from BET-analysis.

SEM

SEM was used to study the morphology of the Si/C composites after carbonization. Sample m-Si@RF_40, in Figure 4.19 a1), showed a high number of distorted spherical particles in the size range of d = ∼0.5-1 µm, together with larger micron-sized particles with irregular shapes. The micron-sized particles were similar to the pristine m-Si seen in Figure 4.1 a). However, the micron-sized particles of m-Si@RF_40 had rounded edges. Figure 4.19 a2) shows two spherical particles with d = ∼0.5 µm, present in the same sample. Sample m-Si@RF_60 showed a similar particle mixture as described for m-Si@RF_40, and with the same rounding of the edges for the large particles, as seen in Figure 4.19 b1). Figure4.19 b2) shows the smaller spherical particles with d = ∼0.5 µm present in the same sample. Sample m-Si@RF_80 showed a powder with large mono-sized spherical particles with d = ∼2 µm, as seen in Figure 4.19 c1) and c2). The same rounding of the edges was seen for most larger particles, however, some particles with rougher edges were observed, as marked with an arrow in 4.19 c1). Figure 4.20 highlights the morphology change as RF-resin is added. The particles in m-Si@RF_0 still showed rough edges similar to the pristine m-Si, after going through the synthesis steps without any RF-resin, as seen in Figure 4.20 a).

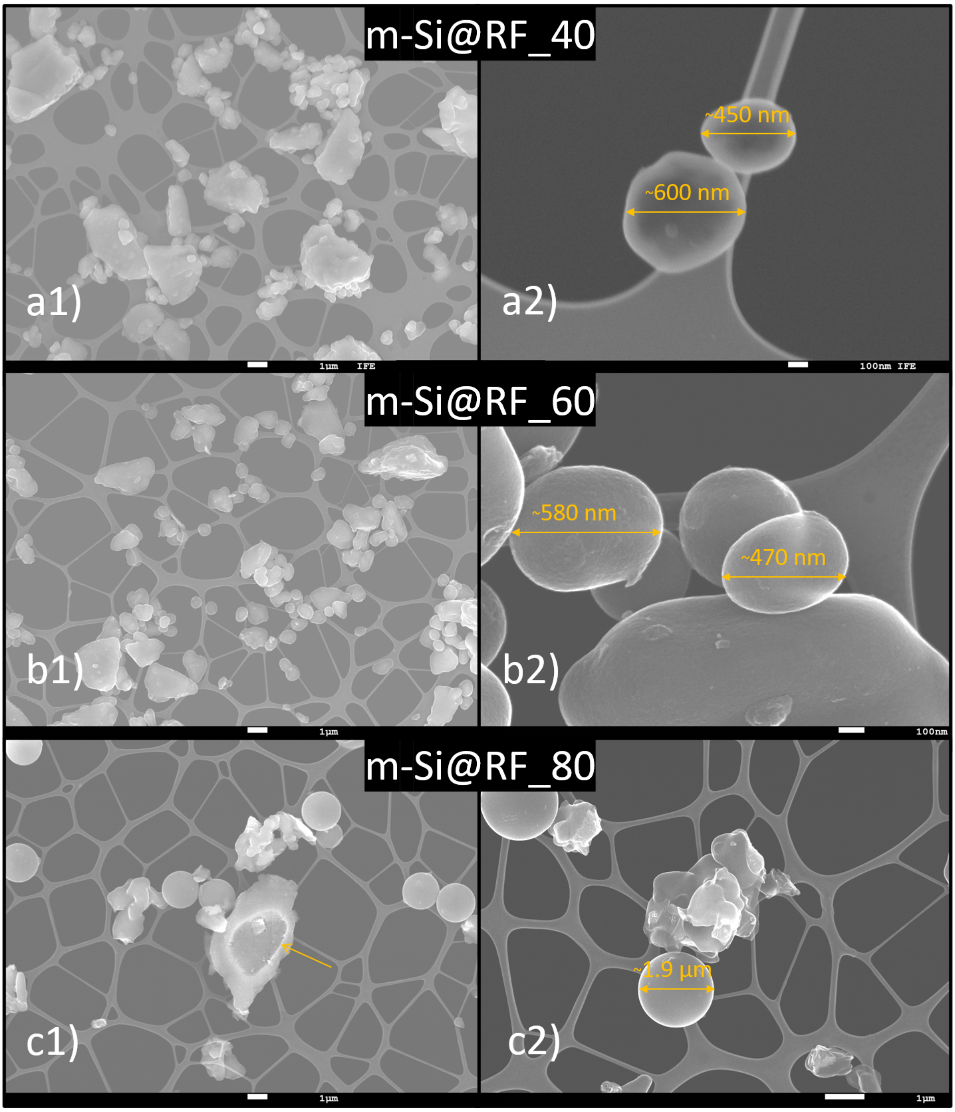
m-Si@RF_40
~450 nm
~600 nm
a1)
a2)
1µm IFE
100nm IFE
m-Si@RF_60
~580 nm
~470 nm
b1)
b2)
1µm
100nm
m-Si@RF_80
~1.9 µm
c1)
c2)
1µm
1µm

Figure 4.19: SEM-images of a1), a2) m-Si@RF_40, b1), b2) m-Si@RF_60, and c1), c2) m-Si@RF_80, after carbonization.

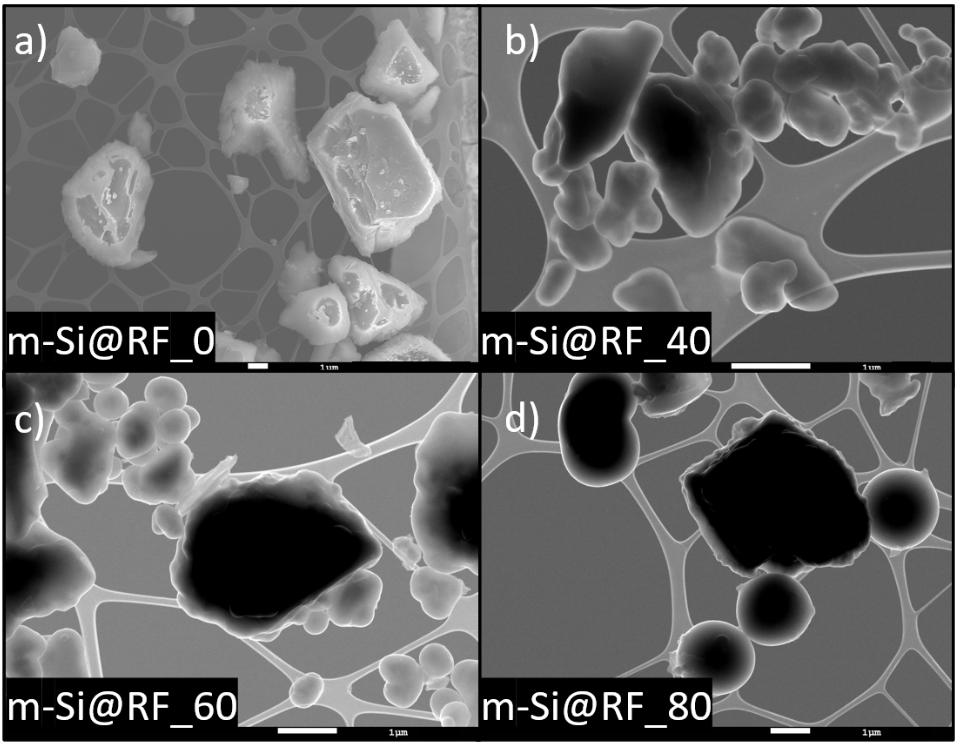

Figure 4.20: SEM-images of a) m-Si@RF_0, b) m-Si@RF_40, c) m-Si@RF_60, and d) m-Si@RF_80, after carbonization.

EDS

In an attempt to verify if the m-Si particles were surface-coated with a C shell, EDS-analysis was used to construct elemental maps of Si, C, and O. Figure 4.21 shows the elemental maps and SEM-images for the samples. The samples were prepared on a C laced Cu-grid that contributed to the C counts. This is shown in the C maps for m-Si and m-Si@RF_0. The C rich surfactant molecule CTAB can be assumed to be washed out before carbonization, and no evident C rich surface due to CTAB was seen for m-Si@RF_0. However, for the three samples containing RF-resin, the C counts clearly showed the presence of C at the Si-particles. EDS-analysis was also used in order to determine if the large spheres in m-Si@RF_80 contained Si-cores, as seen in Figure 4.22. Based on the highly concentrated C counts and low Si-count, the spheres were assumed to contain mostly C without a Si-core. STEM mode on the SEM was used in an attempt to confirm surface coating, however, this was not successful due to the limited acceleration voltage of 30 kV.

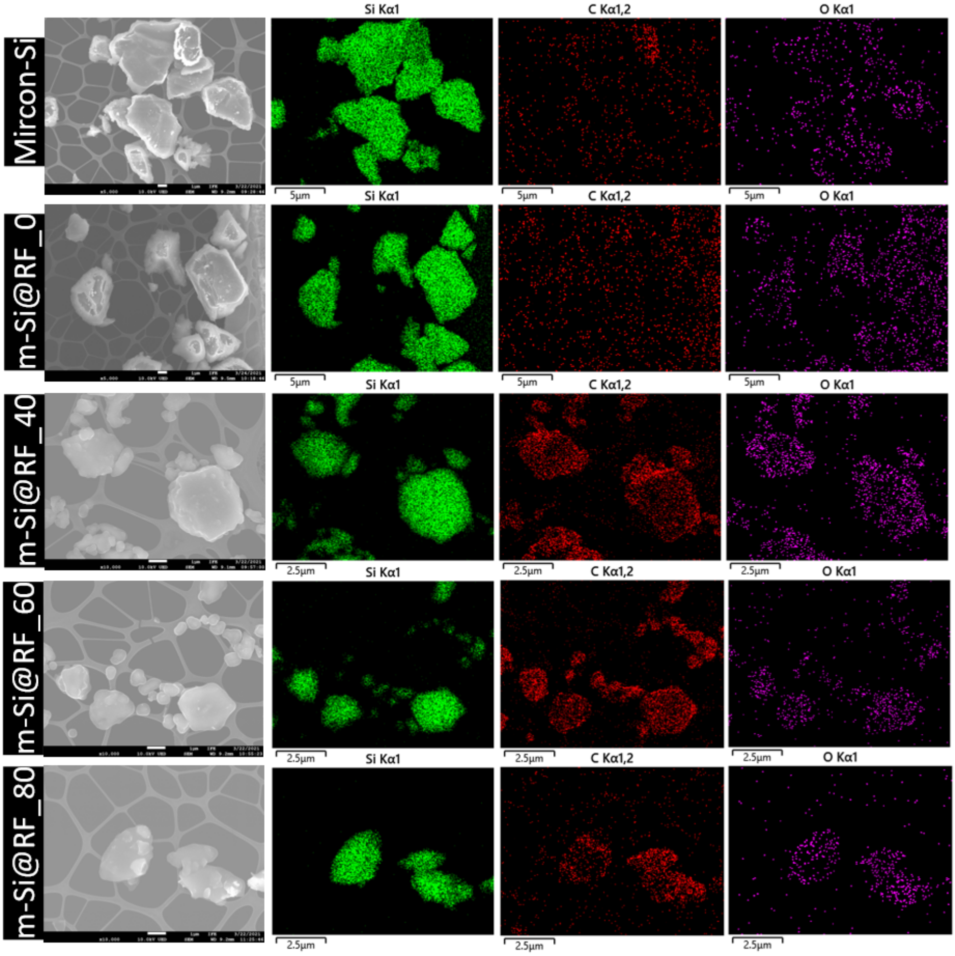
Si Kα1
C Kα1,2
O Kα1
Mircon-Si
m-Si@RF_0
m-Si@RF_40
m-Si@RF_60
m-Si@RF_80
5μm
2.5μm

Figure 4.21: EDS-analysis maps of Si, C and O for pristine Micron-Si, m-Si@RF_0, m-Si@RF_40, m-Si@RF_60, and m-Si@RF_80 and related SEM-images. Counts: Green = Si, red = C and purple = O.

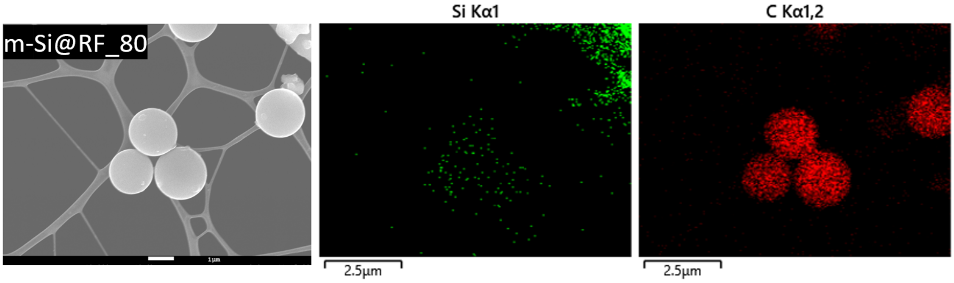

Figure 4.22: EDS-analysis maps and SEM-image of spheres observed in m-Si@RF_80.

TEM

TEM was used in different operating modes and with supporting EDS-analysis to characterize the treated samples m-Si@RF_0, m-Si@RF_40, m-Si@RF_60, and m-Si@RF_80. High resolution bright field TEM (HR BF TEM) was used to study the SiO_x surface layer of m-Si@RF_0 and is shown in Figure 4.23 a1) and a2). No carbon was detected in this sample. The SiO_x thickness varied in the range of 1–7 nm, but was typically observed in the range of 2–4 nm. The images in Figure 4.23 a1) and a2) clearly show an amorphous layer on the crystalline Si. High angle annular dark field STEM mode (HAADF STEM) was used to determine if m-Si@RF_40 was C-coated. A dark contrast C layer, surrounding the brighter m-Si particles, was clearly observed, as seen in Figure 4.23 b1) and b2). A complete and homogeneous C-coating with thickness typically in the range of 50–70 nm was observed. No pure C particles were observed.

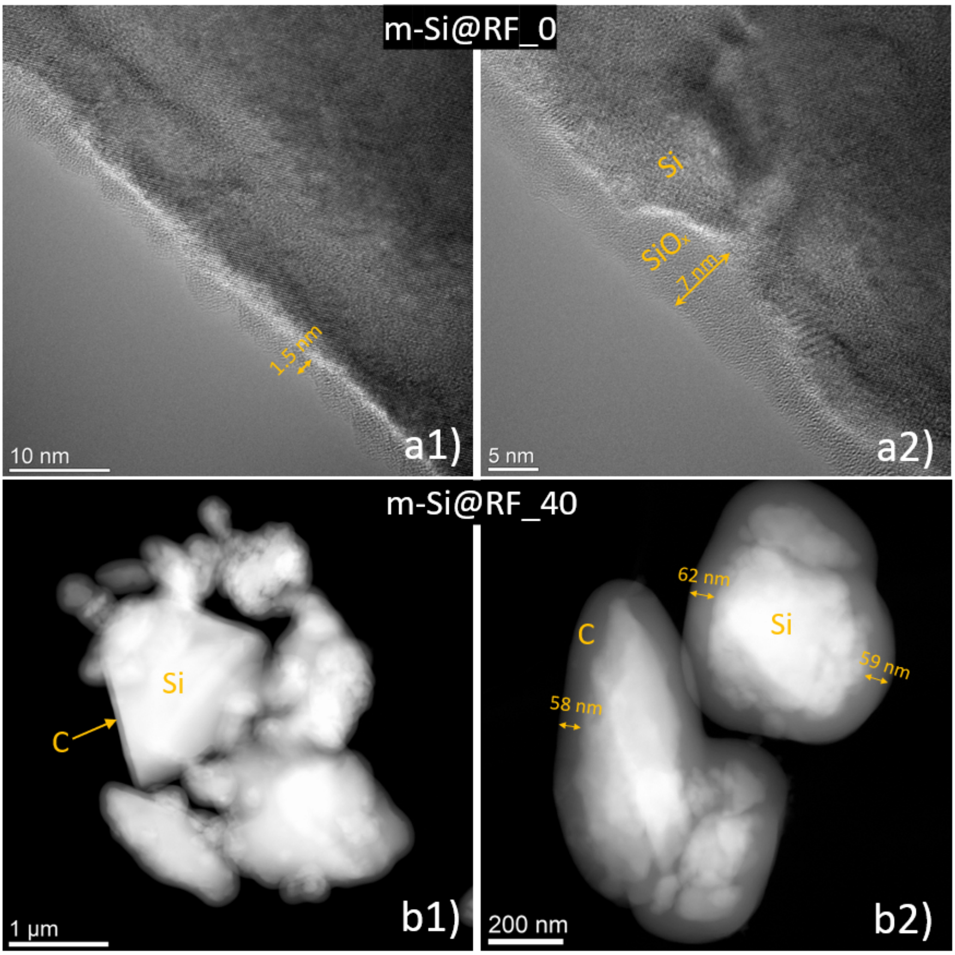
m-Si@RF_0
1.5 nm
10 nm
a1)
Si
SiOx
2 nm
5 nm
a2)
m-Si@RF_40
Si
C
1 µm
b1)
62 nm
C
Si
59 nm
58 nm
200 nm
b2)

Figure 4.23: a1), a2) HR-BF TEM images of m-Si@RF_40 and b1), b2) HAADF STEM images of m-Si@RF_40.

The HAADF STEM images of m-Si@RF_60 and and m-Si@RF_80 are shown in Figure 4.24. In m-Si@RF_60, all of the C was found as a thick and homogeneous coating around the Si particles. No pure carbon spheres were observed. The thickness of the C-coating was typically in the range 100–150 nm. In m-Si@RF_80, most of the C was found as amorphous spheres confirming what was assumed from EDS. However, a few of these spheres had small Si particles embedded in the middle. As pointed out with an arrow in Figure 4.24 b1).

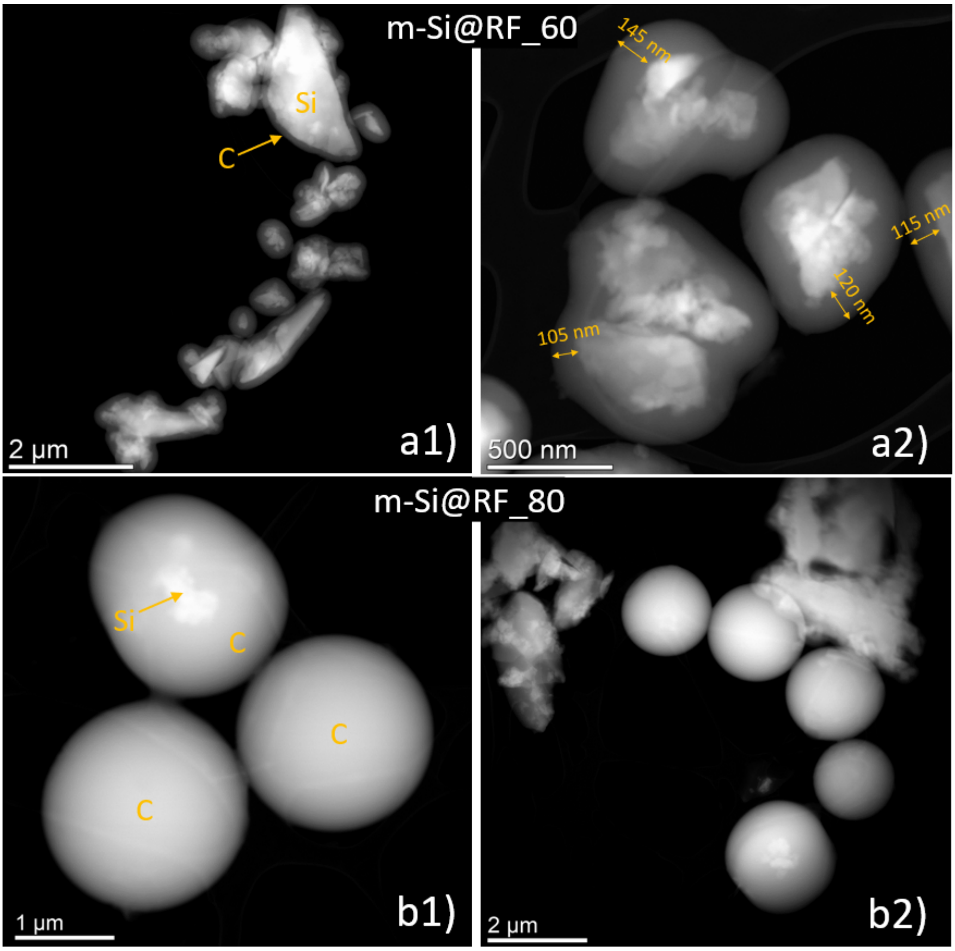
m-Si@RF_60
Si
C
2 µm
a1)
145 nm
115 nm
120 nm
105 nm
500 nm
a2)
m-Si@RF_80
Si
C
C
C
1 µm
b1)
2 µm
b2)

Figure 4.24: HAADF STEM images of a1), a2) m-Si@RF_60, and b1), b2) m-Si@RF_80.

Only a minority of the C in m-Si@RF_80 existed as a regular coating around the Si. The particles coated had highly inhomogeneous thicknesses (nano to micron range). An example of a thin coating of SiO_x and C is shown in Figure 4.25, for m-Si@RF_80. The amorphous SiO_x was observed to be around 3-4 nm, while the carbon, was only 2-3 nm. The thin coating was also visualized by EDS-mapping and compared to m-Si@RF_60, as shown in Figure 4.26.

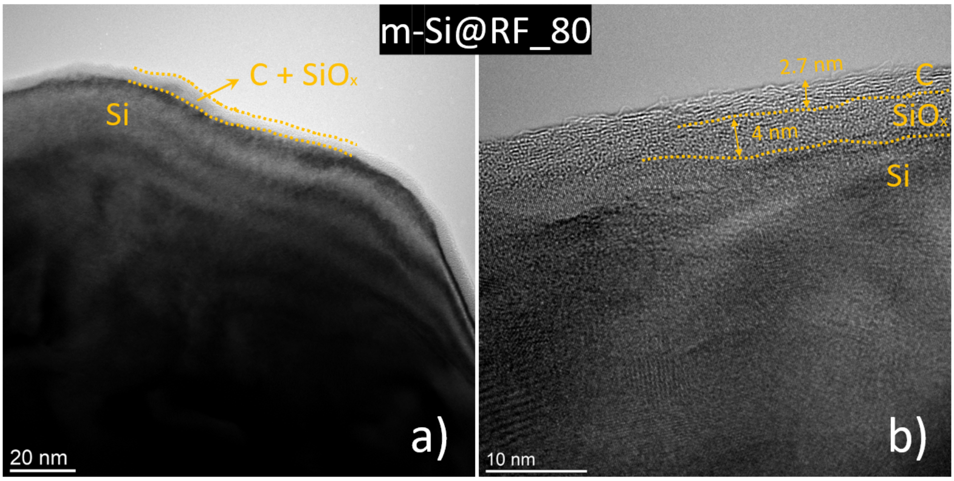
m-Si@RF_80
C + SiO$_x$
Si
a)
20 nm
2.7 nm
C
SiO$_x$
4 nm
Si
b)
10 nm

Figure 4.25: a), b) HR BF TEM images of m-Si@RF_80.

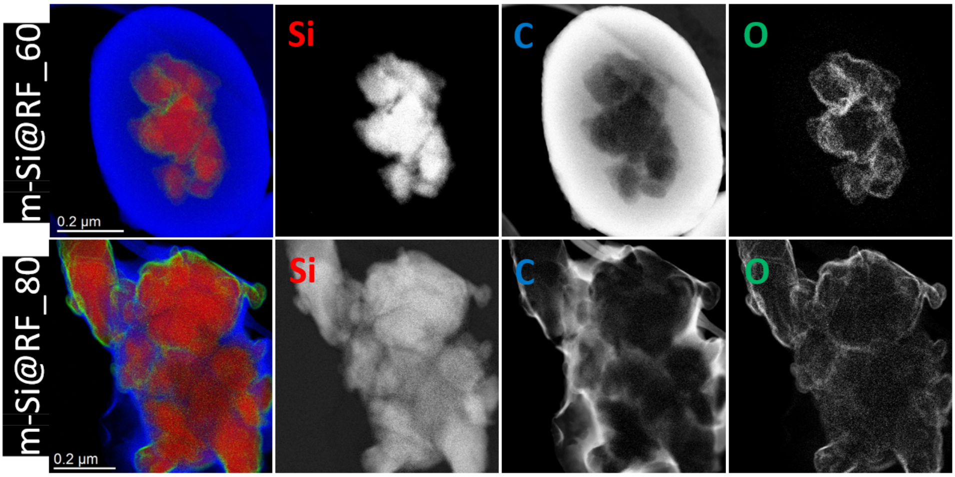
m-Si@RF_60
0.2 µm
Si
C
O
m-Si@RF_80
0.2 µm
Si
C
O

Figure 4.26: EDS-mapping of m-Si@RF_60 and m-Si@RF_80. Red = Si, blue = C green = O.

4.2.3 Electrochemical testing

Galvanostatic cycling

Electrodes were long-term galvanostatically cycled in half-cells as described in section 3.4, and the delithiation capacities as a function of cycle index are shown in Figure 4.27. The initial capacities of Micron-Si and m-Si@RF_0 were similar at 2848±90 and 2885±92, respectively. The composites m-Si@RF_40, m-Si@RF_60, and m-Si@RF_80 had lower initial capacities compared to Micron-Si, namely ∼71%, ∼63%, and ∼63% respectively. Significant capacity losses during the formation cycles were seen for m-Si@RF_0, m-Si@RF_40, and m-Si@RF_60. A drop in capacity as the current was increased, was seen for all samples. After around 25-30 cycles the capacities stabilized or even increased. All samples restored some of the capacity loss, however, this was most prominent for m-Si@RF_0 and m-Si@RF_80, which restored ∼190 and ∼170 mAh g^{-1}, respectively, after their minimums at around 25-30 cycles. This is in line with previous work reported and known as a *pseudo* "self-healing" mechanism of Si.[65]

The composites m-Si@RF_40 and m-Si@RF_60 showed low capacities with high stability. Some significant deviation between cells, with the same electrode material, was seen after around 100 cycles. Micron-Si showed the highest capacity and by far the highest total charges for the first 100 cycles. However, rapid capacity losses at a lower cycle index were seen for Micron-Si, compared to m-Si@RF_0 and m-Si@RF_80.

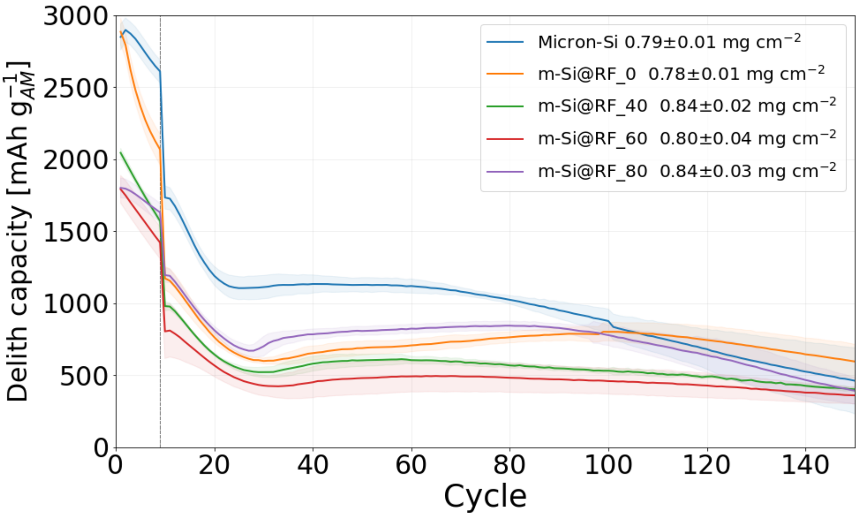

Figure 4.27: The galvanostatic cycling of m-Si, m-Si@RF_0, m-Si@RF_40, m-Si@RF_60 and m-Si@RF_80 (half-cells). The cycling included nine formation cycles 0.16 A g^{-1} followed by 1.6 A g^{-1}, marked by a bold grey vertical line.

By normalizing the delithiation capacity to the initial delithiation capacity, the average capacity retentions were determined, as shown in Figure 4.28. This illustrated the large differences in the cycling stability for the three composite materials and between Micron-Si and m-Si@RF_0. The capacity retention in the 9th and 100th cycle are listed in Table 4.2.

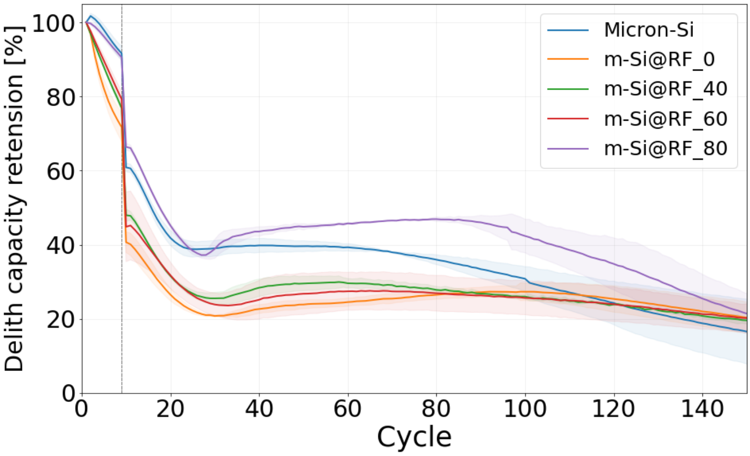

Figure 4.28: Capacity retention of m-Si, m-Si@RF_0, m-Si@RF_40, m-Si@RF_60, and m-Si@RF_80, normalized to the initial delithiation capacity.

The average internal resistance (IR) measurements of the cells with Micron-Si and m-Si@RF_80 are shown in Figure 4.29. Micron-Si and m-Si@RF_80 had a change from decreasing to increasing IR at around cycle 95 and 130, respectively, correlating with the rapid capacity losses.

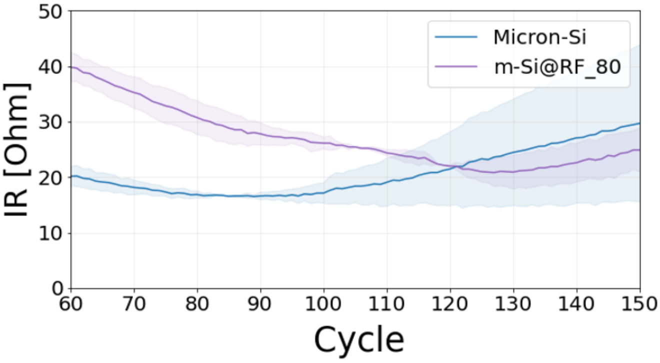

Figure 4.29: Internal resistance measurements of Micron-Si and m-Si@RF_80.

The CEs reported in Figure 4.30 and Table 4.2 are from the rate-testing which was performed on another battery tester. Similar loadings were used and the current was the same for the first cycle. The composites showed lower initial CEs compared to the Si samples.

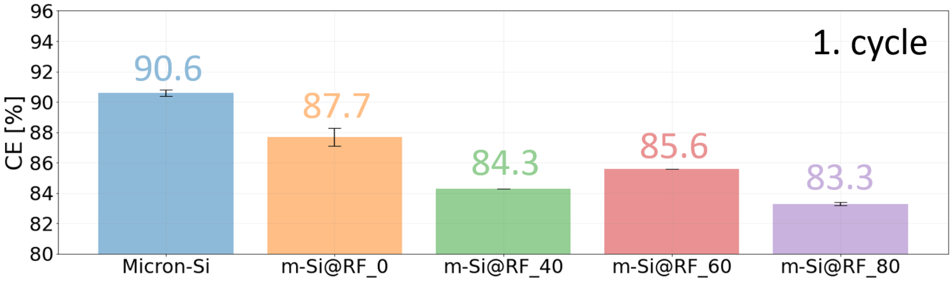

Figure 4.30: Initial coulombic efficiencies of m-Si, m-Si@RF_0, m-Si@RF_40, m-Si@RF_60, and m-Si@RF_80, at 0.16 A g^{-1}.

Table 4.2: Initial delithiation capacity, initial CE and capacity retentions of the 9. and 100. cycle for m-Si, m-Si@RF_0, m-Si@RF_40, m-Si@RF_60 and m-Si@RF_80.

Sample	**Initial delith-capacity [mAh g^{-1}]**	**Initial CE [%]**	**Cap retention (9. cycle) [%]**	**Cap retention (100. cycle) [%]**
Micron-Si	2848±90	90.6±0.2	92±1	31±3
m-Si@RF_0	2885±92	87.7±0.6	72±3	27±2
m-Si@RF_40	2045±30	84.3	77±2	26±1
m-Si@RF_60	1792±95	85.6	79±9	26±5
m-Si@RF_80	1802±69	83.3±0.1	91±1	42±5

In order to clarify if the cycling behavior of the Si/C composites were independent of Si-content, cells with the same Si-loading (∼0.7 mg cm^{-1}) were also long-term cycled. That implied increasing total loading with increasing C content. The cycling results are shown in Figure 4.31, and showed nearly identical cycling behavior over the first 60 cycles. However, after 60 cycles, a rapid capacity loss was seen for m-Si@RF_80. The capacity retention was reduced from 42±5% to 24±13 (100th cycle), as listed in Table 4.3. No significant difference was seen for the m-Si@RF_40 and m-Si@RF_60 with increased loading.

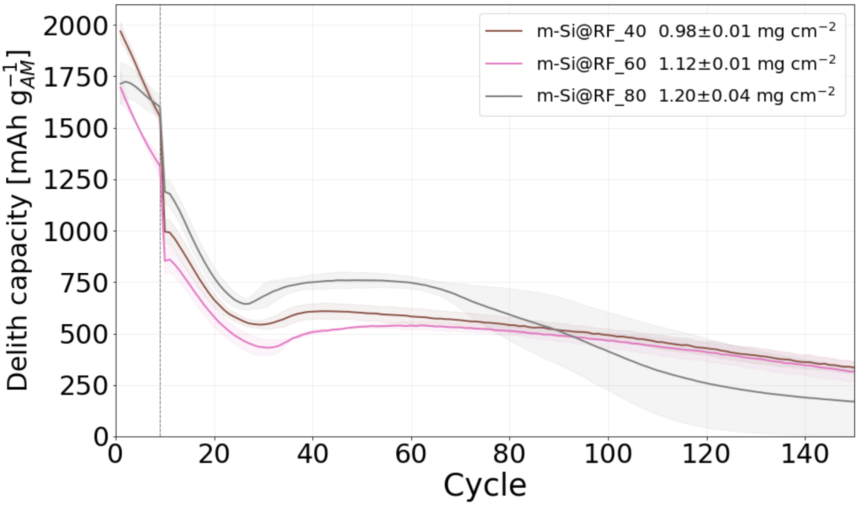

Figure 4.31: The galvanostatic cycling of m-Si, m-Si@RF_0, m-Si@RF_40, m-Si@RF_60 and m-Si@RF_80 (half-cells), with equal Si-loading. The cycling included nine formation cycles 0.16 A g^{-1} followed by 1.6 A g^{-1}, marked by a bold grey vertical line.

Table 4.3: Initial delithiation capacity and capacity retentions of the 9. and 100. cycle for m-Si@RF_40, m-Si@RF_60 and m-Si@RF_80, with equal Si-content.

Sample	**Initial delith capacity [mAh g^{-1}]**	**Cap retention (9. cycle) [%]**	**Cap retention (100. cycle) [%]**
m-Si@RF_40	1968±47	79±0	25±1
m-Si@RF_60	1695±82	77±7	27±1
m-Si@RF_80	1713±101	94±3	24±13

Rate-testing

Half-cells were tested at increasing current rates starting with 13 formation cycles at 0.16 A g^{-1} and ending with a constant current of 0.62 A g^{-1}. One cell each of m-Si@RF_40 and m-Si@RF_60 failed to cycle correctly and are therefore not included in Figure 4.32. The m-Si@RF_0, m-Si@RF_40, and m-Si@RF_60 experience a rapid capacity loss during the formation cycles, as was seen in the long-term cycling as well. In order to compare the effects of the increasing current rates, the capacity was normalized to the capacity of the last formation cycle, as seen in Figure 4.33. The Micron-Si and m-Si@RF_80 showed the best rate-performance, but all samples retained a capacity close to the previous current of the same rate (0.62 A g^{-1}). After retention of capacity, the Micron-Si suffered a rapid capacity loss at around 60 cycles, while m-Si@RF_0 and m-Si@RF_80 cycled relatively stably. No significant differences were seen between m-Si@RF_40 and m-Si@RF_60.

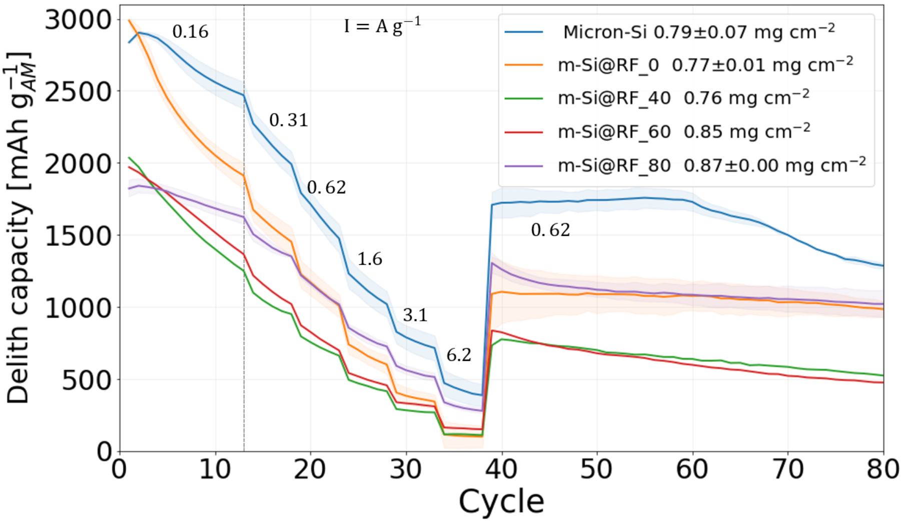

Figure 4.32: Rate-testing with 13 cycles with I = 0.16 A g^{-1}, followed by 5 cycles at 0.31 A g^{-1}, 0.62 A g^{-1}, 1.6 A g^{-1}, 3.1 A g^{-1}, 6.2 A g^{-1} (2C). Lastly, a constant current of 0.62 A g^{-1} was applied.

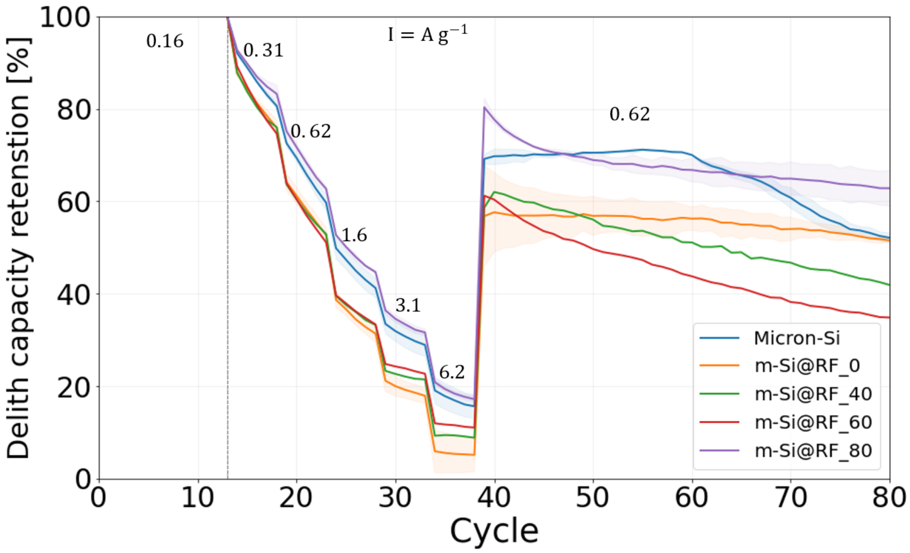

Figure 4.33: Capacity retention of rate-testing normalized with respect to the delithiation capacity of the 13. cycle.

The cells experienced shifts in the lithiation and delithiation peaks, in the differential capacity plots, as the current was increased. This is illustrated with the differential capacity of m-Si@RF_60, in Figure 4.34. The peaks associated with the lithiation of Si shifted to lower potentials, while the delithiation peaks shifted to higher potentials. As the current reached 3.1 A g^{-1}, the lithiation peak at ∼0.1 V and delithiation peak at ∼0.25-0.30 disappeared. However, as the rate was decreased to 0.62 A g^{-1}, at cycle 40, the peaks reappeared.

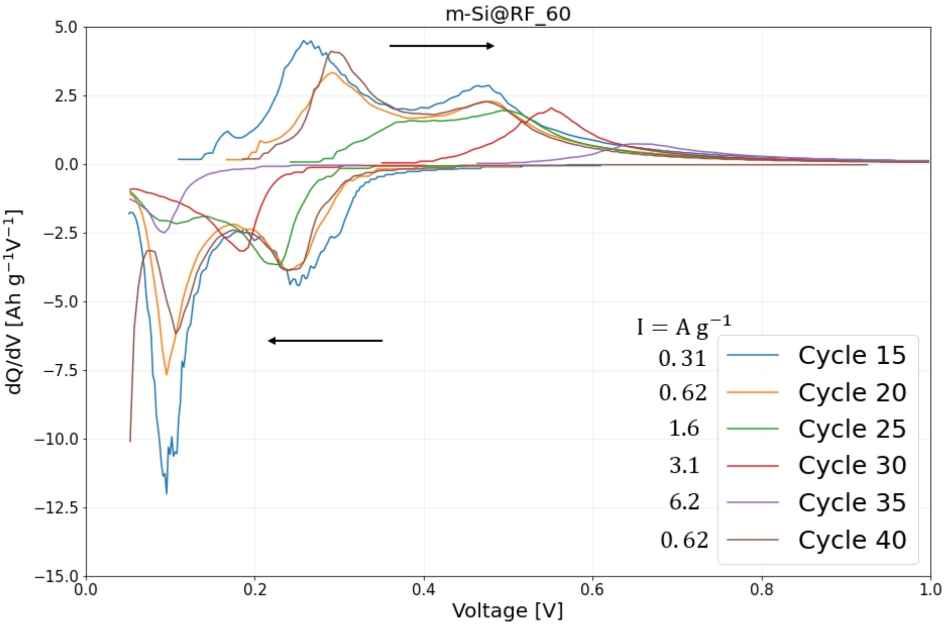

Figure 4.34: Differential capacity of m-Si@RF_60-cell during rate-testing. Each cycle represents a different current rate. The curves are derived from one representative cell.

Full-cells

The long-term galvanostatic cycling of Micron-Si, m-Si@RF_0, and m-Si@RF_80 in full-cells are shown in Figure 4.35. The anode loadings were 0.46±0.01, 0.46±0.03 and 0.72±0.00 mg cm^{-2}, respectively. A rapid loss in capacity was seen in the first 50 cycles for m-Si@RF_0. Micron-Si and m-Si@RF0 had similar cycling behavior with close to linear capacity loss after the formation cycles, however, the capacity losses in the formation cycles were larger for the latter. The CEs for the first cycle are shown in Figure 4.36 and shows a lower initial CE for m-Si@RF0 compared to Micron-Si and m-Si@RF_0. The trend in initial CEs is in line with the results from the half-cell testing.

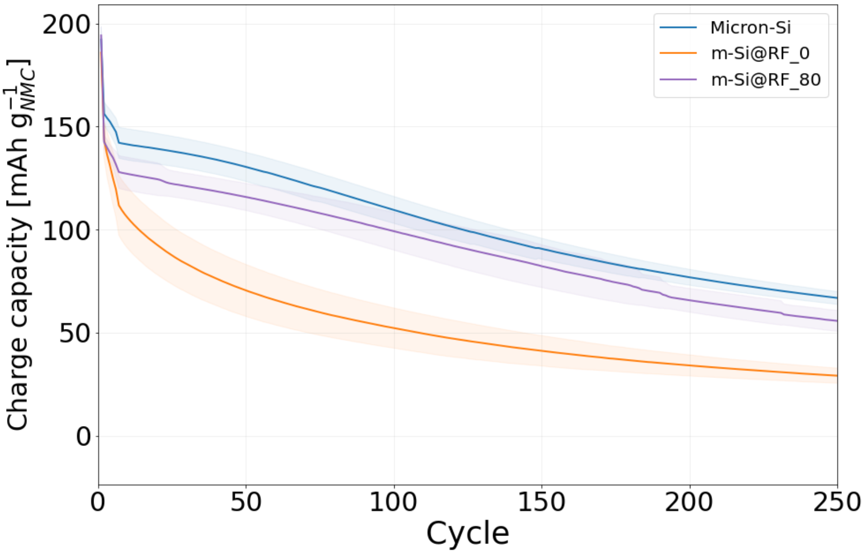

Figure 4.35: The galvanostatic cycling of NMC(111)/Si or Si/C-full cells. One cycle of 7.25 mA g^{-1}, two cycles at 14.5 mA g^{-1}, two at 29 mA g^{-1} and continuous cycling at 72.5 mA g^{-1}, between 3 and 4.3 V.

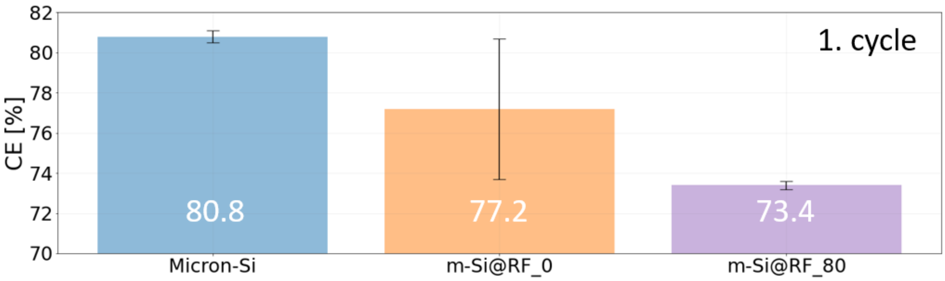

Figure 4.36: Initial coulombic efficiencies for full-cells with Micron-Si, m-Si@RF_0 and m-Si@RF_80.

4.3 Si/C composites with glucose

4.3.1 Reference

Glucose was carbonized and ball-milled as described in section 3.1.4, and the C content was measured to 97.8±0.2 wt%. Half-cells with the hard carbon from glucose were galvanostatically cycled with a targeted anode composition of 60 wt.% hard carbon, 25 wt.% CB and 15 wt.% PAA binder. After the formation cycles, a stable capacity of ∼160 mAh g_{AM}^{-1} was achieved over 300 cycles, as seen in Figure 4.37 a). The initial CE was 40.2±0.3 %, however, high CEs were achieved after the formation cycles, as seen in Figure 4.37 b).

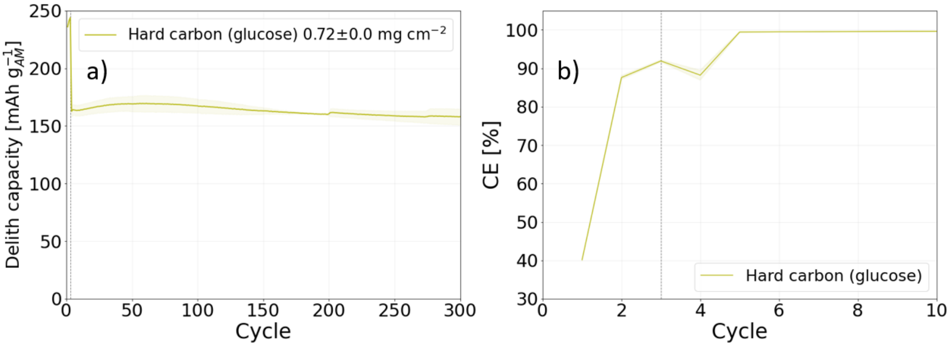

Figure 4.37: a) Delithiation capacity of half-cells with hard carbon (glucose) and b) Initial coulombic efficiencies for the first ten cycles. Three cycles at 0.16 A g^{-1} followed by 1.6 A g^{-1}. The average of three cells.

4.3.2 m-Si/C composites

Synthesis and C content

The m-Si/C composites were made according to the procedure described in section 3.1.3. After carbonization, the m-Si@G_20 and m-Si@G_40 remained as powders, while m-Si@G_60 became one solid and highly porous structure. After ball-milling, the C contents were measured and are shown in Figure 4.38. An increase in C content with increasing glucose was seen, as expected.

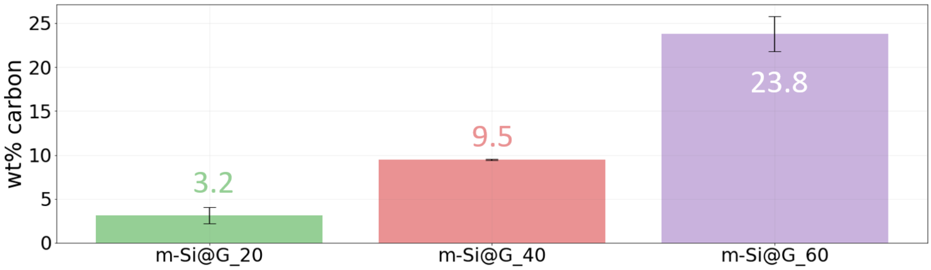

Figure 4.38: C content m-Si@G_20, m-Si@G_40, and m-Si@RF_60 after carbonization.

SEM

SEM-images of m-Si@G_0 showed a powder with an increased number of nanosized particles, compared to pristine m-Si. These nanoparticles were agglomerated together as seen in Figure 4.39 a). A rounding of the particle edges and a high number of sub-micron particles was seen for sample m-Si@G_20 in Figure 4.39 b). Some particles with rounded edges were also seen in m-Si@G_40 and m-Si@G_60, however, a higher number of the micron-sized particles seemed to retain their original shape, compared to the m-Si@G_0 and m-Si@G_20, as seen in Figure 4.39 c) and d).

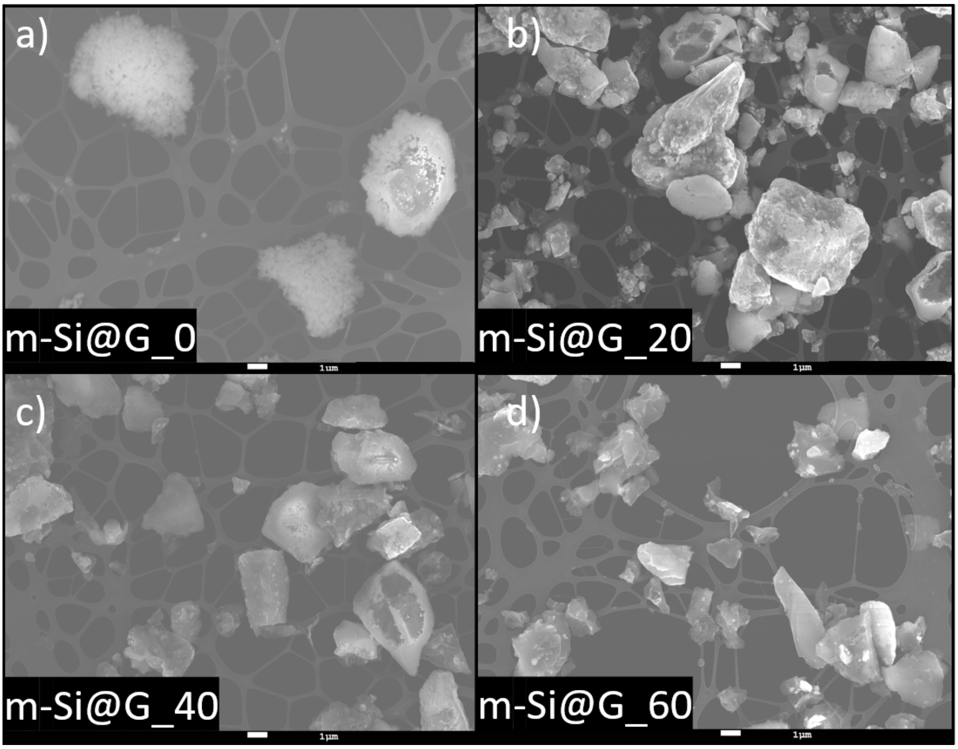

Figure 4.39: SEM-images of a) m-Si@G_0, b) m-Si@G_20, c) m-Si@G_40, and d) m-Si@G_60, after carbonization and ball-milling.

EDS

EDS-analysis maps were created for the samples, as seen in Figure 4.40. The Si/C composites m-Si@G_20, m-Si@G_40 and m-Si@G_60 showed a reasonable match between the SEM and elemental maps. However, some Si particles did not show any C counts in the same area. This was especially obvious in the C count map of sample m-Si@G_40 and m-Si@G_60. The m-Si@G_0 shows a higher number of counts from the C film background. There were also C counts from the particles, even though no C was added to this sample.

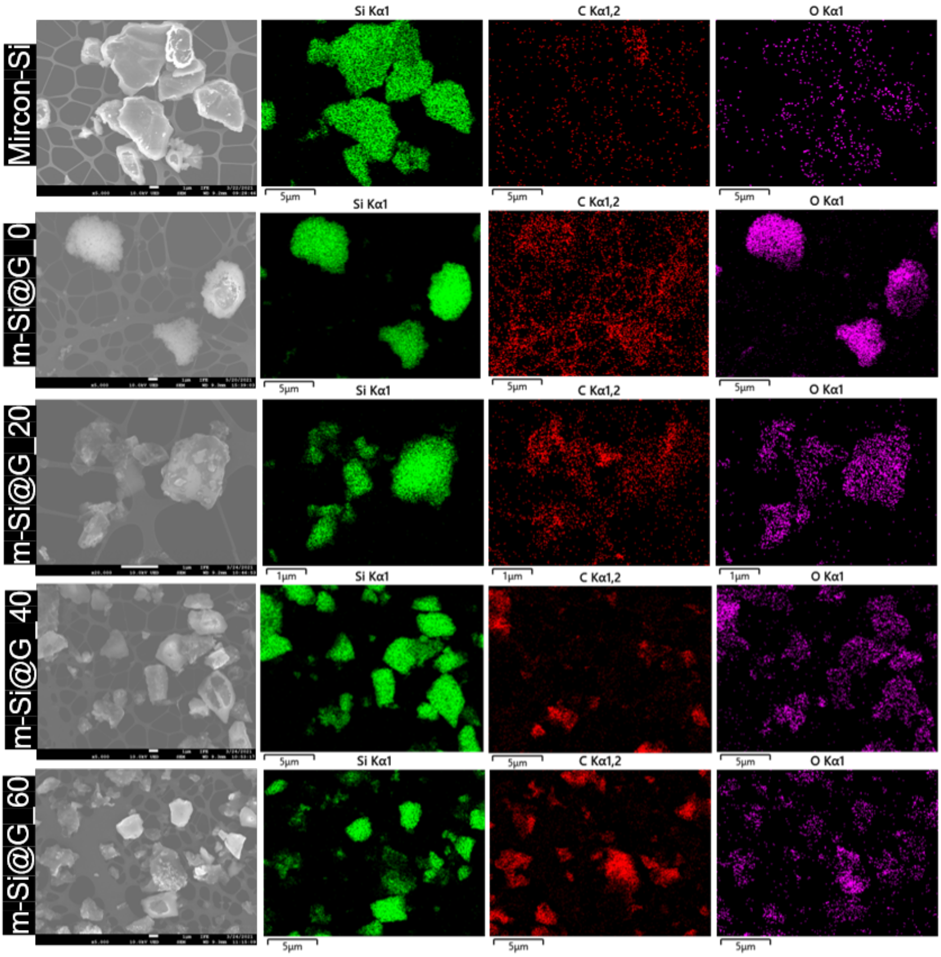
Mircon-Si
Si Kα1
C Kα1,2
O Kα1
5μm
m-Si@G_0
Si Kα1
C Kα1,2
O Kα1
5μm
m-Si@G_20
Si Kα1
C Kα1,2
O Kα1
1μm
m-Si@G_40
Si Kα1
C Kα1,2
O Kα1
5μm
m-Si@G_60
Si Kα1
C Kα1,2
O Kα1
5μm

Figure 4.40: EDS-analysis maps of Si, C and O for pristine Micron-Si, m-Si@G_0, m-Si@G_20, m-Si@G_40, and m-Si@G_60. Counts: Green = Si, red = C and purple = O

4.3.3 Galvanostatic cycling

The galvanostatic cycling results of the glucose-based samples are shown in Figure 4.41. The average initial capacities were decreasing with increasing C content, however, large standard deviations were seen for some half-cells. The average initial capacity of m-Si@G_0 was reduced by ∼17% compared to the pristine Micron-Si. Initial capacities are listed in Table 4.4. The capacity retention is seen in Figure 4.42. A rapid capacity loss of ∼50% was seen for m-Si@G_0 and m-Si@G_40 in the formation cycles, compared to ∼20% for m-Si@G_20 and m-Si@G_60. After around 30 cycles, stable cycling with a limited loss for over 150 cycles was seen for the treated samples. m-Si@G_60 showed the highest retention of capacity and continuously increased from cycle 30 (∼25%) to cycle 100 (∼28%).

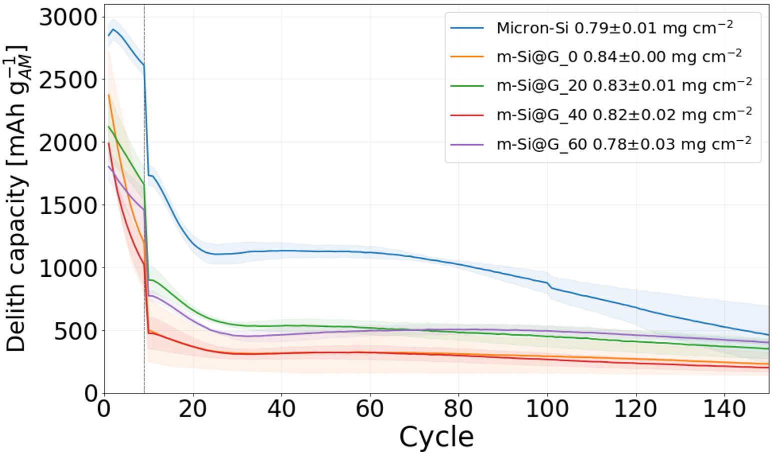

Figure 4.41: The galvanostatic cycling of Micron-Si, m-Si@G_0, m-Si@G_20, m-Si@G_40 and m-Si@G_60 (half-cells). The cycling included nine formation cycles 0.16 A g^{-1} followed by 1.6 A g^{-1}, marked by a bold grey vertical line.

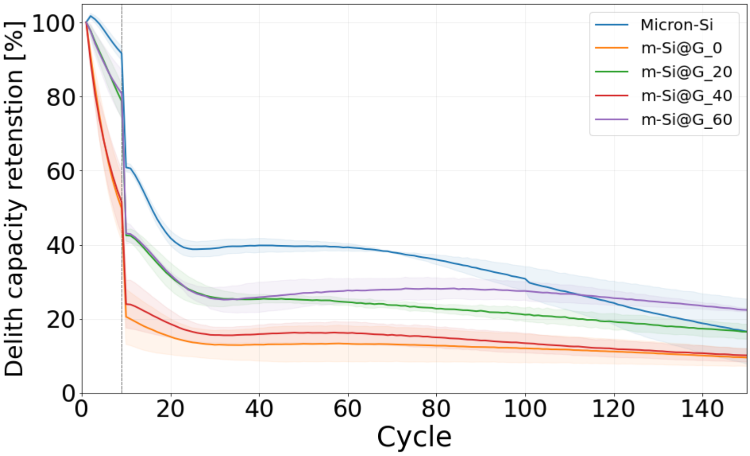

Figure 4.42: Capacity retention of Micron-Si, m-Si@G_0, m-Si@G_20, m-Si@G_40, and m-Si@G_60, normalized to the initial delithiation capacity.

Table 4.4: Initial delithiation capacity and capacity retention of the 9. and 100. cycle for Micron-Si, m-Si@G_0, m-Si@G_20, m-Si@G_40 and m-Si@G_60.

Sample	**Initial lith-capacity [mAh g^{-1}]**	**Cap retention (9. cycle) [%]**	**Cap retention (100. cycle) [%]**
Micron-Si	2848±90	92±1	31±3
m-Si@G_0	2373±359	50±9	12±4
m-Si@G_20	2120±275	78±5	21±2
m-Si@G_40	1988±16	52±9	13±3
m-Si@G_60	1803±108	81±6	28±2

The differential capacity plots showed similar behavior for Micron-Si, m-Si@G_20, m-Si@G_40 and m-Si@G_60 in the first three cycles. However, a high narrow peak at ~0.45 V was still present in the 2. and 3. cycle for the m-Si@G_0, as shown in Figure 4.43. This narrow peak is associated with the delithiation of c-$Li_{3.75}Si$ to a-$Li_{1.1}Si$.[50]

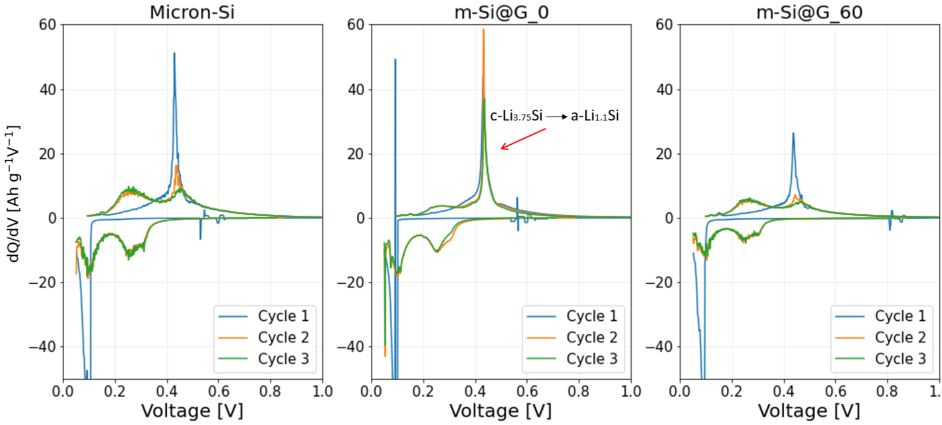

Figure 4.43: Differential capacities of the first three cycles for Micron-Si, m-Si@G_0 and m-Si@G_60. The curves are derived from one representative cell.

4.3.4 n-Si/C composites

Synthesis and C content

The n-Si/C composites remained as powders after carbonization. After ball-milling, the C contents were measured and shown in Figure 4.44. An increase in C content with the increase in glucose was seen, however, samples n-Si@G_40 and n-Si@G_60 had significantly lower concentrations compared to the m-Si@G_40 and m-Si@G_60.

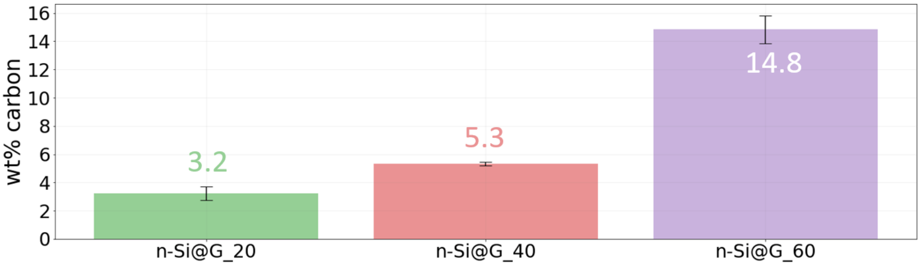

Figure 4.44: C content of n-Si@G_20, n-Si@G_40, and n-Si@G_60 after carbonization.

SEM

SEM-images of the particle powders, after ball-milling, are shown in Figure 4.45. The bulk of n-Si@G_0 were agglomerated to form structures in the micron range, as shown in Figure 4.45 a). The n-Si@G_20, n-Si@G_40, and n-Si@G_60 looked to be similar, as the bulk of the nanoparticles were in the form of micron-sized "chunks". Some smaller "chunks" or single particles, in the nano-range, were also seen, shown in Figure 4.45 b), c) and d).

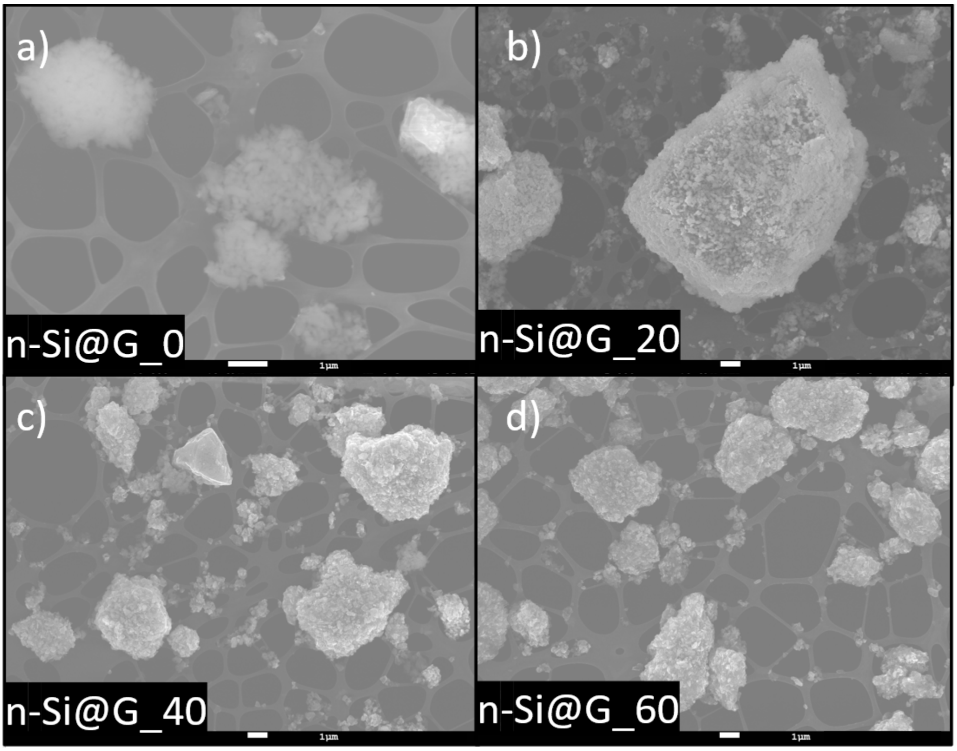

Figure 4.45: SEM-images of a) n-Si@G_0, b) n-Si@G_20, c) n-Si@G_40, and d) n-Si@G_60, after carbonization and ball-milling.

EDS

The same EDS-analysis mapping was done for the samples with n-Si, as shown in Figure 4.46. An increase in C counts from the background was seen for Nano-Si and n-Si@G_0. In the n-Si@G_0, C counts were detected in the same area as Si and O. This was also seen for n-Si@G_40 (5.3 wt% C) and n-Si@G_60 (14.8 wt% C). However, for n-Si@G_20 (3.2 wt% C), only the Si- and the O-map matched.

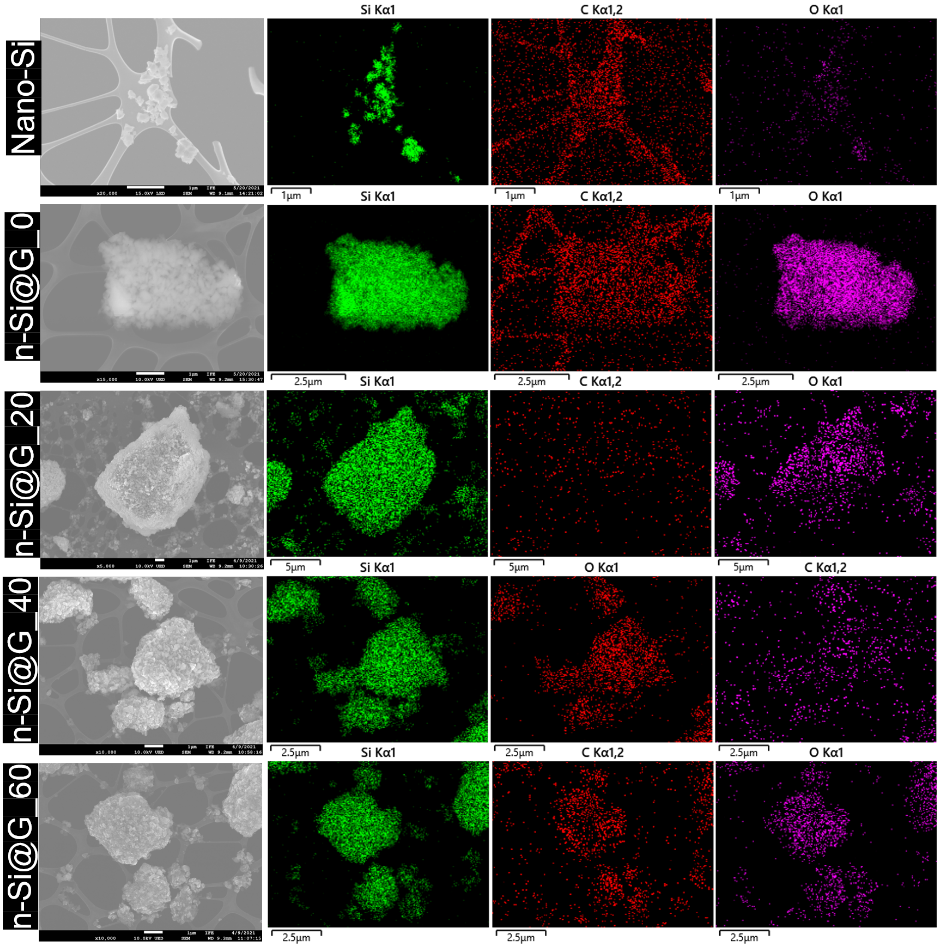
Nano-Si
Si Kα1
C Kα1,2
O Kα1
1μm
1μm
1μm
n-Si@G_0
Si Kα1
C Kα1,2
O Kα1
2.5μm
2.5μm
2.5μm
n-Si@G_20
Si Kα1
C Kα1,2
O Kα1
5μm
5μm
5μm
n-Si@G_40
Si Kα1
O Kα1
C Kα1,2
2.5μm
2.5μm
2.5μm
n-Si@G_60
Si Kα1
C Kα1,2
O Kα1
2.5μm
2.5μm
2.5μm

Figure 4.46: EDS-analysis maps of Si, C and O for pristine Nano-Si, n-Si@G_0, n-Si@G_20, n-Si@G_40, and n-Si@G_60. Counts: Green = Si, red = C and purple = O

Galvanostatic cycling

The long-term galvanostatic cycling results are shown in Figure 4.47. The average initial capacities are listed in Table 4.47. The standard deviations for the Si/C composites were significant. A relation between the C content and initial capacity, as previously shown, was not seen. However, compared to the n-Si@G_0, a significant increase in average capacity was seen for the samples obtained with glucose. The average initial capacity of n-Si@G_0 was reduced to about one-third of the pristine Nano-Si, however, a continuous increase in capacity was seen for all nine formation cycles. A total capacity increase of ∼57%, was demonstrated in the last formation cycle. Overall, the n-Si@G_20 had the highest capacity after 100 cycles, 559 mAh g^{-1} (∼43 % capacity retention).

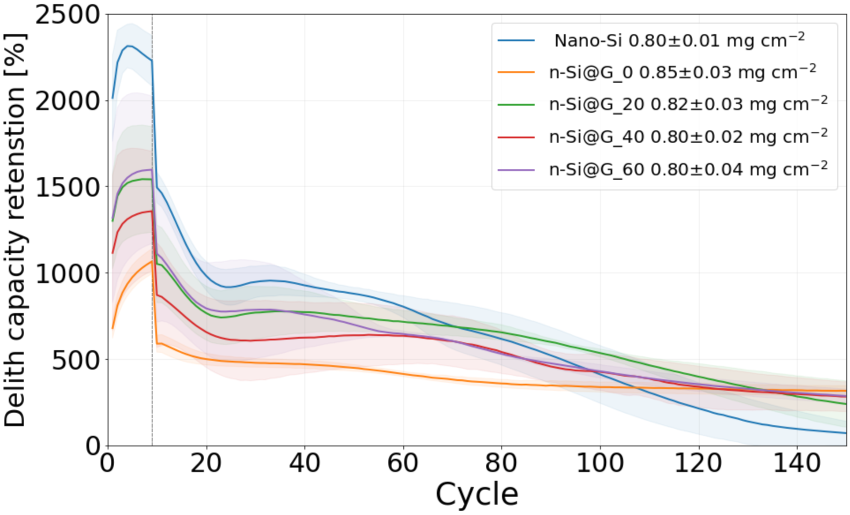

Figure 4.47: The galvanostatic cycling of Nano-Si, n-Si@G_0, n-Si@G_20, n-Si@G_40 and n-Si@G_60 (half-cells). The cycling included nine formation cycles 0.16 A g^{-1} followed by 1.6 A g^{-1}, marked by a bold grey vertical line.

Table 4.5: Initial delithiation capacity and capacity retention of the 9. and 100. cycle for Nano-Si, n-Si@G_0, n-Si@G_20, n-Si@G_40 and n-Si@G_60.

Sample	**Initial lith-capacity [mAh g^{-1}]**	**Cap retention (9. cycle) [%]**	**Cap retention (100. cycle) [%]**
Nano-Si	2012±249	113±21	21±9
n-Si@G_0	679±58	157±4	50±1
n-Si@G_20	1300±276	119±2	43±10
n-Si@G_40	1115±450	126±20	40±6
n-Si@G_60	1318±489	124±13	36±16

The differential plots of Nano-Si, n-Si@G_0, and n-Si@G_20 are shown in Figure 4.48. The peak associated with the initial lithiation of c-Si (cycle 1) was shifted to lower potentials for n-Si@G_0 and n-Si@G_20 compared to the Nano-Si. However, the shift was larger for n-Si@G_0 and the lithiation occurred right before the cut-off voltage of 50 mV. The delithiation peak around ∼0.45 V was also slightly narrower compared to Nano-Si and n-Si@G_20.

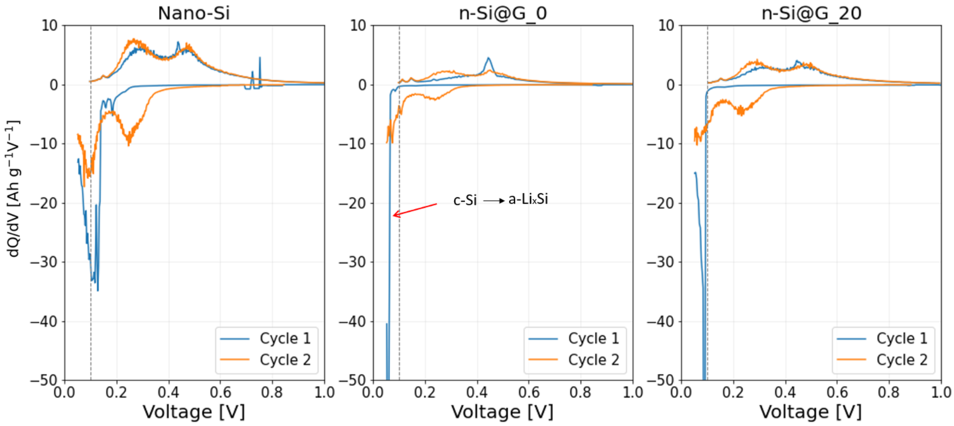

Figure 4.48: Differential capacities of the first two cycles for Nano-Si, n-Si@G_0 and n-Si@G_20. The potential of 0.1 V is marked with a grey bold vertical line. The curves are derived from one representative cell.

5. Discussion

5.1 Industrial grade Si

5.1.1 Material characterization

The XRD analysis suggests crystalline structures for both industrial-grade Si-powders. The diffraction peak broadening seen for n-Si is commonly seen as the particle sizes are reduced to the nano-range.[108] However, in the differential capacity plot of nano-Si, a peak associated with the lithiation of amorphous Si was seen in the first cycle (∼0.25 V). It is therefore suggested that the nano-Si might contains some amorphous phase that could also lead to peak broadening. The process of obtaining the industrial-grade m- and n-Si is not known, however, they are believed to be milled. If so, the formation of a two-phase amorphous and crystalline Si would be in accordance with the results previously reported by Shen *et al.*[109] High-energy milling has also been shown to induce lattice strain in the structure which would also contribute to the peak broadening.[24] This is not taken into account when the crystallite sizes were calculated with the Scherrer-equation.

Both powders had physisorption isotherms typical for non-porous materials, as seen in Figure A.1, in Appendix.[101] The SSA of n-Si was three times that of m-Si, which would be expected as the particle size is reduced. However, as nanoparticles are prone to form agglomerates, the "actual" SSA of the particles might be higher. As a result of the higher total active material surface exposed to the electrolyte, an increase in SEI formation is expected in the first cycle. The initial CE of n-Si was 8% lower than for the m-Si (∼90%). As Li is trapped in the SEI, low CE is detrimental in a full-cell, due to the limited Li-inventory. In half-cells, the Li-inventory will not be limited.

5.1.2 Electrochemical testing

The large initial capacity difference between m-Si and n-Si is speculated to originate from a difference in the amount of amorphous SiO_X. Since Si is oxidized to form a SiO_X surface layer in air, the increased surface area of the n-Si would lead to an increase in the total wt% SiO_X. Wang *et al.* ball-milled commercial Si (size = 1-2 µm) to a nanosized powder (size = 100-200 nm) under an inert Ar-atmosphere and reported an oxygen increase from 5.6

to 11.7 wt%.[110] If high-energy milling of the n-Si (Elkem) took place in air, a thicker SiO_x surface layer would be expected as the oxygen and increased temperature would promote the formation. The increased temperature would increase the diffusion rate of O_2 through the SiO_x to react with the Si core. Increased thickness of SiO_x surface layers has been reported to decrease the initial capacity.[111] A thicker SiO_x has been reported to increase the impedance of the cell, which could limit the lithiation of the Si-core.[112] The increase in impedance would lead to higher overpotentials meaning that the cut-off potentials were reached earlier which limits the capacity.[113] Electrochemical impedance spectroscopy could be used to study the differences in impedance between m-Si and n-Si. Measuring the O-content would also be crucial in understanding the large capacity discrepancy between the two powders.

A significant difference in the cycling behavior was observed, for n-Si and m-Si in the formation cycles. This became more obvious as the formation cycles were increased from three to nine. In the fourth cycle, the capacity of n-Si had increased by an average of 300 mAh g^{-1}, while the capacity of m-Si was slightly reduced (-12 mAh g^{-1}). SiO_2 and SiO are Li-reactive and form Si as they are electrochemically cycled.[110] An increase in capacity with increasing cycle index has been reported for SiO_2-anodes and might be the reason for the different cycling behavior in the formation cycles, assuming n-Si has a higher SiO_x.[114, 96] However, the capacity increase with increasing cycle index may also be explained by the fact that nanoparticles readily form agglomerated structures. If these structures are not sufficiently broken apart in the slurry, the particles in the agglomerate-core could suffer from the low electrical conductivity of Si and insufficient electrolyte wetting. As the structure expands and contracts during cycling, an improvement might be seen as more material is accessed. Ultrasonication of the slurry might be necessary to break the agglomerates.

Increasing the thickness of the SiO_x surface layer has been reported to increase the capacity retention.[111] This is related to the irreversible formation of inactive Li-oxides that form as Li reacts with the SiO_x at the surface. The Li-oxides are proposed to serve as a buffer, alleviating the volume expansion of Si.[110] The n-Si had higher capacity retention in the first 40 cycles compared to m-Si. However, as the initial capacity of n-Si is limited, this also limits the total volume expansion of the particles. This could reduce the cracking of particles and improve the mechanical stability of the electrode. However, a rapid capacity loss is seen at a lower cycle index compared to m-Si. This has been reported as the point of the total consumption of the FEC additive in the electrolyte.[68] The higher SSA and lower

CEs in the formation cycles, for n-Si, might suggest more SEI-formation and thereby earlier consumption of FEC.

5.1.3 Heat-treatment of the Si-powders

Heat-treating the Si-powders at 820°C led to narrower diffraction peaks, which was expected due to the growth of crystallite sizes with increased temperature.[115] The large narrowing in the peaks seen for n-Si is likely to also be attributed to the crystallization of an amorphous phase. Such a phase has been reported to crystallize at 660 °C.[109] This was supported by the reduction of the differential capacity peak, associated with the lithiation of a-Si ($\sim$0.25 V), in the first cycle. The initial lithiation of c-Si at $\sim$0.1 V is shifted to a lower potential (higher overpotential) compared to the lithiation of a-Si, due to the higher energy necessary to break Si-Si-bonds in c-Si. In the heat-treated n-Si, a narrower peak at $\sim$0.45 V was observed. The peak is associated with the delithiation of a metastable phase c-$Si_{3.75}$, that forms during lithiation, at low potentials. The phase is highly unwanted because it is associated with a large overpotential during delithiation and will lower both the energy efficiency and operating voltage of a cell.[50] The cut-off potential of 50 mV was used in an attempt to limit the formation of this phase. This is shown in Figure 5.1. No major changes in the initial capacities were seen after heat treatment. This is supported by the results of Wang *et al.*, which reported that no change in the oxygen content was seen after heat-treatment at 600°C (4h) under an inert atmosphere.[110]

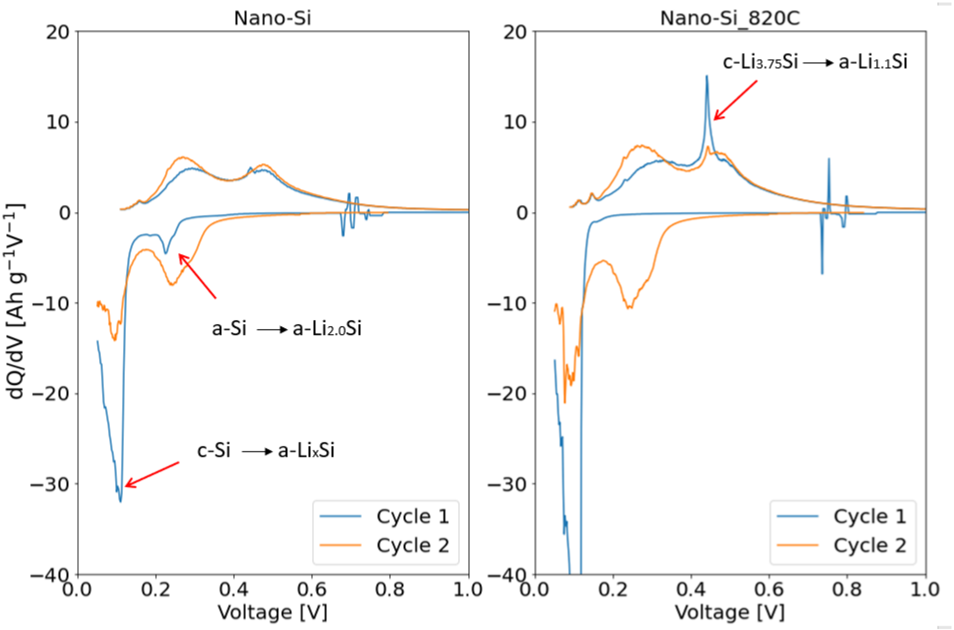

Figure 5.1: Differential capacities of n-Si before and after heat-treatment, for the first two cycles. The curves are derived from one representative cell.

5.2 Si/C composites with RF-resin

5.2.1 Synthesis and reference

The zeta-potential of +46 mV achieved by a 1:1 wt% of m-Si and CTAB was deemed sufficient in achieving a stable suspension of particles. Further increasing the CTAB concentration had been reported to only give a slight increase in zeta potential over >50 mV.[88] The synthesis of spherical polymer particles with a narrow PSD was successfully achieved at high concentrations of R and F, in line with the literature. After carbonization, similar particles have been reported to be microporous with extremely high SSA (>500 m^2 g^{-1}).[116] This could explain the low CE of ∼48%, as significant SEI formation would be needed to passivate the surface. The peaks observed in the differential capacity plot for the first cycle are related to the reduction of the electrolyte and the formation of the SEI layer. The following high CEs (>99.5%) suggest the formation of a stable SEI layer and minor volume expansion. The reversible capacity of ∼200 mAh g^{-1} is in line with the literature.[97] However, the capacity contribution from CB, 25 wt% in these cells, was not considered. Based on reported experiments, the contribution of CB is assumed to be between 50 and 100 mAh g^{-1} at a current rate of 1.6 A g^{-1}.[117] The C content of the carbonized RF-resin was determined to be 96.6 wt%. This would indicate that some functional groups of O and H would be present in the structure. However, the sample was not degassed or dried before firing and thus may also contain water. The presence of functional groups, such as -OH, has been reported when RF-resin was carbonized at 600°C (2h).[118] A decrease in O-groups at the surface of hard carbon with increased carbonization temperature has also been reported.[119] Higher temperatures give higher graphitic ordering and increased electrical conductivity.[119] Higher ordering reduces the number of defects and edges in the structure which are the sites that are commonly terminated by an O-group.[120] It is important to highlight the potential importance of these groups in a core-shell design. Since the PAA is grafted to the surface of Si particles under acidic conditions to give increased stability, changing the surface properties of the Si with a C shell could therefore limit this grafting reaction. The functional groups could also improve the electrolyte wetting of the electrodes. Therefore, using 13C-NMR or X-ray photoelectron spectroscopy (XPS) to investigate surface functional groups at different carbonization temperatures and optimize the amount, would be valuable.

The suspensions with m-Si and increasing amounts of RF-resin, showed some visual differences after the aging overnight. For m-Si@RF_0 m-Si@RF_40 and m-Si@RF_60, all Si particles did not settle, even after centrifuging at 4400 rpm (max). The particles, most likely nano-sized, were therefore decanted out in the washing steps. The washing step intended to wash out CTAB and possible residual of R and F. Most Si particles in m-Si@RF_80 seemed to settle. Therefore, it is believed that less Si was decanted out in the washing steps. The supernate of m-Si@RF_80 looked similar to the pure RF-resin supernate. After washing and centrifugation, it became apparent that particles with the same color as the pure RF-resin settled on top of the Si particles. Since TEM confirmed a high concentration of pure C spheres after carbonization, the pink particles were mostly pure RF-polymer particles. In retrospect, separating the two layers by reducing the centrifugation speeds to keep the lighter polymer particles in the water/ethanol, would be beneficial. The powder would reduce the total amount of low-capacity hard carbon while including the polymer that was coated to the Si, essentially, the only C that was desirable in improving the performance of the Si.

5.2.2 Material characterization

The flash analysis and initial delithiation capacity suggested a similar C content in m-Si@RF_60 and m-Si@RF_80, 29.1 wt% and 33.2 wt%, respectively. This could be explained by the increased loss of Si in the washing step for m-Si@RF_60. However, if the polymerization reactions were not complete after aging overnight, the extra R and F would be washed out, as they are soluble in water and thus explain the similar C contents in m-Si@RF_60 and m-Si@RF_80.

The BET-analyses showed a decrease in the SSA for m-Si@RF_0, m-Si@RF_40, and m-Si@RF_60, compared to the pristine m-Si. The reason for the reduced SSA in m-Si@RF_0 remains unclear but could be explained by the fact that the smallest particles were expected to be washed out in the coating procedure. Ostwald ripening leading to particle growth in the carbonization step could also decrease the SSA. TEM revealed that the coated particles in m-Si@RF_40 and m-Si@RF_60 most often consisted of multiple Si particles encapsulated by a thick C layer. Thereby, increasing the overall particle sizes and reduce surface area. The extreme SSA value of m-Si@RF_80 was a result of its microporous character. The BET-analysis is not valid for microporous materials at the pressures it was ran at, due to the nitrogen pore-filling that occurs at low pressures. The obtained SSA is therefore inaccurate. The reason why m-Si@RF_40 and m-Si@RF_60 did not appear to have a microporous structure remains unclear, however, the porosity has been reported to vary with the rate of polymerization.[121]

After carbonization, SEM-images revealed a high number of spherical particles and a significant change in morphology in m-Si@RF_40, m-Si@RF_60, and m-Si@RF_80. In m-Si@RF_40 these spheres were distorted and TEM revealed that they were a result of a thick C layer encapsulating smaller Si particles. The same was seen for m-Si@RF_60, however, the spheres were less distorted than for m-Si@RF_40, which is explained by the increased thickness of the C layer. The spheres in m-Si@RF_80 were completely spherical because they contained only C or had extremely thick layers. SEM also revealed the same trend for the larger irregular shaped Si particles, in which increased coating thickness gave more rounding of the particles. This confirms that SEM can be used to indicate the formation of a C surface layer on irregular micron-sized particles, however, with great caution.

The lack of polymerization at the surface of m-Si@RF_80 is believed to be a result of the high RF-resin concentration which increases the reaction rate. The increase in reaction rate allow for the formation of particles in the solution and not at the proposed energetically favored surface of the Si particles. These initial particles become the favored sites for further polymerization and the particles grow. In order to promote polymerization at the surface, a decrease in RF concentrations, temperature and pH could be beneficial as it would slow the polymerization reaction.[121, 88]

The initial EDS-mapping done with the SEM, clearly indicated that C was present on the Si particles in samples m-Si@RF_40, m-Si@RF_60, and m-Si@RF_80 and not in m-Si@RF_0. This was later confirmed by TEM. This EDS-mapping proved to be a fast and easy method in determining the relative positions of the elements of interest, however, with great limitations in terms of accuracy and determining the nature of the C. This includes the thickness and homogeneity. The C map of m-Si@RF_80 did not differ significantly from the C maps of m-Si@RF_40 and m-Si@RF_60, even though TEM revealed huge differences in the C thickness.

TEM revealed that Si/C core shell composites structures were successfully achieved for m-Si@RF_40 and m-Si@RF_60. The amorphous C-coating was complete and with homogeneous thickness. The amount of RF-resin was increased by a factor of 2.2 between m-Si@RF_40 and m-Si@RF_60 and the thicknesses roughly doubled from 50-70 nm to 100-150 nm. The method has therefore easy tunability in terms of C layer thickness. However, as the RF-concentration was further increased in m-Si@RF_80, the opposite trend was seen as most C formed as spherical particles. The SiO_x surface layers of m-Si@RF_0 and m-Si@RF_80 showed similar thicknesses. The C layers made for m-Si@RF_40 and m-Si@RF_60 are a lot thicker than the optimal amount previously reported for Si nanoparticles. Luo *et al.* reported an optimal thickness of 10 nm for nanoparticles with a diameter of ~80 nm.[4] That was achieved with a 50 wt% Si and 50 wt% resorcinol, under similar reaction conditions (same temperature and reaction time). Thus highlighting the strong relationship between SSA and the achieved C-coating thickness.

5.2.3 Galvanostatic cycling

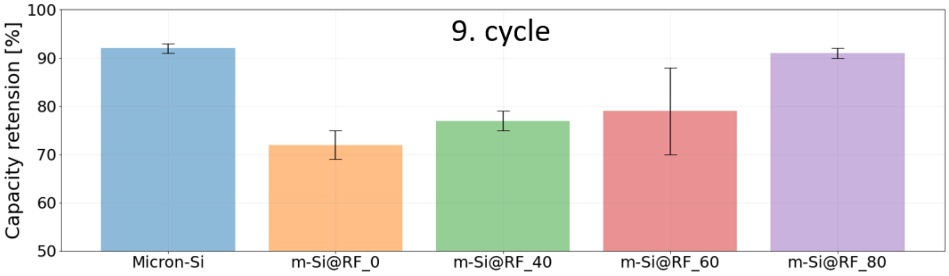

Figure 5.2: Delithiation capacity retention in the ninth cycle for Micron-Si, m-Si@RF_0, m-Si@RF_40, m-Si@RF_60, and m-Si@RF_80.

The galvanostatic cycling revealed significant differences between the Micron-Si and m-Si@RF_0, indicating that the C-coating procedure changed the Si particle properties. This is illustrated in Figure 5.2, which shows the capacity retention in the ninth cycle. The SiO_x surface layer has been shown to grow in contact with water and the oxidation rate increases with the increase in pH.[122, 123] The reaction suspension was slightly alkaline (pH = ~8), however, the TEM revealed a narrow oxide layer (1-7 nm) which is not considered as a thick layer in previous research.[111] Sim *et al.* reported an optimum SiO_x thickness of 7 nm for Si nanowires anodes.[111] If an increase in the total SiO_x content is true for m-Si@RF_0 compared to the Micron-Si, it would be expected to have lower initial capacity, however, this was not the case, as seen in Figure 4.2.[112] The increased capacity losses of m-Si@RF_0 are not expected to be caused by the carbonization step, as previously demonstrated in Section 4.1.3. The only notable difference in the differential capacity plots for Micron-Si and m-Si@RF_0 was in the doublet peak (~0.25–0.3 V) associated with the lithiation of a-Si to a-$Li_{2.0}Si$, as seen in Figure 5.3 a) and b). A faster disappearance of the shoulder peak (~0.3 V) was seen in the formation cycles for m-Si@RF_0 and is marked with a red arrow in Figure 5.3 b). This means that the initial lithiation of a-Si is shifted to lower potentials. The reason for this behavior remains unclear and further investigations are needed.

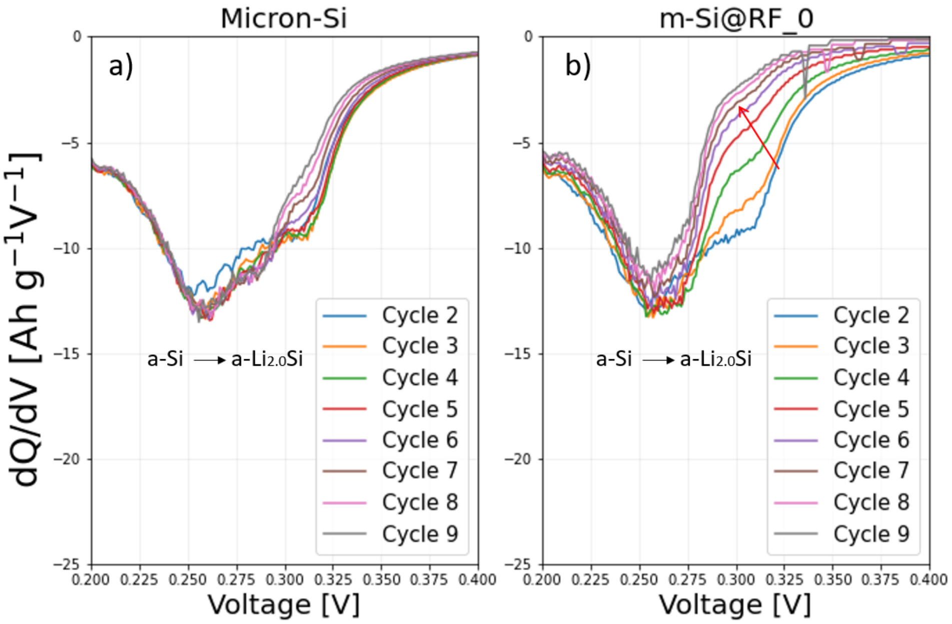

Figure 5.3: Lithiation differential capacities of cycles 2-9 for a) Micron-Si and b) m-Si@RF_0, between 0.2 and 0.4 V.

The differences in the initial capacity retention between the highly C-coated m-Si@RF_40 and m-Si@RF_60, and the mainly uncoated m-Si@RF_80 show higher retension for m-Si@RF_80, as seen in Figure 5.2. The standard deviation of m-Si@RF_60 is large, however, the same trend was also shown in the cells where Si-loadings were matched. The reason for the decreased cycling stability in the formation cycles for the coated samples remains unclear. However, a finite element analysis on C-coated Si nanoparticles have suggested that a C shell may result in increased fractures which had been experimentally shown for C-coated nanoparticles.[124] The core shell structures in m-Si@RF_40 and m-Si@RF_60 were revealed to often consist of multiple irregular shaped Si particles, encapsulated by C. During lithiation of the core, the volume expansion would be anisotropic with high tension stress on the C-coating. This could lead to intensive fractures and unstable SEI. However, this is highly speculative and the behavior difference could also be described by differences in the SEI layer or the binder-particle interaction. Post-mortem analysis of cycled cells would be beneficial to shed light on the differences.

Lower initial capacities for the Si/C composites, compared to the Micron-Si, were expected as they contained less Si. However, based on the capacity and amount of hard carbon, the capacities were lower than expected. Nava *et al.* studied the lithiation of amorphous C-coated Si and showed that full lithiation of the Si particles did not occur.[74] They proposed that the amorphous coating either prevented the transport of Li through the C or that the C shell mechanically constrained the expansion of the Si core. The first hypothesis contradicts previous research.[125] As the current was increased by a factor of ten, a larger drop in capacity was seen for the samples with thick C-coating compared to m-Si@RF_80, suggesting that the C-coating limits the full lithiation of the Si core at high current rates. This could also explain the following cycling behavior, as m-Si@RF_40 and m-Si@RF_60 cycled stably at a low capacity. Limiting the capacity and volume expansion in order to achieve sufficiently high stability would be beneficial, however, this was not the case for m-Si@RF_40 and m-Si@RF_60 as the capacity was too low compared to the pristine Si.

Increasing capacity with increasing cycle index was seen after ∼25-30 cycles for all samples. This *pseudo* "self-healing"-mechanism is in line with previous work and is proposed to be related to the highly lithiated phase, a-$Li_{3.5}Si$.[126, 65] Firstly, as the cycling current is increased, the formation of this phase is substantially decreased, which leads to a large decrease in the capacity. In other words, the Si becomes "self-limiting", by restricting the formation of this phase. This results in the stabilized capacities seen in Figure 4.27. As the cycling continuous, the formation of a-$Li_{3.5}Si$ occurs again, leading to an increase in capacity. Restricting the formation of a-$Li_{3.5}Si$ is proposed to be related to the SEI and electrolyte additives.[65] After ∼100 cycles, the average capacity of m-Si@RF_0 was higher than Micron-Si. This could be explained by the fact that the fast reduction in capacity, for m-Si@RF_0, makes the Si "self-limiting" at an earlier stage and therefore having less volume expansion and electrolyte consumption. The self-limiting behavior followed by the *pseudo* "self-healing"-mechanism is illustrated in the differential capacities of m-Si@RF_40, m-Si@RF_60, and m-Si@RF_80, shown in Figure 5.4. The disappearance of the lithiation peak at ∼0.1 V was seen for all the Si/C composites. This peak is associated with the highly lithiated phase, $Li_{3.5}Si$.[126] For m-Si@RF_80, this peak was less dominating in the overall lithiation compared to m-Si@RF_40 and m-Si@RF_60. Furthermore, the peak also disappeared at a lower cycle index for m-Si@RF_80, as shown in cycles 15 and 20 in Figure 5.4 (red arrows). The peak reappeared for all samples at a higher cycle index.

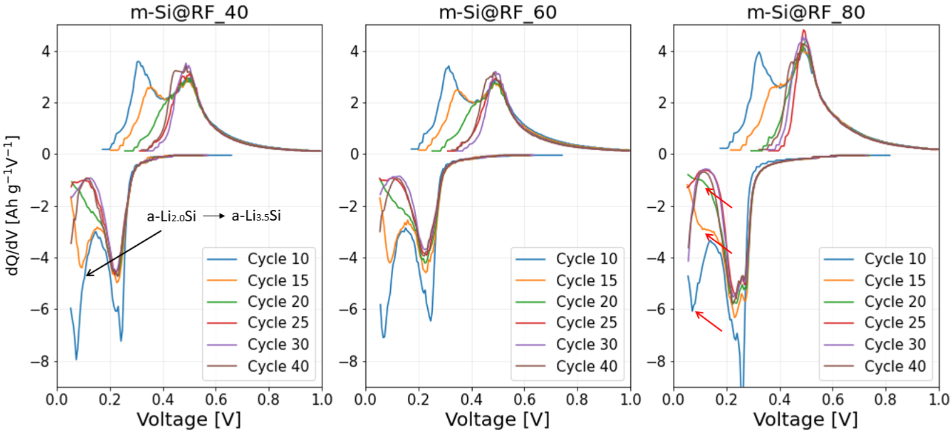

Figure 5.4: Differential capacities of m-Si@RF_40, m-Si@RF_60 and m-Si@RF_80 for cycle 10, 15, 20, 25, 30 and 40 (I = 1.6 A g^{-1}). The curves are derived from one representative cell.

The m-Si@RF_80 demonstrated ~10% higher capacity retention after 100 cycles, compared to Micron-Si, however, in terms of equivalent cycles, the Micron-Si outperforms all samples for the first 100 cycles. Instead, limiting the capacity of industrial-grade micron-sized Si to around 1000 mAh g^{-1} has been shown to be an effective strategy in increasing the capacity retention and cycle life.[127] The internal resistance measurements of Micron-Si and m-Si@RF_80 showed a correlation to the rapid capacity loss seen at around 100 cycles. Extensive SEI growth after this point would reduce the Li^{+}-conductivity and increase the cell's internal resistance.[104] Increasing the total loadings to have matching Si-loadings demonstrated earlier capacity losses for m-Si@RF_80. This would be expected as the total surface area and active material expansion would consume the electrolyte additives at a higher rate.

Rate-testing

Micron-Si and m-Si@RF_80 demonstrated the best rate performance. The major capacity losses off m-Si@RF_0 in the formation cycles and the low initial capacities of the Si/C composites made it difficult to directly compare the effects of increasing the cycling rate. However, normalization to the capacity of the last formation cycle made it apparent that Micron-Si and m-Si@RF_80 retained higher capacities as the current was increased. The restored capacity as the current was decreased was also higher for Micron-Si and m-Si@RF_80, indicating less irreversible losses during the rate-testing. The rate testing supported that the thick C-coatings of m-Si@RF_40 and m-Si@RF_60 were limiting the full lithiation of the core Si, as proposed earlier. This was not seen for m-Si@RF_80. The samples showed increasing overpotentials with increasing rates which explains the decreased capacities seen for all samples. By comparing the rate performances of m-Si@RF_0 and m-Si@RF_80 it became clear that the extra C did improve the performance.

Full-cells

The m-Si@RF_0 also demonstrated rapid capacity losses in a full-cell. The cycling behaviors of Micron-Si and m-Si@RF_80 were similar, however, a higher capacity loss and low CE was seen in the first cycle of m-Si@RF_80. Since the m-Si@RF_80 powder had a lower specific capacity compared to the pristine Si, a higher loading had to be used in order to match the capacity of the cathode. The increased total active material means more SEI-formation and Li-trapping. Since the amount of Li is limited in a full-cell, the losses are not restored, as seen in a half-cell. The higher loading used for m-Si@RF_80 also means that the battery has a lower gravimetric energy density, compared to Micron-Si.

5.3 Si/C composites with glucose

5.3.1 m-Si/C composites

Coating procedure

The procedure of making m-Si/C composites with varying amounts of C was achieved. Even though all Si/glucose samples were hand-grinded to a powder before carbonization, the high glucose content in m-Si@G_60 meant that the sugar melted together to form one Si/C structure in the furnace. This was not seen for m-Si@G_20 and m-Si@G_40, however, the powders obtained from the furnace had increased particle sizes. An attempt to only hand-grind before electrode fabrication failed to give a homogeneous electrode cast and cells failed after a few cycles. Therefore, ball-milling was deemed necessary to obtain a homogeneous powder with reduced sizes. In order to keep the ball-milling step consistent within the different powders, they were milled equally. However, it was believed that the targeted powder sizes were obtained at an earlier stage for the powders with less C, thus making further ball-milling unnecessary. This was evident as the m-Si@G_60 was the only sample with particles left in the sieve. The SEM images suggested that the ball-milling was more destructive of the Si-structures containing less or no C.

The EDS-analysis mapping indicated that a mixture of Si particles, with and without C at the surface, was obtained after ball-milling. By comparing the SEM images and maps from EDS with the ones obtained from the composites made with RF-resin, it is clear that the same rounding of the edges was not present and that the C was more randomly distributed in the powders obtained with glucose. C-coatings with glucose have previously been reported to yield microporous structures with increased SSAs.[96] The CEs were not included in the results as they were inaccurate, however, initial testing with glucose gave decreasing CEs with increasing C content.

Galvanostatic cycling

The hard carbon reference cell of carbonized glucose cycled at ~160 mAh g^{-1} (1.6 A g^{-1}), which was about 20% lower than the reference cell from the RF-resin. However, the initial capacities were very similar. The highly polymerized structure of the RF-polymer particles was expected to have a higher graphitic order after carbonization, compared to the glucose. This would result in higher electrical conductivity and possibly explain the improved capacity retention as the current was increased by a factor of 10. Raman spectroscopy could be used in order to study the graphitization degree of the C structures.

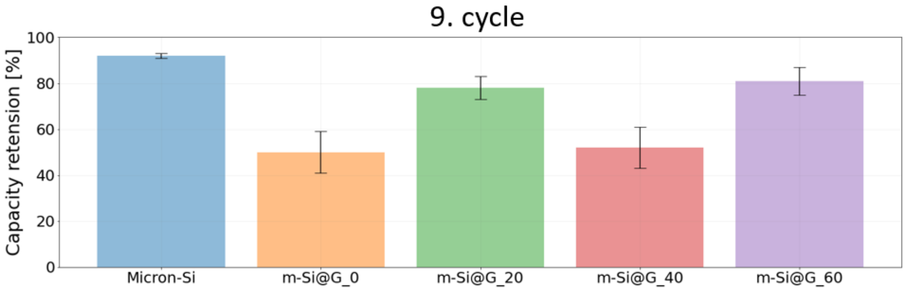

Figure 5.5: Delithiation capacity retention in the ninth cycle for Micron-Si, m-Si@G_0, m-Si@G_20, m-Si@G_40, and m-Si@G_60.

The galvanostatic cycling results revealed that the coating procedure decreased the initial capacity and capacity retention when no C was added. After nine formation cycles, the average capacity retention of m-Si@G_0 was only 50%, as shown in Figure 5.5. A lower initial capacity after ball-milling of industrial-grade micron-sized Si has previously been reported.[128] The growth of the SiO_x surface layer was proposed to be the reason. Improved capacity retention was seen for samples m-Si@G_20 and m-Si@G_60, compared to m-Si@G_0. However, the m-Si@G_40 showed similar behavior as m-Si@G_0. Therefore, a relation between C content and cycling performance was not seen.

The differential capacity plot is seen in Figure 4.43, and showed that the narrow delithiation peak at ~0.45 V still remained, for m-Si@G_0, after the first cycle. This narrow peak is associated with the delithiation of c-$Li_{3.75}Si$ to a-$Li_{1.1}Si$.[50] This phase has been related to large overpotential and forms during lithiation at potentials below the cut-off potential of 50 mV.[50] The peak normally disappears after the first cycle for c-Si, however, for m-Si@G_0, the narrow peak was present for the three initial cycles, which indicates that the phase either formed at potentials higher than the cut-off potential or that the actual potential dropped below 50 mV, before it was measured.

5.3.2 n-Si/C composites

Coating procedure

The C contents in n-Si@G_40 and n-Si@G_60 were a lot lower than the m-Si with the same Si/glucose ratios. The reason is not known but is speculated to originate from either the weighing out of n-Si or insufficient evacuation of oxygen in the furnace. Since the n-Si was received as a slurry with isopropanol, it was challenging to weigh out accurately as the isopropanol would evaporate readily. The two powders were also carbonized in a separate run compared to n-Si@G_20, which had the same C-content as m-Si@G_20. If oxygen was still present in the furnace, some C would burn off as CO_2. The SEM images revealed a highly agglomerated structure for the n-Si@G_0, even after being ultrasonicated in ethanol, in the sample preparation. The samples containing C showed similar structures with a mix of micron-sized "chunks" and smaller nano-sized particles. EDS mapping revealed that the "chunks" of n-Si@G_40 and n-Si@G_60 consisted of C and Si. This was not clear for n-Si@G_20, which only contained 3.2 wt% C. The n-Si@G_0 also looked to have some C in the sample, which could be caused by C contamination from insufficient cleaning of the balls and vessel during ball-milling. It is worth mentioning that the EDS mapping of nano-Si and n-Si@G_0 were done on a separate occasion. No deliberate software changes were made, however, the counts from these two samples look to be a lot higher as the C film from the TEM-grid was clearly visible. The EDS analysis was also taken at different magnifications due to the different sizes. This highlights the great caution that must be taken when using EDS-mapping as a method of verifying C-coating. The method also proved to be insufficient in determining if there was any surface coating of individual n-Si particles, due to the limited accuracy.

Galvanostatic cycling

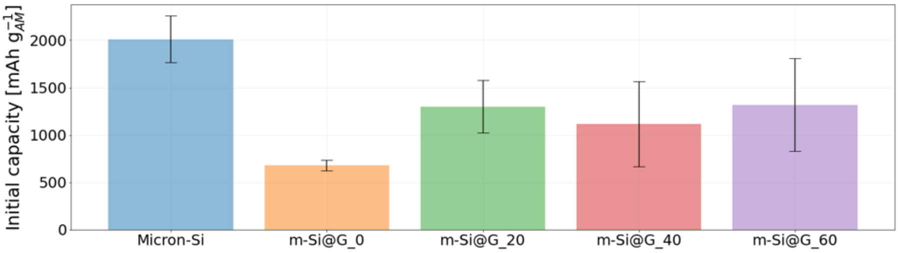

Figure 5.6: Initial delithiation capacity for Nano-Si, n-Si@G_0, n-Si@G_20, n-Si@G_40, and n-Si@G_60.

The initial delithiation capacities of the n-Si/C composites had extreme deviations between cells. The initial capacities are shown in Figure 5.6 The large size distribution of the so-called "chunks", are believed to give non-homogeneous electrode-castings, resulting in large variations. No relation between average initial capacity and C content was seen. However, the samples containing C demonstrated higher average capacities for the first 120 cycles compared to the n-Si@G_0. The average capacity increase with C can not be explained by the lithiation of the hard carbon alone, due to the low C contents and low capacity for the hard carbon (∼160 mAh g^{-1} at 1.6 A g^{-1}). Therefore, it is proposed that the C either improved the electrical contact between particles or that the C limits the oxidation of Si during the coating process/ball-milling. The n-Si@G_0 showed a shift towards a lower potential for the peak associated with the first lithiation of c-Si (normally ∼0.1 V), as shown in Figure 4.48. Therefore, the cut-off potential of 50 mV was likely met before fully lithiating the Si in n-Si@G_0. The increased overpotential leading to the shift in the lithiation peak is speculated to occur due to a thicker SiO_x-layer.

After around 70 cycles, the n-Si@G_20 surpassed the average capacity of the pristine Nano-Si. The increased stability of n-Si@G_20 is believed to be a result of its low initial capacity. Firstly, lower capacity means lower volume expansion and a more stable electrode layer. Secondly, less cracking of the SEI and consumption of electrolyte additives. In other words, limiting the initial capacity postpones the point of rapid capacity loss. This is one of the reasons why a direct comparison of composites and pristine Si is difficult. In terms of equivalent cycles, non of the powders would perform better. A strategy of also limiting the capacity of Si to around 1200 mAh g^{-1} would be a fairer comparison.

5.4 General remarks

In summary, reducing the bulk particle sizes from the micron-range to the nano-range of industrial-grade Si did not improve the cycling stability in half-cells and decreased the initial capacity. It was also determine that heat treating the industrial Si would not drastically affect the initial capacity. The RF-resin coating method proved to be successful in making Si/C core shell composites with high tunability, as long as the concentration did not exceed a critical amount. However, the samples with thick carbon layers (m-Si@RF_40 and m-Si@RF_60) did not demonstrate improved cycling performance compared to the pristine Si. The layers are proposed to be too thick as they were about 5 to 15 times thicker than the optimal layer thickness previously reported for Si.[4] The low capacities demonstrated by these samples are proposed to limit the lithiation of the Si core. This was supported by the fact that the sample with minor C-coating, but similar C content (m-Si@RF_80) cycled at a significantly higher capacity for the first 100 cycles. Therefore, a wt% ratio of 20% Si and 80% R was the optimal amount in this series, however, it is believed that reducing the RF-resin amount to reduce the rate of polymerization would make surface layers <50 nm, which would perform better than m-Si@RF_80. Although improving the performance of m-Si@RF_80 would be possible, the real question is if the Si/C core shell composites made from this specific method would actually outperform the pristine m-Si. Further work is necessary to answer that question.

Based on the EDS-mapping analyses, the m-Si/C composites made with glucose did not demonstrate complete surface C-coatings as was seen for m-Si@RF_40 and m-Si@RF_60. The coating method was found to be devastating to the capacity and only slight improvements with the presence of carbon was demonstrated. The optimal glucose amount in the series was found to be 60%, however, the sample was still outperformed by the pristine m-Si for the first 150 cycles. Due to the limited characterization, the reason for the decreased capacity remains unclear. Further investigates into the effects of the method is therefore needed.

The n-Si/C composites made with glucose had too similar C contents (3.2, 5.3, and 14.8 wt%) to distinguish any clear trend between C content and cycling performance. Large standard deviations were also demonstrated for the composites. Again, the method proved to be devastating for the capacity when no C was added but drastically improved with the addition of C. The n-Si/C composites benefited the most from the introduction of C and the sample with 20 wt% glucose demonstrated higher average delithiation capacities after around 70 cycles compared to the pristine n-Si.

6. Conclusion

Reducing the size of industrial-grade Si from micron-sized to nano-sized did not improve the cycling stability as they were long-term galvanostatically cycled in half-cells. A significant decrease in the initial delithiation capacity was seen as the size was reduced (-45%). Si/C core shell composites were obtained from coating irregular shaped micron-sized industrial-grade Si with an RF-resin and further carbonizing them in a furnace. The facile one-pot coating procedure yielded thick complete layers with homogeneous thicknesses (50-150 nm) for samples under a critical amount of RF-resin. Under the critical amount of RF-resin, the C thickness could be controlled by the amount of RF-resin added. Over the critical amount of RF-resin, the majority of C formed pure polymer spheres that were carbonized to hard carbon spheres. The Si/C composites suffered from low initial capacities as they were cycled in half-cells, and did not improve the average capacity of the pristine Si for the first 150 cycles. The composite with the least C-coating on the Si surfaces demonstrated the highest capacity and capacity retention for the first 150 cycles. A slight improvement in capacity retention with increased current rates was observed for the Si/C composite with the least coating, compared to the pristine Si. The composites with thick C layers demonstrated low retention in capacities with increased current rates and the C layers are proposed to limit the lithiation of the Si core.

Si/C composites with increasing C contents were obtained by using both the micron- and nano-sized industrial-grade Si powders and glucose. The nature of the C layers for the samples could not be determined but were believed to be incomplete and inhomogeneous. No improvement was shown for the first 150 cycles for the Si/C composites with the micron-sized Si. A slight increase in the capacity was seen for all composites of nano-sized Si after 100 cycles, compared to the pristine n-Si. The best performance was achieved with a composite containing 3.2 wt% C, which surpassed the average capacity of the pristine n-Si after around 75 cycles.

7. Further work

Controlling the polymerization reaction is key in obtaining C-coatings at the surface. Reducing the RF-resin amounts to make Si-core shell structures with thinner C layer thicknesses could be beneficial in approaching a potential optimum thickness. The RF-resin will also polymerize under acidic conditions, which could be a good strategy in order to reduce the oxidation of Si. The number of functional groups and the porosity of the C-coating are important factors that could be controlled by the carbonization temperature.[4, 96] Studying the effects of the carbonization temperature could therefore be beneficial in reducing the initial SEI-formation and to ensure a covalent bonding with the PAA-binder.

The ball-milling after carbonization was suspected to be too energy-intensive and possibly destructive of the C-coating. Ball-milling in an inert atmosphere would be beneficial to reduce the potential oxidization. Optimizing the carbonization temperature and increase the C content will be important for the glucose method.[96] TEM is also necessary in order to describe the nature of the C layer from glucose. Electrochemical impedance spectroscopy would be beneficial to determine if the C-coatings improve the kinetics and to understand the differences between the two industrial Si powders. Post-mortem analysis of cells to study the C-coating's effect on the SEI formation and to study the fracture resistance of the coated particles would also be beneficial.

Bibliography

[1] M. N. Obrovac and L. Christensen, “Structural changes in silicon anodes during lithium insertion/extraction,” *Electrochemical and Solid-State Letters*, vol. 7, no. 5, 2004.

[2] M. T. McDowell, S. W. Lee, W. D. Nix, and Y. Cui, “25th anniversary article: Understanding the lithiation of silicon and other alloying anodes for lithium-ion batteries,” *Advanced Materials*, vol. 25, no. 36, pp. 4966–4985, 2013.

[3] N. Liu, H. Wu, M. T. McDowell, Y. Yao, C. Wang, and Y. Cui, “A yolk-shell design for stabilized and scalable Li-ion battery alloy anodes,” *Nano Letters*, vol. 12, no. 6, pp. 3315–3321, 2012.

[4] W. Luo, Y. Wang, S. Chou, Y. Xu, W. Li, B. Kong, S. X. Dou, H. K. Liu, and J. Yang, “Critical thickness of phenolic resin-based carbon interfacial layer for improving long cycling stability of silicon nanoparticle anodes,” *Nano Energy*, vol. 27, pp. 255–264, 2016.

[5] N. Watts et al., “The 2020 report of The Lancet Countdown on health and climate change: responding to converging crises,” 1 2021.

[6] WMO, “United in Science 2020,” pp. 1–20, 2020.

[7] R. B. Johnston, “Arsenic and the 2030 Agenda for sustainable development,” *Arsenic Research and Global Sustainability - Proceedings of the 6th International Congress on Arsenic in the Environment, AS 2016*, pp. 12–14, 2016.

[8] M. V. Reddy, A. Mauger, C. M. Julien, A. Paolella, and K. Zaghib, “Brief history of early lithium-battery development,” *Materials*, vol. 13, no. 8, pp. 1–9, 2020.

[9] B. Nykvist and M. Nilsson, “Rapidly falling costs of battery packs for electric vehicles,” *Nature Climate Change*, vol. 5, no. 4, pp. 329–332, 2015.

[10] X. N. Penisa, M. T. Castro, J. D. A. Pascasio, E. A. Esparcia, O. Schmidt, and J. D. Ocon, “Projecting the price of lithium-ion NMC battery packs using a multifactor learning curve model,” *Energies*, vol. 13, no. 20, 2020.

[11] M. S. Ziegler and J. E. Trancik, “Re-examining rates of lithium-ion battery technology improvement and cost decline,” *Energy and Environmental Science*, vol. 14, pp. 1635–1651, 4 2021.

[12] BloombergNEF, “Battery Pack Prices Cited Below $100/kWh for the First Time in 2020, While Market Average Sits at $137/kWh.”

[13] E. Mossali, N. Picone, L. Gentilini, O. Rodrìguez, J. M. Pérez, and M. Colledani, “Lithium-ion batteries towards circular economy: A literature review of opportunities and issues of recycling treatments,” *Journal of Environmental Management*, vol. 264, 2020.

[14] V. Etacheri, R. Marom, R. Elazari, G. Salitra, and D. Aurbach, “Challenges in the development of advanced Li-ion batteries: A review,” *Energy and Environmental Science*, vol. 4, no. 9, pp. 3243–3262, 2011.

[15] A. M. Kuhlmann, “The Second Most Abundant Element in the Earth’s Crust,” *JOM*, vol. 15, pp. 502–505, 7 1963.

[16] X. Zuo, J. Zhu, P. Müller-Buschbaum, and Y. J. Cheng, “Silicon based lithium-ion battery anodes: A chronicle perspective review,” *Nano Energy*, vol. 31, no. October 2016, pp. 113–143, 2017.

[17] X. Li, M. Gu, S. Hu, R. Kennard, P. Yan, X. Chen, C. Wang, M. J. Sailor, J. G. Zhang, and J. Liu, “Mesoporous silicon sponge as an anti-pulverization structure for high-performance lithium-ion battery anodes,” *Nature Communications*, vol. 5, no. May, 2014.

[18] Y. Zhou, X. Jiang, L. Chen, J. Yue, H. Xu, J. Yang, and Y. Qian, “Novel mesoporous silicon nanorod as an anode material for lithium ion batteries,” *Electrochimica Acta*, vol. 127, pp. 252–258, 2014.

[19] H. Wu, G. Chan, J. W. Choi, I. Ryu, Y. Yao, M. T. Mcdowell, S. W. Lee, A. Jackson, Y. Yang, L. Hu, and Y. Cui, “Stable cycling of double-walled silicon nanotube battery anodes through solid-electrolyte interphase control,” *Nature Nanotechnology*, vol. 7, no. 5, pp. 310–315, 2012.

[20] T. Sri Devi Kumari, D. Jeyakumar, and T. Prem Kumar, “Nano silicon carbide: A new lithium-insertion anode material on the horizon,” *RSC Advances*, vol. 3, pp. 15028–15034, 9 2013.

[21] A. Ulvestad, J. P. Mæhlen, and M. Kirkengen, “Silicon nitride as anode material for Li-ion batteries: Understanding the SiNx conversion reaction,” *Journal of Power Sources*, vol. 399, pp. 414–421, 9 2018.

[22] N. Liu, Z. Lu, J. Zhao, M. T. Mcdowell, H. W. Lee, W. Zhao, and Y. Cui, “A pomegranate-inspired nanoscale design for large-volume-change lithium battery anodes,” *Nature Nanotechnology*, vol. 9, no. 3, pp. 187–192, 2014.

[23] I. H. Son, J. H. Park, S. Kwon, S. Park, M. H. Rümmeli, A. Bachmatiuk, H. J. Song, J. Ku, J. W. Choi, J. M. Choi, S. G. Doo, and H. Chang, “Silicon carbide-free graphene growth on silicon for lithium-ion battery with high volumetric energy density,” *Nature Communications*, vol. 6, no. May, pp. 1–8, 2015.

[24] M. Gauthier, D. Mazouzi, D. Reyter, B. Lestriez, P. Moreau, D. Guyomard, and L. Roué, “A low-cost and high performance ball-milled Si-based negative electrode for high-energy Li-ion batteries,” *Energy and Environmental Science*, vol. 6, no. 7, pp. 2145–2155, 2013.

[25] X. H. Liu, L. Zhong, S. Huang, S. X. Mao, T. Zhu, and J. Y. Huang, “Size-Dependent Fracture of Silicon,” *ACS Nano*, vol. 6, no. 2, pp. 1522–1531, 2012.

[26] O. U. Press, “Battery.”

[27] R. M. Dell and D. A. J. Rand, *Understanding Batteries*. RSC Paperbacks, The Royal Society of Chemistry, 2001.

[28] M. Winter and R. J. Brodd, “What are batteries, fuel cells, and supercapacitors?,” *Chemical Reviews*, vol. 104, no. 10, pp. 4245–4269, 2004.

[29] J. B. Goodenough, “How we made the Li-ion rechargeable battery: Progress in portable and ubiquitous electronics would not be possible without rechargeable batteries. John B. Goodenough recounts the history of the lithium-ion rechargeable battery,” *Nature Electronics*, vol. 1, no. 3, p. 204, 2018.

[30] K. B. Oldham, J. C. Myland, and A. M. Bond, *Electrochemical Science and Technology: Fundamentals and Applications*. 2011.

[31] J. B. Goodenough and K. S. Park, “The Li-ion rechargeable battery: A perspective,” *Journal of the American Chemical Society*, vol. 135, no. 4, pp. 1167–1176, 2013.

[32] M. Whittingham, S., “1 - Intercalation Chemistry: An Introduction,” pp. 1–18, Academic Press, 1982.

[33] J. B. Goodenough and Y. Kim, “Challenges for rechargeable Li batteries,” *Chemistry of Materials*, vol. 22, no. 3, pp. 587–603, 2010.

[34] C. Liu, Z. G. Neale, and G. Cao, "Understanding electrochemical potentials of cathode materials in rechargeable batteries," *Materials Today*, vol. 19, no. 2, pp. 109–123, 2016.

[35] J. Mosa and M. Aparicio, *Lithium intercalation materials for battery prepared by sol-gel method.* 2018.

[36] Q. Li, J. Chen, L. Fan, X. Kong, and Y. Lu, "Progress in electrolytes for rechargeable Li-based batteries and beyond," *Green Energy and Environment*, vol. 1, no. 1, pp. 18–42, 2016.

[37] S. J. An, J. Li, C. Daniel, D. Mohanty, S. Nagpure, and D. L. Wood, "The state of understanding of the lithium-ion-battery graphite solid electrolyte interphase (SEI) and its relationship to formation cycling," *Carbon*, vol. 105, pp. 52–76, 2016.

[38] Z. Xu, J. Yang, H. Li, Y. Nuli, and J. Wang, "Electrolytes for advanced lithium ion batteries using silicon-based anodes," *Journal of Materials Chemistry A*, vol. 7, no. 16, pp. 9432–9446, 2019.

[39] M. O. Skare, "A Method for Controlled Oxide and Carbon Coating of Silicon Nanoparticles as Anode in Lithium-Ion Batteries," 2017.

[40] N. T. T. K., "Lithium Ion Rechargeable Battery," *Prog. Batteries Solar Cells*, no. 9, pp. 209–219, 1990.

[41] N. Nitta, F. Wu, J. T. Lee, and G. Yushin, "Li-ion battery materials: Present and future," *Materials Today*, vol. 18, no. 5, pp. 252–264, 2015.

[42] J. Lu, Z. Chen, F. Pan, Y. Cui, and K. Amine, "High-Performance Anode Materials for Rechargeable Lithium-Ion Batteries," *Electrochemical Energy Reviews*, vol. 1, no. 1, pp. 35–53, 2018.

[43] S. Goriparti, E. Miele, F. De Angelis, E. Di Fabrizio, R. Proietti Zaccaria, and C. Capiglia, "Review on recent progress of nanostructured anode materials for Li-ion batteries," *Journal of Power Sources*, vol. 257, pp. 421–443, 2014.

[44] W. Xu, J. Wang, F. Ding, X. Chen, E. Nasybulin, Y. Zhang, and J. G. Zhang, "Lithium metal anodes for rechargeable batteries," 1 2014.

[45] H. Tian, F. Xin, X. Wang, W. He, and W. Han, "High capacity group-IV elements (Si, Ge, Sn) based anodes for lithium-ion batteries," *Journal of Materiomics*, vol. 1, no. 3, pp. 153–169, 2015.

[46] N. Liu, W. Li, M. Pasta, and Y. Cui, “Nanomaterials for electrochemical energy storage,” *Frontiers of Physics*, vol. 9, no. 3, pp. 323–350, 2014.

[47] M. Ashuri, Q. He, and L. L. Shaw, “Silicon as a potential anode material for Li-ion batteries: Where size, geometry and structure matter,” *Nanoscale*, vol. 8, no. 1, pp. 74–103, 2016.

[48] J. W. Choi and D. Aurbach, “Promise and reality of post-lithium-ion batteries with high energy densities,” 3 2016.

[49] M. T. McDowell, S. W. Lee, J. T. Harris, B. A. Korgel, C. Wang, W. D. Nix, and Y. Cui, “In situ TEM of two-phase lithiation of amorphous silicon nanospheres,” *Nano Letters*, vol. 13, no. 2, pp. 758–764, 2013.

[50] K. Ogata, E. Salager, C. J. Kerr, A. E. Fraser, C. Ducati, A. J. Morris, S. Hofmann, and C. P. Grey, “Revealing lithium-silicide phase transformations in nano-structured silicon-based lithium ion batteries via in situ NMR spectroscopy,” *Nature Communications*, vol. 5, 2014.

[51] J. Li and J. R. Dahn, “An In Situ X-Ray Diffraction Study of the Reaction of Li with Crystalline Si,” *Journal of The Electrochemical Society*, vol. 154, no. 3, p. A156, 2007.

[52] P. Limthongkul, Y. I. Jang, N. J. Dudney, and Y. M. Chiang, “Electrochemically-driven solid-state amorphization in lithium-silicon alloys and implications for lithium storage,” *Acta Materialia*, vol. 51, no. 4, pp. 1103–1113, 2003.

[53] M. J. Chon, V. A. Sethuraman, A. McCormick, V. Srinivasan, and P. R. Guduru, “Real-time measurement of stress and damage evolution during initial lithiation of crystalline silicon,” *Physical Review Letters*, vol. 107, no. 4, pp. 1–4, 2011.

[54] S. D. Beattie, D. Larcher, M. Morcrette, B. Simon, and J.-M. Tarascon, “Si Electrodes for Li-Ion Batteries—A New Way to Look at an Old Problem,” *Journal of The Electrochemical Society*, vol. 155, no. 2, p. A158, 2008.

[55] M. T. McDowell, I. Ryu, S. W. Lee, C. Wang, W. D. Nix, and Y. Cui, “Studying the kinetics of crystalline silicon nanoparticle lithiation with in situ transmission electron microscopy,” *Advanced Materials*, vol. 24, no. 45, pp. 6034–6041, 2012.

[56] K. Rhodes, N. Dudney, E. Lara-Curzio, and C. Daniel, “Understanding the Degradation of Silicon Electrodes for Lithium-Ion Batteries Using Acoustic

Emission," *Journal of The Electrochemical Society*, vol. 157, no. 12, p. A1354, 2010.

[57] G. G. Eshetu and E. Figgemeier, "Confronting the Challenges of Next-Generation Silicon Anode-Based Lithium-Ion Batteries: Role of Designer Electrolyte Additives and Polymeric Binders," *ChemSusChem*, vol. 12, no. 12, pp. 2515–2539, 2019.

[58] S. M. Boroujeni and K. P. Birke, "Study of a Li-ion cell kinetics in five regions to predict Li plating using a pseudo two-dimensional model," *Sustainability (Switzerland)*, vol. 11, no. 22, 2019.

[59] K. Peng, J. Jie, W. Zhang, and S. T. Lee, "Silicon nanowires for rechargeable lithium-ion battery anodes," *Applied Physics Letters*, vol. 93, no. 3, pp. 1–4, 2008.

[60] M. S. Park, G. X. Wang, H. K. Liu, and S. X. Dou, "Electrochemical properties of Si thin film prepared by pulsed laser deposition for lithium ion micro-batteries," *Electrochimica Acta*, vol. 51, no. 25, pp. 5246–5249, 2006.

[61] L. Lin, Y. Ma, Q. Xie, L. Wang, Q. Zhang, and D. L. Peng, "Copper-Nanoparticle-Induced Porous Si/Cu Composite Films as an Anode for Lithium Ion Batteries," *ACS Nano*, vol. 11, no. 7, pp. 6893–6903, 2017.

[62] D. Mazouzi, B. Lestriez, L. Roué, and D. Guyomard, "Silicon composite electrode with high capacity and long cycle life," *Electrochemical and Solid-State Letters*, vol. 12, no. 11, 2009.

[63] D. Mazouzi, Z. Karkar, C. R. Hernandez, P. J. Manero, D. Guyomard, L. Roué, and B. Lestriez, "Critical roles of binders and formulation at multiscales of silicon-based composite electrodes," *Journal of Power Sources*, vol. 280, pp. 533–549, 2015.

[64] J. S. Bridel, T. Azaïs, M. Morcrette, J. M. Tarascon, and D. Larcher, "Key parameters governing the reversibility of Si/carbon/CMC electrodes for Li-ion batteries," *Chemistry of Materials*, vol. 22, no. 3, pp. 1229–1241, 2010.

[65] C. E. L. Foss, S. Müssig, A. M. Svensson, P. J. Vie, A. Ulvestad, J. P. Mæhlen, and A. Y. Koposov, "Anodes for Li-ion batteries prepared from microcrystalline silicon and enabled by binder's chemistry and pseudo-self-healing," *Scientific Reports*, vol. 10, no. 1, pp. 1–8, 2020.

[66] P. Parikh, M. Sina, A. Banerjee, X. Wang, M. S. D'Souza, J. M. Doux, E. A. Wu, O. Y. Trieu, Y. Gong, Q. Zhou, K. Snyder, and Y. S. Meng, "Role of

Polyacrylic Acid (PAA) Binder on the Solid Electrolyte Interphase in Silicon Anodes," *Chemistry of Materials*, vol. 31, no. 7, pp. 2535–2544, 2019.

[67] D. Mazouzi, Z. Karkar, C. R. Hernandez, P. J. Manero, D. Guyomard, L. Roué, and B. Lestriez, "Critical roles of binders and formulation at multiscales of silicon-based composite electrodes," *Journal of Power Sources*, vol. 280, pp. 533–549, 2015.

[68] T. Jaumann, J. Balach, U. Langklotz, V. Sauchuk, M. Fritsch, A. Michaelis, V. Teltevskij, D. Mikhailova, S. Oswald, M. Klose, G. Stephani, R. Hauser, J. Eckert, and L. Giebeler, "Lifetime vs. rate capability: Understanding the role of FEC and VC in high-energy Li-ion batteries with nano-silicon anodes," *Energy Storage Materials*, vol. 6, no. August 2016, pp. 26–35, 2017.

[69] R. Jung, M. Metzger, D. Haering, S. Solchenbach, C. Marino, N. Tsiouvaras, C. Stinner, and H. A. Gasteiger, "Consumption of Fluoroethylene Carbonate (FEC) on Si-C Composite Electrodes for Li-Ion Batteries," *Journal of The Electrochemical Society*, vol. 163, no. 8, pp. A1705–A1716, 2016.

[70] V. Etacheri, O. Haik, Y. Goffer, G. A. Roberts, I. C. Stefan, R. Fasching, and D. Aurbach, "Effect of fluoroethylene carbonate (FEC) on the performance and surface chemistry of Si-nanowire li-ion battery anodes," *Langmuir*, vol. 28, no. 1, pp. 965–976, 2012.

[71] T. Jaumann, J. Balach, M. Klose, S. Oswald, U. Langklotz, A. Michaelis, J. Eckert, and L. Giebeler, "SEI-component formation on sub 5 nm sized silicon nanoparticles in Li-ion batteries: The role of electrode preparation, FEC addition and binders," *Physical Chemistry Chemical Physics*, vol. 17, no. 38, pp. 24956–24967, 2015.

[72] M. L. Terranova, S. Orlanducci, E. Tamburri, V. Guglielmotti, and M. Rossi, "Si/C hybrid nanostructures for Li-ion anodes: An overview," *Journal of Power Sources*, vol. 246, pp. 167–177, 2014.

[73] X. Shen, Z. Tian, R. Fan, L. Shao, D. Zhang, G. Cao, L. Kou, and Y. Bai, "Research progress on silicon/carbon composite anode materials for lithium-ion battery," *Journal of Energy Chemistry*, vol. 27, no. 4, pp. 1067–1090, 2018.

[74] G. Nava, J. Schwan, M. G. Boebinger, M. T. McDowell, and L. Mangolini, "Silicon-Core-Carbon-Shell Nanoparticles for Lithium-Ion Batteries: Rational Comparison between Amorphous and Graphitic Carbon Coatings," *Nano Letters*, vol. 19, no. 10, pp. 7236–7245, 2019.

[75] S. H. Ng, J. Wang, D. Wexler, K. Konstantinov, Z. P. Guo, and H. K. Liu, “Highly reversible lithium storage in spheroidal carbon-coated silicon nanocomposites as anodes for lithium-ion batteries,” *Angewandte Chemie - International Edition*, vol. 45, pp. 6896–6899, 10 2006.

[76] Y. S. Hu, R. Demir-Cakan, M. M. Titirici, J. O. Müller, R. Schlögl, M. Antonietti, and J. Maier, “Superior storage performance of a Si@SiOx/C nanocomposite as anode material for lithium-ion batteries,” *Angewandte Chemie - International Edition*, vol. 47, no. 9, pp. 1645–1649, 2008.

[77] P. Gao, J. Fu, J. Yang, R. Lv, J. Wang, Y. Nuli, and X. Tang, “Microporous carbon coated silicon core/shell nanocomposite via in situ polymerization for advanced Li-ion battery anode material,” *Physical Chemistry Chemical Physics*, vol. 11, no. 47, pp. 11101–11105, 2009.

[78] Y. Xu, G. Yin, Y. Ma, P. Zuo, and X. Cheng, “Nanosized core/shell silicon@carbon anode material for lithium ion batteries with polyvinylidene fluoride as carbon source,” *Journal of Materials Chemistry*, vol. 20, no. 16, pp. 3216–3220, 2010.

[79] H. Tao, L. Z. Fan, W. L. Song, M. Wu, X. He, and X. Qu, “Hollow core-shell structured Si/C nanocomposites as high-performance anode materials for lithium-ion batteries,” *Nanoscale*, vol. 6, no. 6, pp. 3138–3142, 2014.

[80] L. Zhang, R. Rajagopalan, H. Guo, X. Hu, S. Dou, and H. Liu, “A Green and Facile Way to Prepare Granadilla-Like Silicon-Based Anode Materials for Li-Ion Batteries,” *Advanced Functional Materials*, vol. 26, no. 3, pp. 440–446, 2016.

[81] L. Pan, H. Wang, D. Gao, S. Chen, L. Tan, and L. Li, “Facile synthesis of yolk–shell structured Si–C nanocomposites as anodes for lithium-ion batteries,” *Chemical Communications*, vol. 50, no. 44, pp. 5878–5880, 2014.

[82] Z. Lu, B. Li, D. Yang, H. Lv, M. Xue, and C. Zhang, “A self-assembled silicon/phenolic resin-based carbon core-shell nanocomposite as an anode material for lithium-ion batteries,” *RSC Advances*, vol. 8, no. 7, pp. 3477–3482, 2018.

[83] Y. Tzeng, W. C. Huang, C. Y. Jhan, and Y. H. Wu, “Effects of in situ graphitic nanocarbon coatings on cycling performance of silicon-flake-based anode of lithium ion battery,” *Coatings*, vol. 11, no. 2, pp. 1–19, 2021.

[84] R. W. Pekala, “Organic aerogels from the polycondensation of resorcinol with formaldehyde,” *Journal of Materials Science*, vol. 24, no. 9, pp. 3221–3227, 1989.

[85] J. Liu, S. Z. Qiao, H. Liu, J. Chen, A. Orpe, D. Zhao, and G. Q. Lu, “Extension of the stöber method to the preparation of monodisperse resorcinol-formaldehyde resin polymer and carbon spheres,” *Angewandte Chemie - International Edition*, vol. 50, no. 26, pp. 5947–5951, 2011.

[86] T. Li, M. Cao, J. Liang, X. Xie, and G. Du, “Mechanism of base-catalyzed resorcinol-formaldehyde and phenol-resorcinol-formaldehyde condensation reactions: A theoretical study,” *Polymers*, vol. 9, no. 9, 2017.

[87] S. E. Blanco, M. C. Almandoz, and F. H. Ferretti, “Determination of the overlapping pKa values of resorcinol using UV-visible spectroscopy and DFT methods,” *Spectrochimica Acta - Part A: Molecular and Biomolecular Spectroscopy*, vol. 61, no. 1-2, pp. 93–102, 2005.

[88] N. Li, Q. Zhang, J. Liu, J. Joo, A. Lee, Y. Gan, and Y. Yin, “Sol-gel coating of inorganic nanostructures with resorcinol-formaldehyde resin,” *Chemical Communications*, vol. 49, no. 45, pp. 5135–5137, 2013.

[89] X. Fang, S. Liu, J. Zang, C. Xu, M. S. Zheng, Q. F. Dong, D. Sun, and N. Zheng, “Precisely controlled resorcinol–formaldehyde resin coating for fabricating core–shell, hollow, and yolk–shell carbon nanostructures,” *Nanoscale*, vol. 5, no. 15, pp. 6908–6916, 2013.

[90] M. Kosmulski, “Chemical properties of material surfaces,” 2001.

[91] E. Y. Bryleva, N. A. Vodolazkaya, N. O. Mchedlov-Petrossyan, L. V. Samokhina, N. A. Matveevskaya, and A. V. Tolmachev, “Interfacial properties of cetyltrimethylammonium-coated SiO2 nanoparticles in aqueous media as studied by using different indicator dyes,” *Journal of Colloid and Interface Science*, vol. 316, no. 2, pp. 712–722, 2007.

[92] G. Zhu, Y. Wang, S. Yang, Q. Qu, and H. Zheng, “Correlation between the physical parameters and the electrochemical performance of a silicon anode in lithium-ion batteries,” *Journal of Materiomics*, vol. 5, no. 2, pp. 164–175, 2019.

[93] Y. S. Hu, R. Demir-Cakan, M. M. Titirici, J. O. Müller, R. Schlögl, M. Antonietti, and J. Maier, “Superior storage performance of a Si@SiOx/C nanocomposite as anode material for lithium-ion batteries,” *Angewandte Chemie - International Edition*, vol. 47, no. 9, pp. 1645–1649, 2008.

[94] D. Shao, D. Tang, Y. Mai, and L. Zhang, “Nanostructured silicon/porous carbon spherical composite as a high capacity anode for Li-ion batteries,” *Journal of Materials Chemistry A*, vol. 1, no. 47, pp. 15068–15075, 2013.

[95] M. V. Blanco, V. Renman, F. Vullum-Bruer, and A. M. Svensson, “Nanostructured diatom earth SiO2negative electrodes with superior electrochemical performance for lithium ion batteries,” *RSC Advances*, vol. 10, no. 55, pp. 33490–33498, 2020.

[96] M. V. Blanco, V. Renman, J. Zhu, F. Vullum-Bruer, and A. M. Svensson, “Optimizing carbon coating parameters for obtaining SiO2/C anodes with improved electrochemical performance,” *Journal of Solid State Electrochemistry*, vol. 25, no. 4, pp. 1339–1351, 2021.

[97] J.R. Dahn, Tao Zheng, Yinghu Liu, and J.S. Xue, “Mechanisms for Lithium Insertion in Carbonaceous Materials,” *Science*, vol. 270, p. 590, 1995.

[98] “Front Matter,” in *Developments in Surface Contamination and Cleaning, Volume 12* (R. Kohli and K. L. Mittal, eds.), pp. i–iii, Elsevier, 2019.

[99] K. Barmak, K. R. Coffey, B. Ingham, M. F. Toney, K. Barmak, P. B. Barna, G. Radnóczi, T. P. Weihs, S.-L. Zhang, Z. Zhang, W. D. Nix, K. R. Coffey, T. Thomson, D. Shelton, and P. Schelling, “Metallic Films for Electronic, Optical and Magnetic Applications,” in *Metallic Films for Electronic, Optical and Magnetic Applications* (K. Barmak and K. Coffey, eds.), pp. xi–xiii, Woodhead Publishing, 2014.

[100] S. Bandyopadhyay, *Fabrication and Application of Nanomaterials*. New York: McGraw-Hill Education, 1st edition. ed., 2019.

[101] M. Thommes, K. Kaneko, A. V. Neimark, J. P. Olivier, F. Rodriguez-Reinoso, J. Rouquerol, and K. S. Sing, “Physisorption of gases, with special reference to the evaluation of surface area and pore size distribution (IUPAC Technical Report),” *Pure and Applied Chemistry*, vol. 87, pp. 1051–1069, 10 2015.

[102] J. J. Friel and C. E. Lyman, “Tutorial review: X-ray mapping in electron-beam instruments,” 2 2006.

[103] D. R. Vij Editor, “Handbook of Applied Solid State Spectroscopy,” tech. rep.

[104] N. P. Wagner, A. Tron, J. R. Tolchard, G. Noia, and M. P. Bellmann, “Silicon anodes for lithium-ion batteries produced from recovered kerf powders,” tech. rep.

[105] H. G. Schweiger, O. Obeidi, O. Komesker, A. Raschke, M. Schiemann, C. Zehner, M. Gehnen, M. Keller, and P. Birke, “Comparison of several methods for determining the internal resistance of lithium ion cells,” *Sensors*, vol. 10, no. 6, pp. 5604–5625, 2010.

[106] J. M. Westra, V. Vavrunková, P. Ŝutta, R. A. Van Swaaij, and M. Zeman, “Formation of thin-film crystalline silicon on glass observed by in-situ XRD,” in *Energy Procedia*, vol. 2, pp. 235–241, 8 2010.

[107] L. J. Krause, T. Brandt, V. L. Chevrier, and L. D. Jensen, “Surface Area Increase of Silicon Alloys in Li-Ion Full Cells Measured by Isothermal Heat Flow Calorimetry,” *Journal of The Electrochemical Society*, vol. 164, no. 9, pp. A2277–A2282, 2017.

[108] C. F. Holder and R. E. Schaak, “Tutorial on Powder X-ray Diffraction for Characterizing Nanoscale Materials,” 7 2019.

[109] T. D. Shen, C. C. Koch, T. L. McCormick, R. J. Nemanich, J. Y. Huang, and J. G. Huang, “The structure and property characteristics of amorphous/nanocrystalline silicon produced by ball milling,” *Journal of Materials Research*, vol. 10, no. 1, pp. 139–148, 1995.

[110] D. Wang, M. Gao, H. Pan, J. Wang, and Y. Liu, “High performance amorphous-Si@SiOx/C composite anode materials for Li-ion batteries derived from ball-milling and in situ carbonization,” *Journal of Power Sources*, vol. 256, pp. 190–199, 6 2014.

[111] S. Sim, P. Oh, S. Park, and J. Cho, “Critical thickness of SiO2 coating layer on core@Shell bulk@nanowire Si anode materials for Li-ion batteries,” *Advanced Materials*, vol. 25, pp. 4498–4503, 8 2013.

[112] S. Xun, X. Song, L. Wang, M. E. Grass, Z. Liu, V. S. Battaglia, and G. Liu, “The Effects of Native Oxide Surface Layer on the Electrochemical Performance of Si Nanoparticle-Based Electrodes,” *Journal of The Electrochemical Society*, vol. 158, no. 12, p. A1260, 2011.

[113] V. J. Ovejas and A. Cuadras, “State of charge dependency of the overvoltage generated in commercial Li-ion cells,” *Journal of Power Sources*, vol. 418, pp. 176–185, 4 2019.

[114] B. Philippe, R. Dedryvère, J. Allouche, F. Lindgren, M. Gorgoi, H. Rensmo, D. Gonbeau, and K. Edström, “Nanosilicon electrodes for lithium-ion batteries:

Interfacial mechanisms studied by hard and soft X-ray photoelectron spectroscopy," *Chemistry of Materials*, vol. 24, pp. 1107–1115, 3 2012.

[115] S. Vepřek, F.-A. Sarott, and M. Rückschloß, "Temperature dependence of the crystallite size and crystalline fraction of microcrystalline silicon deposited from silane by plasma CVD," *Journal of Non-Crystalline Solids*, vol. 137-138, pp. 733–736, 1991.

[116] J. Liu, S. Z. Qiao, H. Liu, J. Chen, A. Orpe, D. Zhao, and G. Q. M. Lu, "Extension of The Stöber Method to the Preparation of Monodisperse Resorcinol-Formaldehyde Resin Polymer and Carbon Spheres," *Angewandte Chemie*, vol. 123, no. 26, pp. 6069–6073, 2011.

[117] K. A. See, M. A. Lumley, G. D. Stucky, C. P. Grey, and R. Seshadri, "Reversible Capacity of Conductive Carbon Additives at Low Potentials: Caveats for Testing Alternative Anode Materials for Li-Ion Batteries," *Journal of The Electrochemical Society*, vol. 164, no. 2, pp. A327–A333, 2017.

[118] W. Luo, Y. Wang, S. Chou, Y. Xu, W. Li, B. Kong, S. X. Dou, H. K. Liu, and J. Yang, "Critical thickness of phenolic resin-based carbon interfacial layer for improving long cycling stability of silicon nanoparticle anodes," *Nano Energy*, vol. 27, pp. 255–264, 2016.

[119] C. Matei Ghimbeu, J. Górka, V. Simone, L. Simonin, S. Martinet, and C. Vix-Guterl, "Insights on the Na+ ion storage mechanism in hard carbon: Discrimination between the porosity, surface functional groups and defects," *Nano Energy*, vol. 44, pp. 327–335, 2 2018.

[120] M. S. Shafeeyan, W. M. A. W. Daud, A. Houshmand, and A. Shamiri, "A review on surface modification of activated carbon for carbon dioxide adsorption," 2010.

[121] S. J. Taylor, M. D. Haw, J. Sefcik, and A. J. Fletcher, "Gelation mechanism of resorcinol-formaldehyde gels investigated by dynamic light scattering," *Langmuir*, vol. 30, no. 34, pp. 10231–10240, 2014.

[122] B. E. Deal and A. S. Grove, "General relationship for the thermal oxidation of silicon," *Journal of Applied Physics*, vol. 36, no. 12, pp. 3770–3778, 1965.

[123] R. G. Stephen and F. L. Riley, "Oxidation of Silicon by Water," tech. rep., 1989.

[124] W. Li, K. Cao, H. Wang, J. Liu, L. Zhou, and H. Yao, “Carbon coating may expedite the fracture of carbon-coated silicon core-shell nanoparticles during lithiation,” *Nanoscale*, vol. 8, no. 9, pp. 5254–5259, 2016.

[125] Z. L. Xu, K. Cao, S. Abouali, M. Akbari Garakani, J. Huang, J. Q. Huang, E. Kamali Heidari, H. Wang, and J. K. Kim, “Study of lithiation mechanisms of high performance carbon-coated Si anodes by in-situ microscopy,” *Energy Storage Materials*, vol. 3, pp. 45–54, 4 2016.

[126] S. D. Beattie, M. J. Loveridge, M. J. Lain, S. Ferrari, B. J. Polzin, R. Bhagat, and R. Dashwood, “Understanding capacity fade in silicon based electrodes for lithium-ion batteries using three electrode cells and upper cut-off voltage studies,” *Journal of Power Sources*, vol. 302, pp. 426–430, 2016.

[127] H. F. Andersen, C. E. L. Foss, J. Voje, R. Tronstad, T. Mokkelbost, P. E. Vullum, A. Ulvestad, M. Kirkengen, and J. P. Mæhlen, “Silicon-Carbon composite anodes from industrial battery grade silicon,” *Scientific Reports*, vol. 9, no. 1, pp. 1–9, 2019.

[128] S. Y. Lai, K. D. Knudsen, B. T. Sejersted, A. Ulvestad, J. P. Mæhlen, and A. Y. Koposov, “Silicon Nanoparticle Ensembles for Lithium-Ion Batteries Elucidated by Small-Angle Neutron Scattering,” *ACS Applied Energy Materials*, vol. 2, no. 5, pp. 3220–3227, 2019.

Appendix

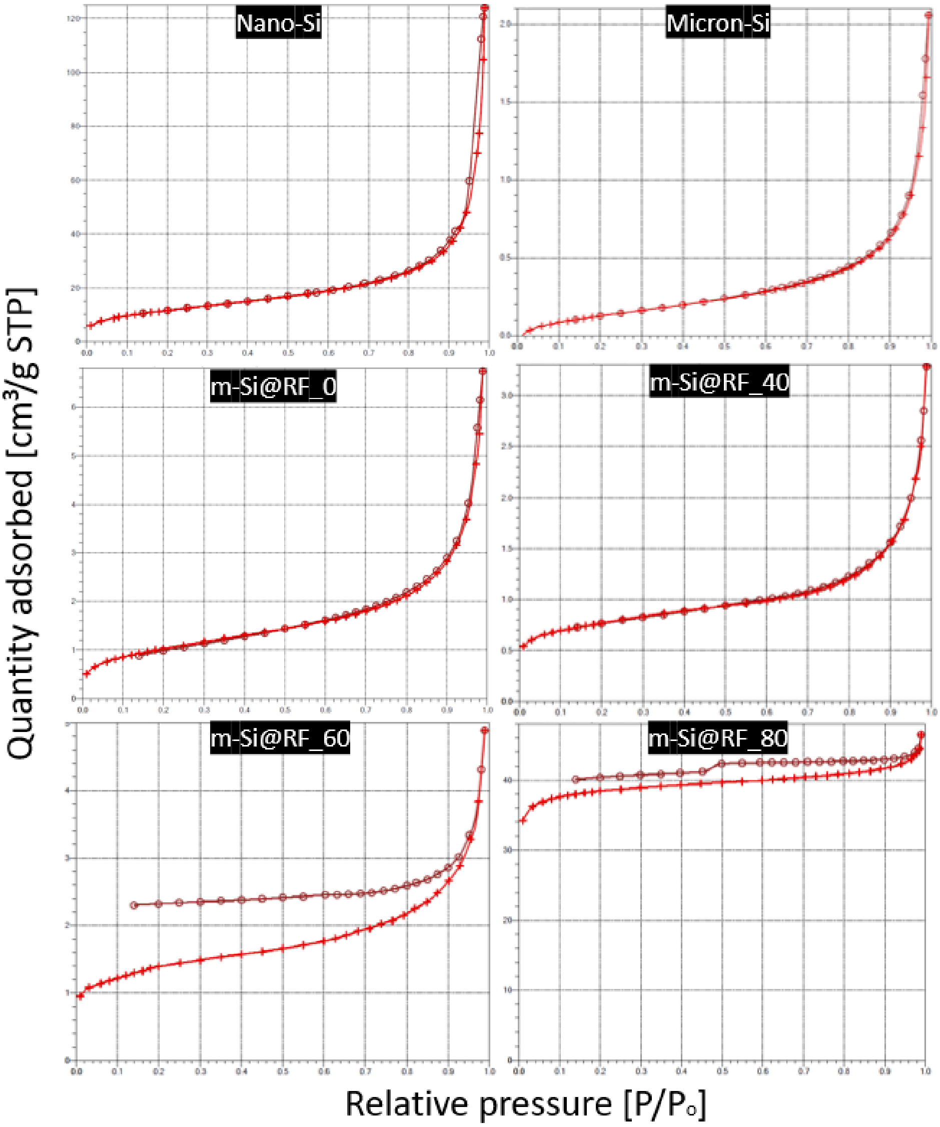

Figure A.1: Nitrogen adsorption and desorption isotherms of Nano-Si, Micron-Si, m-Si@RF_0, m-Si@RF_40, m-Si@RF_60, and m-Si@RF_80.

NTNU

Norwegian University of
Science and Technology